UNIVERSITY OF OKLAHOMA

GRADUATE COLLEGE

QUASI-ISOTROPIC LOW SIZE, WEIGHT, AND POWER TAG FOR REMOTELY TRACKING BIRDS USING WEATHER RADAR

A THESIS

SUBMITTED TO THE GRADUATE FACULTY

in partial fulfillment of the requirements for the

Degree of

MASTER OF SCIENCE

By

BRYAN SANDOVAL

Norman, Oklahoma

2021

Downloaded from SHAREOK. Persistent Handle URL: https://hdl.handle.net/11244/329027

QUASI-ISOTROPIC LOW SIZE, WEIGHT, AND POWER TAG FOR REMOTELY TRACKING BIRDS USING WEATHER RADAR

A THESIS APPROVED FOR THE
SCHOOL OF ELECTRICAL AND COMPUTER ENGINEERING

BY THE COMMITTEE CONSISTING OF

Dr. Jessica Ruyle, Chair

Dr. Caleb Fulton

Dr. Eli Bridge

© Copyright by BRYAN SANDOVAL 2021
All Rights Reserved.

Acknowledgments

I would like to acknowledge and give a big thanks to Clayton Blosser, who helped me by fabricating and testing the Bazooka Balun. I would also like to thank Adrian Bauer for teaching and helping me through out the fabrication and testing process. This was a huge help and I am grateful for that. I would also like to thank my committee for the guidance and mentor-ship they have provided me throughout my masters program. I would like to give a special thanks to Dr. Jessica Ruyle. She gave me an opportunity to do undergraduate research several years ago and it has forever changed my life. Throughout my time doing research, I struggled to learn concepts and often spent long days and nights studying. Dr. Ruyle was always there to answer any questions and guide me throughout tough times. Similarly, I would also like to acknowledge my good friend, Alex Moreno. Alex has been a crucial friend and mentor that has helped develop the confidence that I have today. I wouldn't have preserved through my undergraduate and graduate degree as well as I did without you. Thank you.

This acknowledgment would not be complete without giving thanks to my beautiful family. To my parents, who have always instilled hard work and love to break generational barriers. To my siblings, for giving me a reason to keep doing the best I can. To my two dogs, Bubba Joe and Ace, for giving me a reason to take well needed breaks and to remember to have fun. Lastly, to my beautiful wife, Samanta Sandoval. You are my best friend and my life partner. You have always supported me and always managed to make me laugh when I needed it the most. I love you.

Table of Contents

Acknowledgments **iv**

List of Tables **viii**

List of Figures **ix**

Abstract **xvii**

1 Introduction **1**

2 Formulating Design Requirements **9**

2.1 Introduction 9

2.2 Formulating Design Requirements 9

2.3 Previous RFID Antennas 11

2.4 Typical Omnidirectional Antennas 17

2.5 Conclusion 20

3 Antenna Parameters and Limitations **22**

3.1 Introduction 22

3.2 Antenna Size Limitation 22

3.2.1 Minimum Antenna Quality Factor 22

3.2.2 Maximum Theoretical Gain per Kilometers 25

3.3 Achievable Bird size tagging 32
3.4 Conclusion 38

4 Antenna Simulation Analysis **40**
4.1 Introduction 40
4.2 Curved Folded Dipole Antenna 41
4.3 Bandwidth Analysis 45
4.4 Conclusion 56

5 Designing and Verifying Bird Model **58**
5.1 Introduction 58
5.2 Designing Bird Model 58
5.3 Verifying Bird Model 64
5.4 Conclusion 94

6 CFDA Measurements **95**
6.1 Introduction 95
6.2 CFDA Measurements 95
6.3 Conclusion 117

7 Hybrid RFID Circuit Layout **119**
7.1 Introduction 119
7.2 Hybrid RFID Circuit Layout 119
7.3 Conclusion 125

8 Conclusions and Future Work **126**
8.1 Conclusions 126
8.2 Scientific Impact 127

8.3 Future Work 127

References **129**

List of Tables

3.1 Radar Range Equation Input Parameters 29

3.2 List of Components and their corresponding weight for the Hybrid RFID Tag from [8] 33

3.3 Weight Comparison between Copper and stainless steel memory wire . 34

3.4 List of newly proposed Components and their corresponding weight for the Hybrid RFID Tag 38

7.1 List of Components and their corresponding weight for the Hybrid RFID Tag from [8] 120

7.2 Updated List of Key Components and their corresponding weight for the Hybrid RFID Tag for circuit layout prototype 120

List of Figures

1.1 Examples of Commercially available RFID PIT Tags that are relatively small [5]. 2

1.2 Electronic Transponder Analysis Gateway (ETAG) RFID Reader circuit with key components labeled [7]. 3

1.3 (a) RFID-eqipped Wood Duck nest box (b) RFID reader equipped in the attic of the Bluebird next box nest box [7]. 4

1.4 (a) WSR-88d Weather Radar that is part of the Next-Generation Radar (NEXRAD) network [9]. (b) Original Hybrid Active-Passive RFID circuit prototype under test from [8]. 6

2.1 Illustrative comparison of an omnidirectional (desired) and a non-omnidirectional (undesired) radiation pattern with respect to the radar 11

2.2 (a) Photo of the Low Profile Antenna prototype; (b) Normalized measured azimuthal radiation pattern of the Low Profile antenna from [10] . 12

2.3 (a) Photo of the compact Dipolar Patch Antenna prototype; (b) Normalized Realized Gain of the Dipolar Patch antenna from [12] 14

2.4 (a) Geometric Shape and dimensions of the coplanar waveguide-fed patch antenna; (b) Azimuth Gain radiation pattern of the coplanar waveguide fed patch antenna from [11] 15

2.5 (a) Geometry of the 3D antenna; (b) prototype of the 3D antenna placed on a box from [15] 16
2.6 Radiation Patterns of the 3D antenna (solid lines) compared to a simple planar dipole (dashed lines) in E-Plane and H-plane, respectfully from [15] 17
2.7 A 3D Radiation Pattern of the Halfwave Dipole antenna from [16] . . . 18
2.8 (a) Geometry of the wire S-Shaped Dipole antenna; (b) Radiation pattern on the x-y plane for the S-Shaped Dipole from [17] 19
2.9 Radiation Pattern of the loop antenna from [18] 20

3.1 Capacitor-plate dipole antenna enclosed within a radian-sphere from [20] 23
3.2 Antenna Size per Fractional Bandwidth 25
3.3 (a) Antenna Size per Realized Gain; (b) Antenna Size and Realized Gain per Fractional Bandwidth 27
3.4 Max Range per Realized Gain 30
3.5 Max Range per Realized Gain Across Modulation Factors 31
3.6 In Black: Range at 144 Kilometers; In Red: Range at 97 Kilometers . . 32
3.7 Weight Classes of Birds with current tracking technology 34
3.8 Single Layer of Flex Board Material from [24] 35
3.9 LifeTag from Cellular Tracking technologies from [25] 37

4.1 Curved Folded Dipole Antenna from [26] 41
4.2 Curvature Analysis on Impedance and Radiation efficiency from [26] . 42
4.3 Return Loss (S11) at selected curvature angles from [26] 42
4.4 Far field radiation pattern E and H plane reference from [26] 43
4.5 Far Field radiation pattern trends across Curvature angle from [26] . . . 43

4.6 Size difference in (a) $\theta = 0$ and (b) $\theta = 180$ 45
4.7 Same Footprint shown for CFDA with (a) $w2$=1 mm and (b) $w2$=7 mm 47
4.8 Fractional Bandwidth swept across Various outer ribbon widths for 21 mm footprint antenna 49
4.9 Fractional Bandwidth swept across Various outer ribbon widths for 13.5 mm footprint antenna 50
4.10 Quality Factor for 21 mm footprint antenna with $w1$ = 1 mm 51
4.11 Quality Factor for 21 mm footprint antenna with $w1$ = 0.5 mm 52
4.12 Quality Factor for 13.5 mm footprint antenna with $w1$ = 1 mm 53
4.13 Quality Factor for 13.5 mm footprint antenna with $w1$ = 0.5 mm 53
4.14 Realized Gain across frequency for 21 mm footprint CFDA with various $w2$ widths 55
4.15 Realized Gain across frequency for 21 mm footprint CFDA with $w2$= 4mm and $w1$ = 0.5 mm 56

5.1 Simple Bird Model from [29] 60
5.2 Diagram of Pigeon's Air-sacs from [30] 61
5.3 Dark-Eyed Junco from [31] 62
5.4 Bird Model with Inflated Air-sacs 63
5.5 Bird Model with Deflated Air-sacs 63
5.6 Dimetric View of the Simulated Ribbon Monopole with an operating frequency of 2.85 GHz 65
5.7 Before and After image of the Rogers 5880 substrate with inverted Mask fabricated via Photo-lithography process 66

5.8 Fabricated Ribbon Monopole with an operating frequency of 2.85 GHz (a) Top view of Ribbon monopole (b) Bottom view of ground plane with soldered coax connector 66
5.9 Magnitude of Insertion Loss ($|S_{11}|$) in dB plotted across frequency . . . 68
5.10 Input impedance (Z_{11}) plotted across frequency 68
5.11 Azimuth far-field radiation measurement set-up in anechoic chamber . . 70
5.12 Co-polarized Azimuth far-field radiation pattern measurement compared to simulated radiation pattern 70
5.13 Elevation far-field radiation pattern set-up in anechoic chamber (a) Elevation set-up with 3D mount (b) Side-view of Monopole orientated for $\Phi = 0$ (c) Side-view of Monopole orientated for $\Phi = 90$ 72
5.14 Co-polarized Elevation far-field radiation pattern measurement compared to simulated radiation pattern at $\Phi = 0$ 73
5.15 Co-polarized Elevation far-field radiation pattern measurement compared to simulated radiation pattern at $\Phi = 90$ 73
5.16 Illustration of a leg-loop harness for bird trackers from [32] 74
5.17 Simulated ribbon monopole with Bird Model GHz (a) Dimetric view of Bird model with monopole (b) Side view of Bird Model with monopole 75
5.18 Magnitude of Insertion Loss ($|S_{11}|$) in dB plotted across frequency for bird measurements compared to monopole 76
5.19 Input impedance (Z_{11}) plotted across frequency for bird measurements compared to monopole 77
5.20 Co-polarized Azimuth far-field radiation pattern with and without birds 78
5.21 Co-polarized Elevation far-field radiation pattern with and without birds at $\Phi = 0$ 79

5.22 Co-polarized Elevation far-field radiation pattern with and without birds at $\Phi = 90$ 79
5.23 Magnitude of Insertion Loss ($|S_{11}|$) in dB plotted across frequency for Inflated Bird Model vs Deflated Bird Model 81
5.24 Input impedance (Z_{11}) plotted across frequency for Inflated Bird Model vs Deflated Bird Model 81
5.25 Co-polarized Azimuth far-field radiation pattern for the Inflated Bird Model vs the Deflated Bird Model 82
5.26 Co-polarized Elevation far-field radiation pattern for the Inflated Bird Model vs the Deflated Bird Model at $\Phi = 0$ 83
5.27 Co-polarized Elevation far-field radiation pattern for the Inflated Bird Model vs the Deflated Bird Model at $\Phi = 90$ 83
5.28 Magnitude of Insertion Loss ($|S_{11}|$) in dB plotted across frequency for bird measurements compared to Bird Model 85
5.29 Input impedance (Z_{11}) plotted across frequency for bird measurements compared to Bird Model 85
5.30 Co-polarized Azimuth far-field radiation pattern for birds measurements compared to Bird Model 86
5.31 Co-polarized Elevation far-field radiation pattern for birds measurements compared to Bird Model at $\Phi = 0$ 87
5.32 Co-polarized Elevation far-field radiation pattern for birds measurements compared to Bird Model at $\Phi = 90$ 88
5.33 Final Bird Model with Inner and Outer Volume 89
5.34 Magnitude of Insertion Loss ($|S_{11}|$) in dB plotted across frequency for bird measurements compared to the Final Bird Model 90

5.35 Input impedance (Z_{11}) plotted across frequency for bird measurements compared to the Final Bird Model 91
5.36 Co-polarized Azimuth far-field radiation pattern for birds measurements compared to Final Bird Model 92
5.37 Co-polarized Elevation far-field radiation pattern for birds measurements compared to the Final Bird Model at $\Phi = 0$ 93
5.38 Co-polarized Elevation far-field radiation pattern for birds measurements compared to the Final Bird Model at $\Phi = 90$ 93

6.1 Curved Folded Dipole Antenna in HFSS with an inner ribbon width ($w1$) of 0.5 mm and an outer ribbon width ($w2$) of 4 mm 96
6.2 Fabricated Curved Folded Dipole Antenna next to a 1 cent coin (penny) for Size comparison 97
6.3 (a) Fabricated Bazooka Balun soldered to CFDA (b) Common Mode Rejection Ratio (CMRR) in dB plotted across frequency 98
6.4 Magnitude of Insertion Loss ($|S_{11}|$) in dB plotted across frequency for the Simulated vs Measured CFDA 100
6.5 Input impedance (Z_{11}) plotted across frequency for the Simulated vs Measured CFDA 100
6.6 Input impedance (Z_{11}) plotted across frequency for the Simulated vs Measured CFDA at various Dielectric constants 101
6.7 Azimuth radiation pattern Set-up for CFDA 102
6.8 Co-polarized Azimuth far-field radiation pattern for CFDA (Simulated vs Measured) 102
6.9 CFDA with Balun attached shown in HFSS with surface currents plotted on the Coax cable at 2.7 GHz, 2.85 GHz, and 2.95 GHz 104

6.10 Measured Azimuth Radiation Pattern (at 2.85 GHz and 2.7 GHz) overlaid on top of the CFDA with Balun in HFSS 105
6.11 Elevation radiation pattern Set-up for CFDA at (a) $\Phi = 0$ and (b) $\Phi = 90$ 106
6.12 The Simulated Co-polarized Elevation far-field radiation pattern for the CFDA (for 2.85 GHz) at $\Phi = 0$ 106
6.13 Co-polarized Elevation far-field radiation pattern for the CFDA (for 2.85 GHz) at $\Phi = 90$ 107
6.14 Co-polarized Elevation far-field radiation pattern for the CFDA (for 2.7 GHz) at $\Phi = 90$ 107
6.15 Representation of how salvaged bird carcasses were positioned for measurements 108
6.16 Co-polarized Azimuth far-field radiation pattern (at 2.85 GHz) for CFDA with salvaged bird carcasses 109
6.17 Co-polarized Azimuth far-field radiation pattern (at 2.7 GHz) for CFDA with salvaged bird carcasses 109
6.18 Co-polarized Elevation far-field radiation pattern for the CFDA (for 2.85 GHz) at $\Phi = 0$ with salvaged bird carcasses 111
6.19 Co-polarized Elevation far-field radiation pattern for the CFDA (for 2.7 GHz) at $\Phi = 0$ with salvaged bird carcasses 111
6.20 Co-polarized Elevation far-field radiation pattern for the CFDA (for 2.85 GHz) at $\Phi = 90$ with salvaged bird carcasses 112
6.21 Co-polarized Elevation far-field radiation pattern for the CFDA (for 2.7 GHz) at $\Phi = 90$ with salvaged bird carcasses 112
6.22 Representation of Bird Model was positioned for simulations 113

6.23 Magnitude of Insertion Loss ($|S_{11}|$) in dB plotted across frequency for the Simulated CFDA . . . 114
6.24 Input impedance (Z_{11}) plotted across frequency for the Simulated CFDA 114
6.25 Simulated Co-polarized Azimuth far-field radiation pattern (at 2.85 GHz) for CFDA with Bird Model . . . 115
6.26 Simulated co-polarized Elevation radiation pattern (at 2.85 GHz) for CFDA with Bird Model (a) at $\Phi = 0$ and (b) at $\Phi = 90$ . . . 116
6.27 Simulated Elevation radiation pattern (at 2.85 GHz) for CFDA at $\Phi = 90$ for Phi polarized, Theta polarized, and total Gain . . . 117

7.1 Hybrid RFID Circuit Schematic from [8] . . . 121
7.2 Custom made layout for the (a) RF Detector from (b) RF Switch (c) 4-Bit Counter . . . 122
7.3 Hybrid RFID Circuit Layout in AWR . . . 124
7.4 Hybrid RFID Circuit Layout Fabricated onto a 30 mil Rogers 4350 . . . 125

Abstract

Modern tracking technology has the potential to revolutionize the field of ornithology. However, some tracking technologies such as Radio Frequency Identification (RFID) are limited in read range while others such as GPS trackers can only track large birds due to tag weight. In this thesis, a quasi-isotropic low size, weight, and power active RFID tag is developed to track birds using the WSR-88D weather radar. For the radiator for the tag, a quasi-isotropic Curved Folded Dipole Antenna (CFDA) is designed to match the frequency and bandwidth of the WSR-88D radar. To ensure tag performance when attached to birds an electromagnetic phantom is developed to accurately represent a Dark-eyed Junco (*Junco Hyemalis*). This phantom is validated with bird measurements and can be used for future electromagnetic simulations involving birds. Lastly, a single layer board circuit layout is design for an RFID tag that will work with the WSR-88d radar and is fabricated to be used as the first prototype for this new tracking technology.

Chapter 1

Introduction

Antennas can be argued as the most critical component in a communication system because they are needed to transmit and receive signals. As technology advances, antennas need to become more adaptive and designed for specific applications. Wildlife tracking is one particular field where antennas have been designed for various tracking technology. For a couple of decades, Biologists have been integrating different tracking technology onto birds to monitor their migration routes and behavior. Radio Tracking, also known as Radio Telemetry, is one method that is used to pinpoint the location of a bird. Radio Tracking usually has a bird tagged with a pulsed transmitter while a Biologist utilizes a directional antenna, typically a Yagi-Uda antenna, to get a good localization of the transmitter [1]. Another method of tracking, called Geolocating with Loggers, uses small logging devices that store data such as the time of sunset and sunrise at pre-determined times [1]. Other tracking methods include Global Positioning System (GPS) and Global System for Mobile Communication (GSM), where the bird can be tagged with a GPS unit to get location coordinates directly or it can be linked with the mobile communication infrastructure to get the closet GPS coordinates through a mobile user nearby [1]. Each method of tracking has its specific applications and can have a limitation on what size bird to track. One method of wildlife tracking that can apply to smaller birds, that have gotten more attention in the recent decade, has

been Radio Frequency Identification (RFID).

RFID is a growing market that has been used in applications such as managing traffic, toll collection, gaining entrance to buildings and gated communities, tracking packages, and much more since the early 1990s [2]. More specifically in wildlife, RFID has been used to track birds and monitor their behavior through the use of Passive Integrated Transponders (PIT) tags in near-field applications. PIT tags are devices, typically a double-looped solenoid antenna with a chip, that transmit an identification number when scanned by a transmitter at Low Frequency (120 -150 KHz) and are relatively small in size (< 0.1g) [3], [4]. The sizes of several small RFID PIT tags that are commonly used to track animals are shown in Figure 1.1.

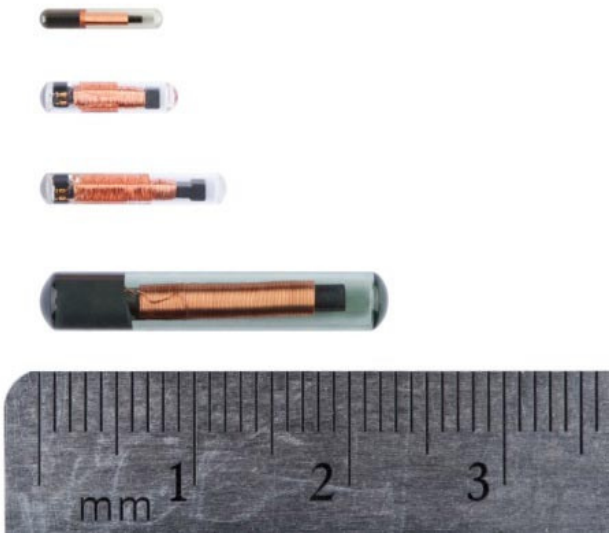

Figure 1.1: Examples of Commercially available RFID PIT Tags that are relatively small [5].

Since these are passive devices, they do not need their power supply, which limits the PIT tags to having to be in the read range of a transmitter. This read range is typically between 10-20 centimeters [6]. Because of this, RFID Reader systems, such as Electronic Transponder Analysis Gateway (ETAG) shown in Figure 1.2, are often

incorporated in nest boxes or bird feeders to allow the Ornithologists to collect data on the PIT tags that get logged onto the RFID system [3], which is accurately shown in Figure 1.3.

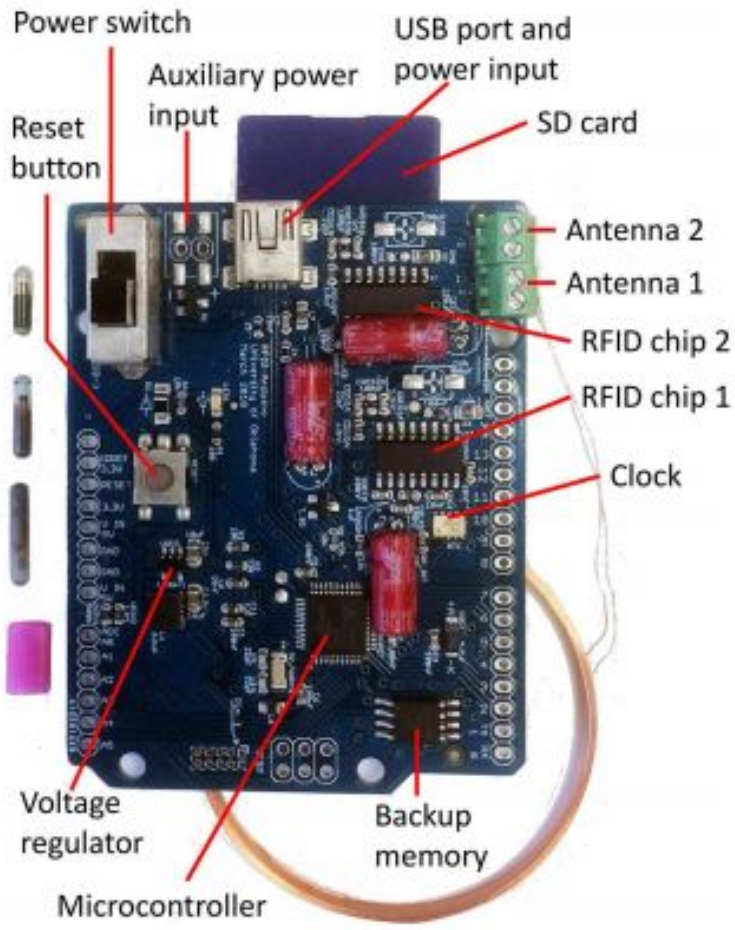

Figure 1.2: Electronic Transponder Analysis Gateway (ETAG) RFID Reader circuit with key components labeled [7].

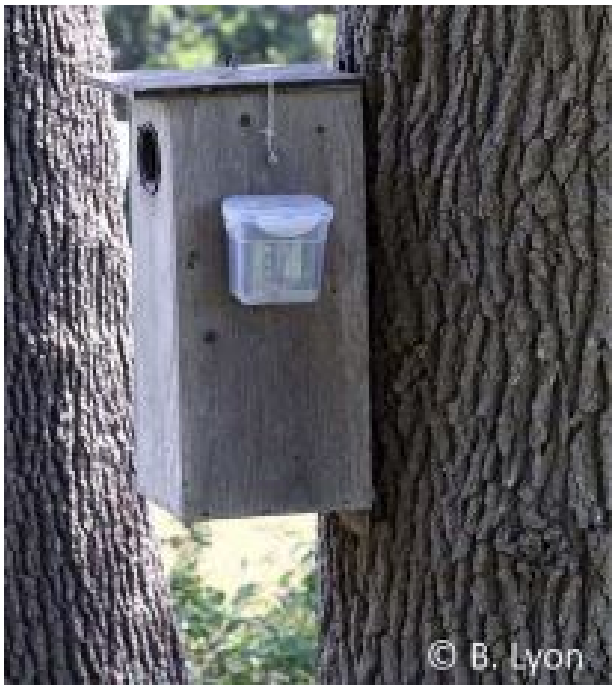

(a)



(b)

Figure 1.3: (a) RFID-eqipped Wood Duck nest box (b) RFID reader equipped in the attic of the Bluebird next box nest box [7].

However, since PIT tags have to be within proximity, this limits Ornithologists from only monitoring birds via the RFID systems in controlled environments. It would be beneficial for Ornithologists to be able to track and collect data on migration patterns using RFID tags. In fact, in recent literature, a Hybrid Active-Passive RFID tag was created to work with the WSR-88d weather radar, which is part of the Next-Generation Radar (NEXRAD) network [8]. This Hybrid Active-Passive RFID tag and WSR-88d weather radar are shown in Figure 1.4. This Hybrid RFID tag was designed to interface with the WSR-88d's through (ASK) back-scatter modulation at 2.85 GHz [8]. Due to the WSR-88d weather radar having a transmit power of 700 kilowatts, this will allow the previously mentioned Hybrid RFID tag to be tracked at larger distances through back-scattering modulation [9]. With the use of this Hybrid RFID tag and the NEXRAD radar network, Ornithologists would able to track bird migration patterns. However, the proposed antenna used for the Hybrid RFID tag was a ceramic prepackaged antenna from Johanson with a 0-2 dBi gain and a measured return loss of 9.5 dB [8]. Considering these antenna specifications, it will be worth designing an antenna that can exceed these specifications and allow for a more adaptive antenna that can be applied to several different sizes of birds. Furthermore, this thesis will focus on creating such an antenna for the Hybrid RFID tag to provide Ornithologists with an adaptive solution to track and collect data on bird migrations.



(a)

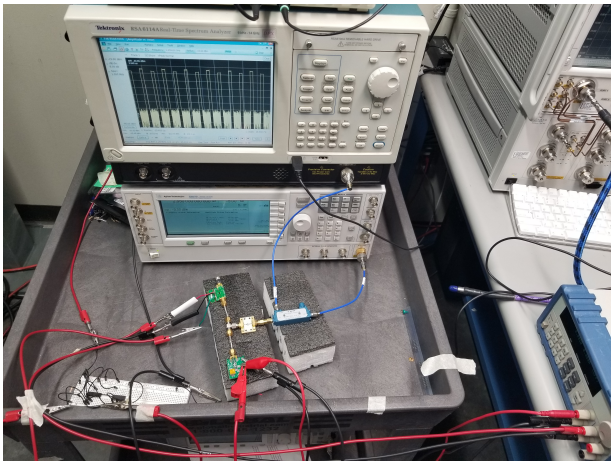

(b)

Figure 1.4: (a) WSR-88d Weather Radar that is part of the Next-Generation Radar (NEXRAD) network [9]. (b) Original Hybrid Active-Passive RFID circuit prototype under test from [8].

In order to move forward with this novel proposition, it is important to investigate previous RFID antennas with a few search constraints. The first constraint is that the RFID antenna must have a radiation pattern that is omnidirectional in the azimuth due to the horizontal orientation of the bird's body during flight. For the Second constraint, it will need to be able to mount a bird without physically constraining the bird's movement. We are only able to add no more than 3 to 5 percent of a bird's weight [1]. With these constraints, there were very few relatable RFID antenna designs. From previous work, a Low-profile antenna was created to have an elevated toroid radiation pattern to act as a Reader for vehicle registration [10]. The elevated toroid radiation shape would prove useful for this application since it is omnidirectional in the azimuth. However, the antenna read is composed of an inverted F antenna with a suspended circular cap while also having a ground plane that is at least 0.86λ in size [10]. Similarly, a co-planar waveguide (CPW)-fed prong-shaped patch antenna was designed for RFID applications and has an omnidirectional radiation pattern for both the elevation and azimuth planes [11]. Furthermore, a compact dipolar patch antenna was designed for a UHF RFID tag that could be mountable on metal surfaces [12]. However, although these antenna designs provide omnidirectional radiation in the azimuth plane, the antennas are impractical to mount a bird due to the 3 to 5 percent weight attachment limitation.

Therefore, in this thesis, a lightweight antenna with an omnidirectional radiation pattern in the azimuth plane will be designed to work with the Hybrid Active-Passive RFID tag. To begin this thesis, Chapter 2 will review previous literature on RFID antenna designs to narrow down key characteristics needed for a prototype. Chapter 3 will continue by forming a design prototype, based on the antenna characteristics needed, and simulate that created prototype in ANSYS's High-Frequency Structure Simulator (HFSS) software. The antenna prototype is simulated with and without a bird model to see the effect on the radiation pattern. Then, in Chapter 4 and 5, the

final antenna prototype and bird model are fabricated for testing. Chapter 6 discusses the measurements and results of the antenna prototype as well as testing it with the Hybrid RFID tag. Finally, in Chapter 6, this thesis will conclude with the analysis of the final fabricated antenna prototype and recommendations for continuing research on this topic.

Chapter 2

Formulating Design Requirements

2.1 Introduction

In this chapter, the antenna characteristics and design requirements will be formulated and justified for this application while also analyzing previously designed RFID antenna based on these design requirements. These previously designed RFID antennas will be analyzed and compared to the design requirements to understand what antenna characteristics could work. This chapter will also serve as a basis to formulate modified antenna designs, based on the design requirements and typical omnidirectional antennas, that can be designed and simulated in Chapter 3.

2.2 Formulating Design Requirements

To investigate possible antenna solutions for this application, there must be some requirements set to narrow down the search. To formulate these design requirements, specific bird tracking challenges need to be discussed. In [13], a study was done where fifty Savannah Sparrows were radio-tagged to track fledgling survival in Southwestern Ontario. Out of those fifty Savannah Sparrows deployed, three became entangled due to the antenna of the radio tag which resulted in two birds having minor injuries and

one bird resulted in death due to being entangled too long [13]. This leads to the first notable requirement for this designed antenna is that it will need to be able to mount on a bird without affecting the bird's natural environment. Another bird tracking challenge is that the size radio tag will determine what size birds can be tracked and what radio tag technology can accomplish this. For example, in [14], a study was done to collect data on various Hummingbird' mass, however, the size of the Hummingbird made it a difficult challenge. The size of the Hummingbird restricted what tracking technology could be used because they could only use 3% or less of the bird's weight for the radio tracking device. This led to a solution that a passive RFID tag (PIT tag) would be the best tracking device due to its low weight since it did not need a battery and had an appropriate size of 7 mm in length. This study was ultimately done by having a weight scale with an RFID reader at each feeding station and utilizing RFID PIT tags to identify each hummingbird to the recorded weight from the scale [14]. With this in mind, the proposed antenna and the Hybrid RFID circuit tag will also need to consist of a combined total weight of less than 5 percent of the bird's total mass. Since there is no classification of birds being targeted, the proposed antenna and Hybrid RFID circuit tag will need to be as small as possible to be able to track small birds. An analysis of what size birds can be tracked with the final antenna prototype will be discussed in a later chapter.

Besides, another challenge of tracking birds is maintaining the correct orientation of the radio tracking device with respect to its maximum power transmitting direction. For example, for this application, since the Hybrid RFID circuit tag will backscatter RF energy from the WSR-88D weather radar, the antenna orientation will determine where the radiation nulls are oriented. Assuming that the bird's body orientation remains horizontal, with respect to the weather radar during flight, an omnidirectional radiation pattern will be needed in the Azimuth plane. This is illustrated in Figure 2.1. Having

this omnidirectional radiation pattern in the azimuth plane serves as another design requirement because it will help avoid having nulls pointing towards the weather radar, which will decrease the chances of losing data. With these design requirements clearly defined, possible antenna solutions can be investigated and be designed as needed.

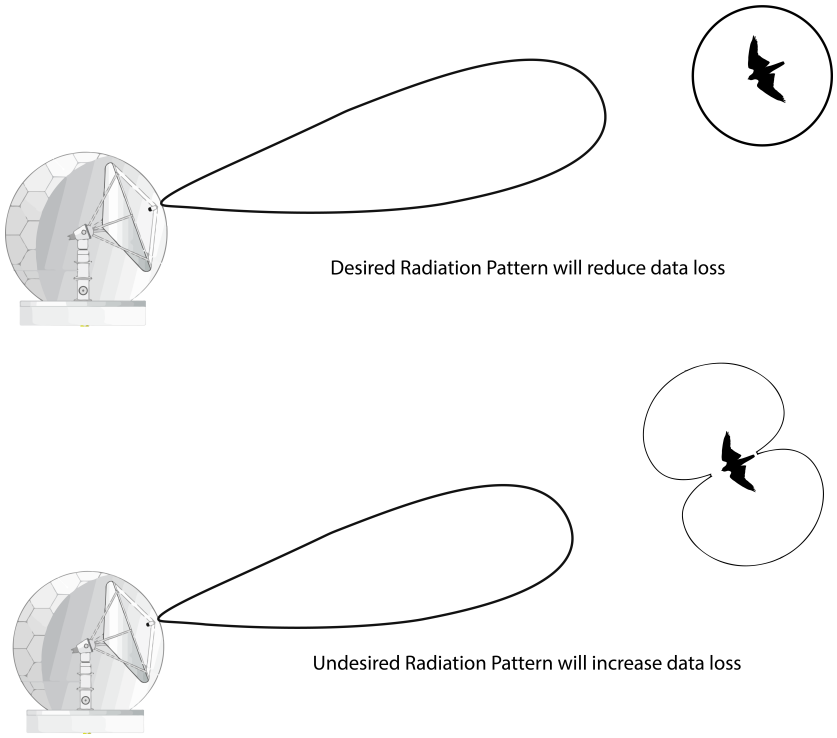

Figure 2.1: Illustrative comparison of an omnidirectional (desired) and a non-omnidrectional (undesired) radiation pattern with respect to the radar

2.3 Previous RFID Antennas

With the design requirements in mind, few previously designed RFID antennas coincide with the characteristics needed for this application but fail to meet all requirements. One of those being a low-profile antenna that enables vehicle communication through the use of RFID technology [10]. This low-profile antenna design, which consists of an Inverted F radiator, a circular cap, and a slotted ground plane, was designed to be

installed on the road and acts as an RFID reader as cars pass by with RFID tags on the registration plates [10]. The radiation characteristics of the simulated antenna consist of an elevated toroid shape, which is omnidirectional in the Azimuth plane, with 1.4 dBi of gain [10]. In Figure 2.2, the constructed low-profile antenna is shown along with the normalized radiation pattern. With an elevated toroid-shaped radiation pattern, the low-profile vehicle registration antenna does meet the radiation requirement needed for this application. However, as shown in Figure 2.2, this antenna would not be practical to mount on a bird ergonomically since the diameter of the ground plane is 0.86 λ, which is 280 mm at an operating frequency of 923 MHz [10]. Also, this antenna would not be able to meet the weight requirement needed for this application.

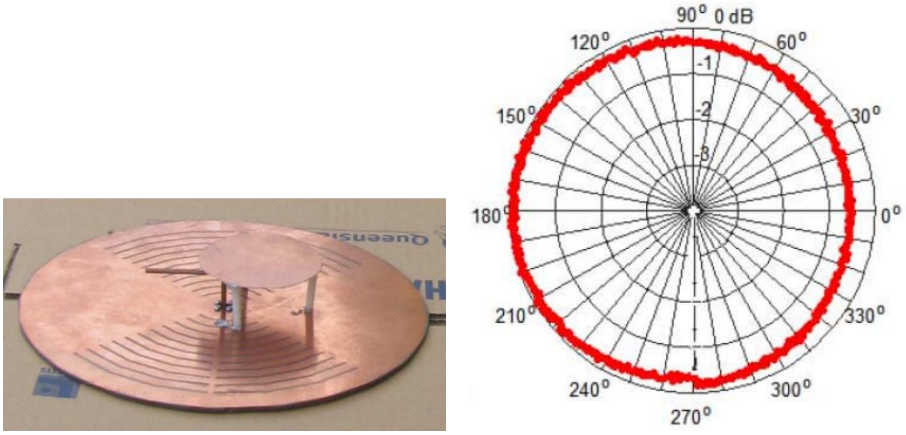

(a) (b)

Figure 2.2: (a) Photo of the Low Profile Antenna prototype; (b) Normalized measured azimuthal radiation pattern of the Low Profile antenna from [10]

Another previously designed RFID antenna would be the compact dipolar patch antenna. The compact dipolar patch antenna was designed for the Ultra High Frequency (UHF) range and was meant to be mounted on metal surfaces [12]. This compact patch antenna consists of two pairs of orthogonal dipolar patches and is inherently

placed in the nulls of each other, which eliminates the nulls from the radiation pattern in the azimuth plane [12]. This particular patch antenna would be advantageous for this application for a couple of reasons. The first reason is that the patch antenna is relatively small enough to mount onto a bird due to it's dimensions of 30 mm x 300 mm x 1.6 mm (0.0915λ x 0.0915λ x 0.0049λ) [12]. The second reason would be the lack of radiation nulls in the azimuth plane when mounted on metal [12]. A picture of the compact dipolar patch and its tag radiation sensitivity is shown in Figure 2.3. However, although the antenna meets the radiation and size constraints, there are a few barriers that make it impractical for this application. First, this compact patch antenna is designed to be mounted on metal and not on a dielectric material (such as a bird). Second, the feeding methods for a patch antenna, such as probe fed or microstrip fed, will add additional weight due to the additional materials needed to feed the patch. Lastly, although it is relatively small, this patch antenna would not be ergonomically efficient to mount on a bird due to it being a flat surface.

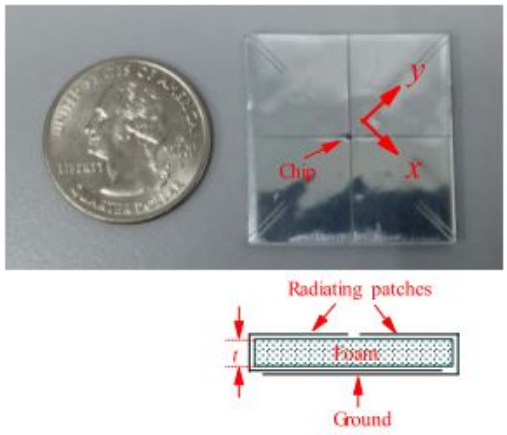

(a)

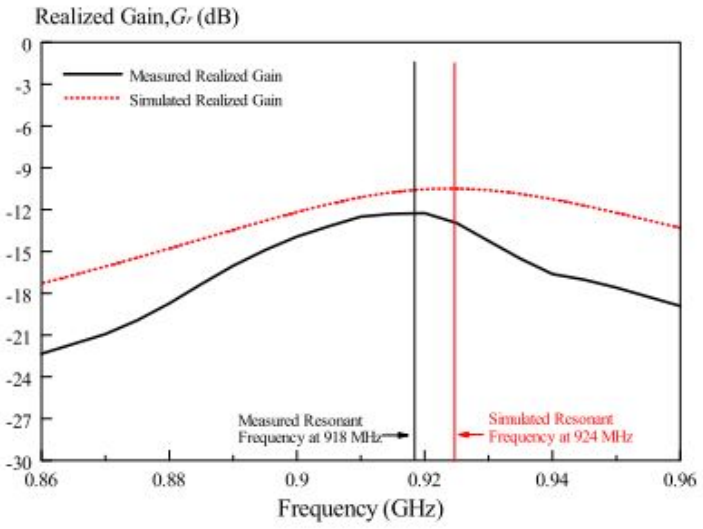

(b)

Figure 2.3: (a) Photo of the compact Dipolar Patch Antenna prototype; (b) Normalized Realized Gain of the Dipolar Patch antenna from [12]

Also, a coplanar waveguide (CPW)-fed patch antenna was another design that met some of the requirements for this application. This coplanar waveguide (CPW)-fed patch antenna was designed for RFID applications at 5.8 GHz and was designed on a 13 x 16 mm^2 FR4 substrate with a thickness of 1.6 mm [11]. This patch antenna has

an omnidirectional radiation pattern in the Azimuth plane with a gain of 4 dBi and a radiation efficiency of 98 percent [11]. With relatively small antenna dimensions and an omnidirectional azimuthal radiation pattern, both shown in Figure 2.4, this antenna can be used for this application. However, this antenna would prove impractical to mount on a bird because it is a flat surface antenna. This would also not be ergonomically efficient when mounting on smaller birds.

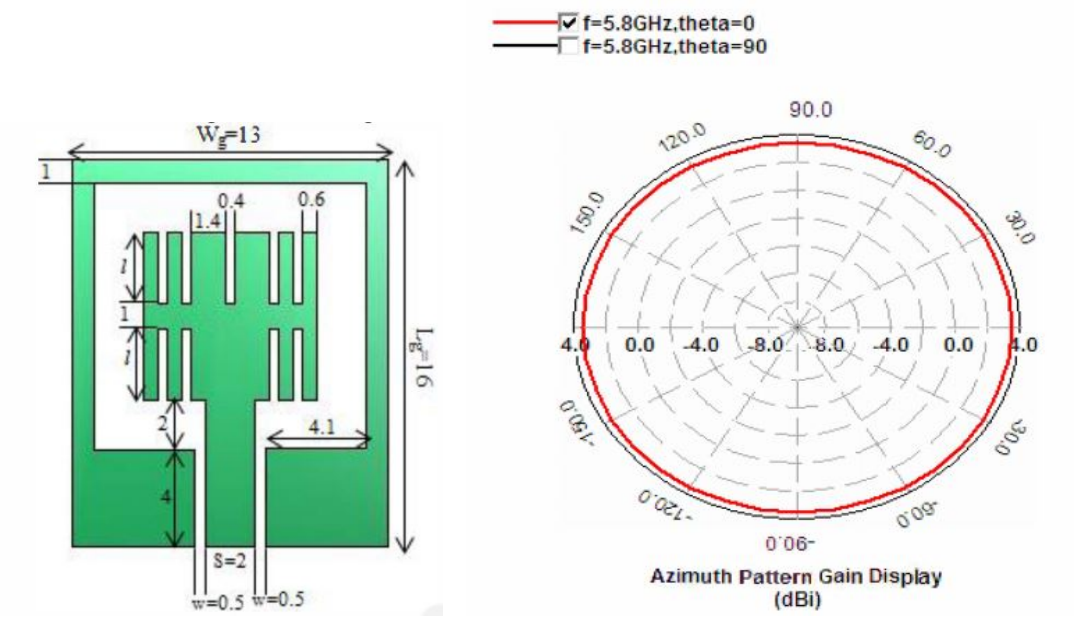

(a) (b)

Figure 2.4: (a) Geometric Shape and dimensions of the coplanar waveguide-fed patch antenna; (b) Azimuth Gain radiation pattern of the coplanar waveguide fed patch antenna from [11]

Lastly, an antenna designed for passive UHF RFID tags was designed to not be read-orientation sensitive when placed on the corner of cardboard boxes [15]. The 3D antenna consists of planar dipoles, whose arms are orthogonal, and is designed to provide near omnidirectional radiation in every direction [15]. Additionally, this RFID tag antenna has a total length of 3/4 of a wavelength and can be manufactured the

same way as regular planar thin label RFID tags [15]. In Figure 2.5, the geometry of the planar dipoles is shown and placed on a box for the prototype while Figure 2.6 displays the radiation patterns of the E-plane and H-plane, respectively. By having near omnidirectional radiation in all directions, this antenna would be beneficial to apply to this particular application. However, this antenna provides several limitations that prevent it from being applicable. First, the antenna is designed to have two orthogonal planar dipoles, which limits the possibility of mounting it onto a bird ergonomically without affecting its radiation pattern. Second, since this antenna is 3/4 of a wavelength in length, this would limit what size bird we could mount this to at 2.85 GHz.

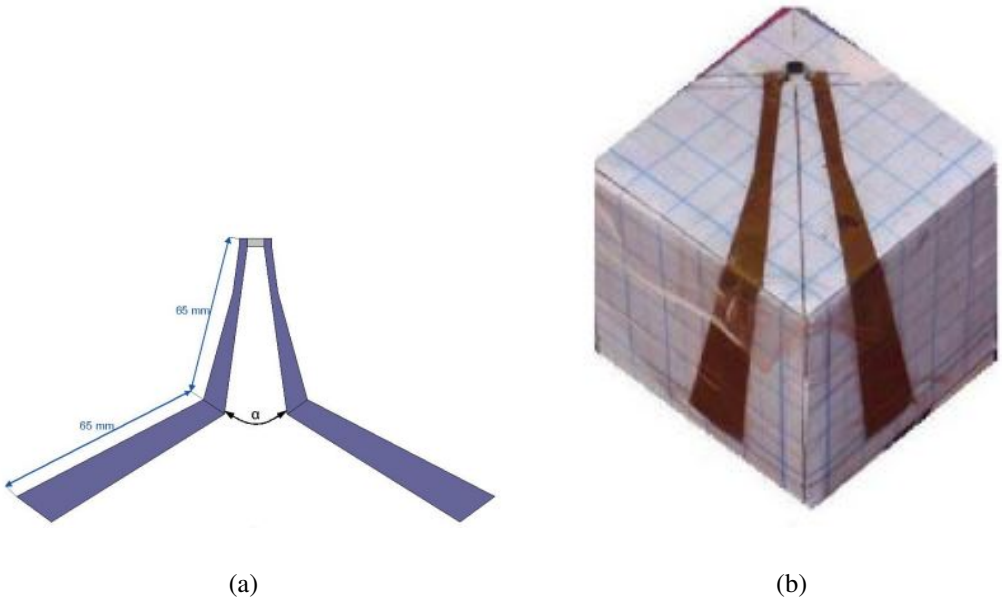

(a) (b)

Figure 2.5: (a) Geometry of the 3D antenna; (b) prototype of the 3D antenna placed on a box from [15]

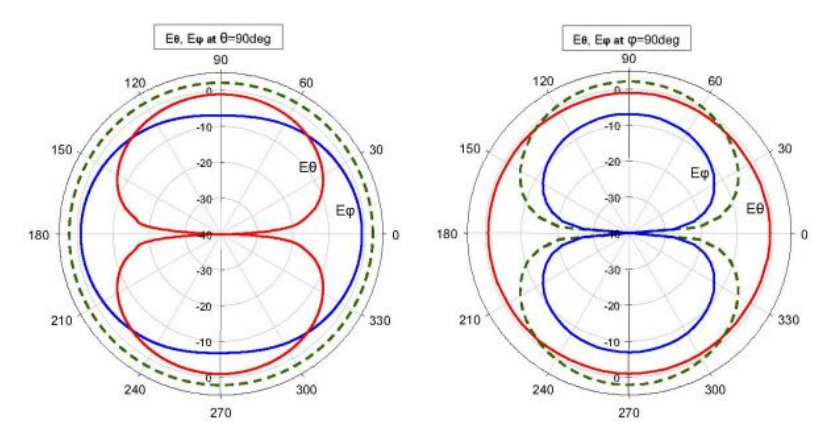

Figure 2.6: Radiation Patterns of the 3D antenna (solid lines) compared to a simple planar dipole (dashed lines) in E-Plane and H-plane, respectfully from [15]

Although all of the previously mentioned RFID antennas have the appropriate omnidirectional radiation pattern needed for this application, they all lack the appropriate characteristics to be able to mount onto a bird and not exceed the weight constraint of 5 percent or less. Needless to say, designing an antenna for this Hybrid RFID tag would be a better suit rather than utilizing a previously design RFID antenna.

2.4 Typical Omnidirectional Antennas

Before providing possible antenna design solutions, it is important to look at typical omnidirectional antennas and how they could be modified to be a possible design solution. With the weight limitation in mind, antennas, such as Patch antennas, would not be the appropriate option due to the substrate and a ground plane adding additional weight. An option worth investigating would be wire antennas due to the structural design flexibility and low weight. A dipole and a loop antenna are two common types of wire antennas that could be modified and combined to design an antenna for the Hybrid RFID tag. A dipole antenna is an omnidirectional radiator, shown in Figure 2.7, that

has a null on each end of the dipole. A dipole antenna, without any modifications, could be a possible antenna solution to be mounted onto a bird. However, when attaching the dipole to the bird, it would have to be orientated horizontally to have the least amount of interference with the bird's natural environment. If the antenna with the Hybrid RFID tag is not mounted appropriately, it could cause the birds to get stuck in vegetation or other objects [13]. Besides, mounting a dipole horizontally would place the radiation nulls in the azimuth orientation, which would interfere with the tag reading and not meet the design requirements for this application.

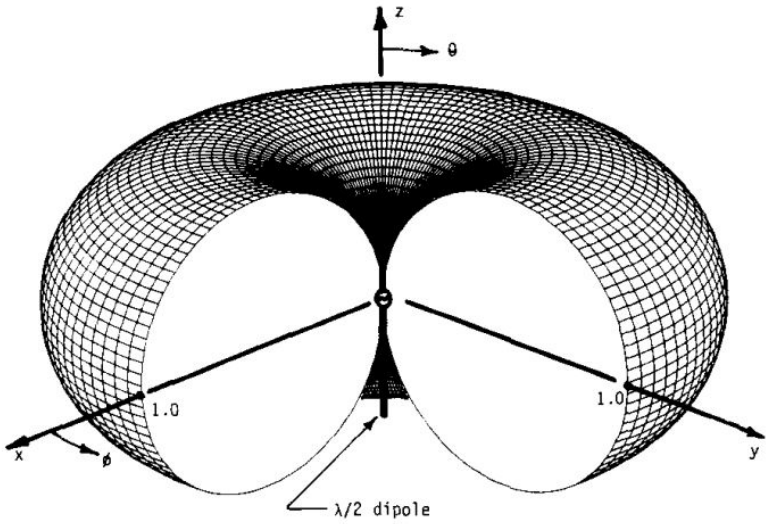

Figure 2.7: A 3D Radiation Pattern of the Halfwave Dipole antenna from [16]

In order to remove the nulls in the azimuth plane on a horizontally orientated dipole, some structural modifications must be made. A viable modification would be to curve the dipole into an "S" shape (also known as curved dipoles) to provide the omnidirectional radiation needed in the azimuth plane. Similarly, in previous studies,"S" shaped wire dipoles have shown that it provides nearly omnidirectional radiation pattern [17]. In Figure 2.8, an "S" shaped wire dipole and its corresponding radiation above a ground

plane (label P.G.) and in Free Space (labeled F.S.) is shown.

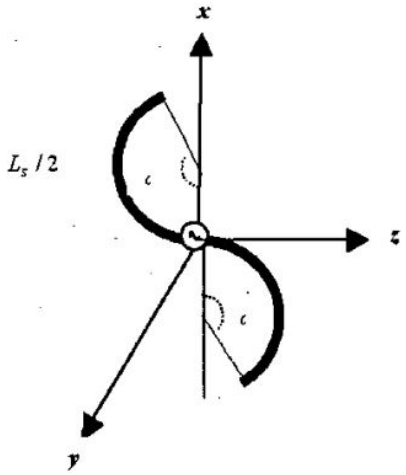

(a)

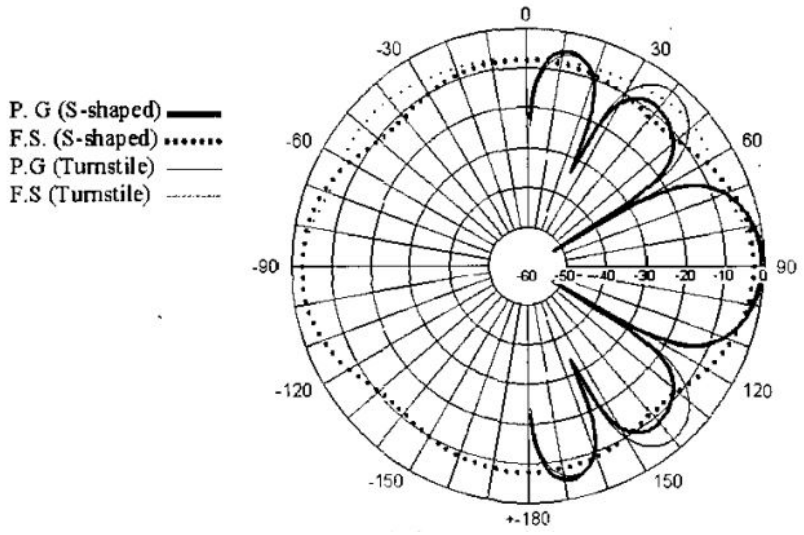

(b)

Figure 2.8: (a) Geometry of the wire S-Shaped Dipole antenna; (b) Radiation pattern on the x-y plane for the S-Shaped Dipole from [17]

Similar to the dipole antenna, the loop antenna is an omnidirectional radiator with two nulls perpendicular to the loop, which is shown in Figure 2.9. This loop antenna, instead of making structural modifications, could be used how it is to help mount onto

a bird due to its opening in the middle of the loop. This loop opening will allow the bird to fit in and be able to ergonomically mount onto a bird. The loop antenna could also be used in combination with the curved dipole to satisfy the design requirements.

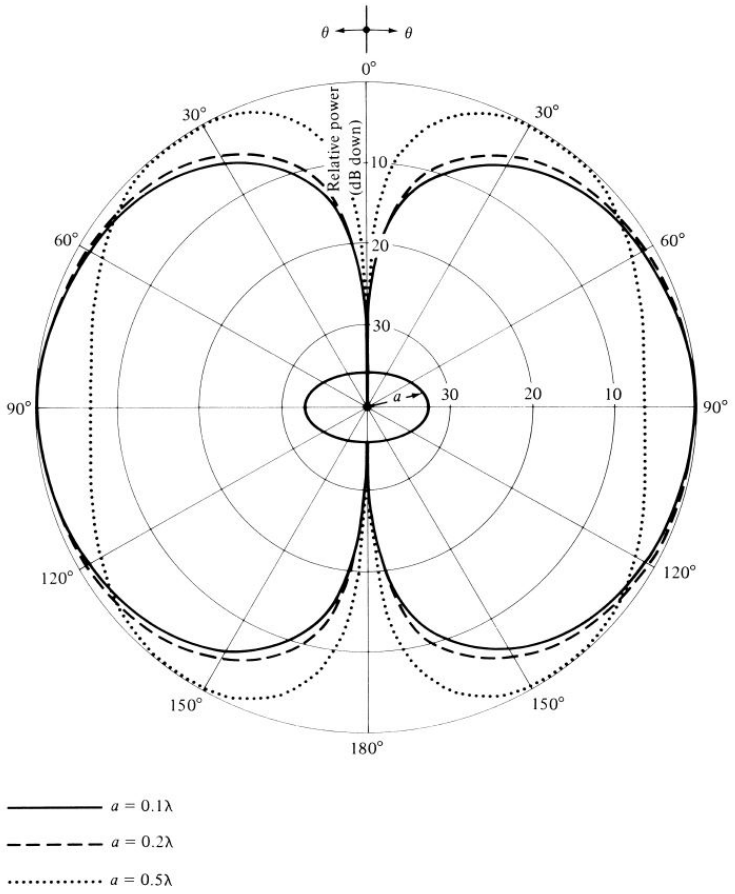

Figure 2.9: Radiation Pattern of the loop antenna from [18]

2.5 Conclusion

In this chapter, general design requirements were established to help investigate different antenna design solutions. These design requirements were compared to previously design RFID antennas to understand what has been considered and to understand what types of antennas to investigate as possible solutions. With these previously inves-

tigated antennas, typically omnidirectional antennas were discussed and analyzed as possible solutions. Certain typical omnidirectional antennas, such as the wired Dipole and the loop antenna, can be modified to meet the basic design requirements. In the next chapter, a combination of crossed loop antennas and an S-shaped dipole will be further investigated and justified for a specific size of birds based on specific antenna parameter requirements.

Chapter 3

Antenna Parameters and Limitations

3.1 Introduction

In this chapter, the theoretical antenna parameters and size limitations will be discussed in detail. A baseline for how small the desired antenna can be theoretically will be determined using the Antenna Quality factor and the maximum achievable gain. Afterward, a material and weight analysis will be discussed and then Incorporated with the weight analysis of the proposed Hybrid RFID tag. Also, with newly proposed components and slight modifications, a final material and weight analysis will be made to see what size bird can be tagged while also meeting the 5% weight limitation.

3.2 Antenna Size Limitation

3.2.1 Minimum Antenna Quality Factor

One of the most challenging antenna design aspects is making the antenna as small as possible without affecting its performance. Electrically Small Antennas are often the solution to many modern communication system applications that require low-volume and low-profile antennas since they are much smaller than the operating wavelength. Electrically Small Antennas, as defined by Wheeler, are smaller than a radian-sphere,

which is the boundary between the near field and far-field, with radius r and $\beta r = 1$ [19], [20]. In Figure 3.1, a capacitor-plate dipole antenna is enclosed within a radian-sphere. Thus, Electrically Small Antennas typically satisfies $\beta a \leq 1$ [20]. However, Electrically Small Antennas are fundamentally limited by the Bandwidth and Quality Factor of the Antenna. Antenna Quality Factor (Q_A), assuming the antenna is tuned to a resonant frequency and lossless, equals radiation Q and can be defined as

$$Q_A = \frac{2\,\omega\,\max[W_{e_{av}}, W_{m_{av}}]}{P} \tag{3.1}$$

where $W_{e_{av}}$ and $W_{m_{av}}$ are the time-average stored electric and magnetic energies, ω is the angular frequency and P is time-average radiated power [20].

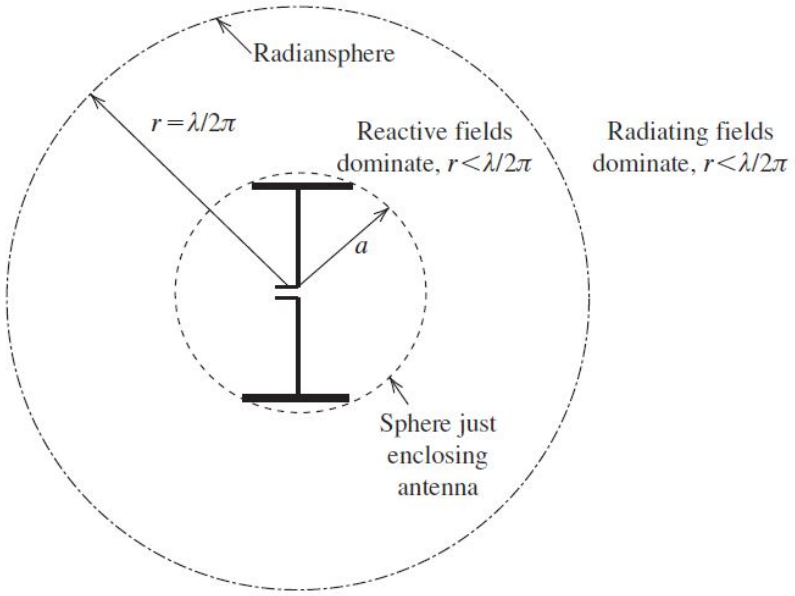

Figure 3.1: Capacitor-plate dipole antenna enclosed within a radian-sphere from [20]

Since the purpose of this thesis is to design an antenna suitable for the Hybrid RFID tag, the time-average stored electric and magnetic energies and the time-average radiated power are not yet known. However, since the bandwidth of the desired antenna

is known, the Quality Factor of the antenna can be calculated. In fact, the Quality Factor (Q_A) is related to the Fractional Bandwidth (FBW) as $FBW = \frac{1}{Q_A}$ [21]. Since the desired bandwidth band of the antenna is 2.7 GHz to 3 GHz (300 MHz of Bandwidth), the Fractional Bandwidth is calculated as

$$FBW = \frac{BW}{f_c} = \frac{3GHz - 2.7GHz}{2.85GHz} = 0.105 \tag{3.2}$$

and is then used to find the Antenna Quality Factor by

$$Q_A = \frac{1}{FBW} = \frac{1}{0.105} = 9.524 \tag{3.3}$$

In [20], it is stated that the minimum Quality Factor can be expressed as

$$Q_A = \frac{1}{\beta^3 a^3} \tag{3.4}$$

where β is the phase propagation constant ($\beta = \frac{2\pi}{\lambda}$) and a is the radius of the sphere enclosing the antenna. Since the antenna size is directly related to the radius of the sphere enclosing the antenna, Equation 3.4 can be rewritten as [20]

$$a = \sqrt[3]{\frac{1}{\beta^3 Q_A}}. \tag{3.5}$$

Using the previously calculated values from Equations 3.2 and 3.3, it can be approximated that the minimum antenna size is $a > 0.15\lambda$, which is a radius of 15.76 mm (31.5 mm in diameter) at 2.85 GHz. In Figure 3.2, it is shown that with an increase of Fractional Bandwidth, the minimum antenna size must also increase. This minimum antennas size can be used to predict what size birds can be tagged with a Hybrid RFID tag, which will be discussed in detail later in this chapter.

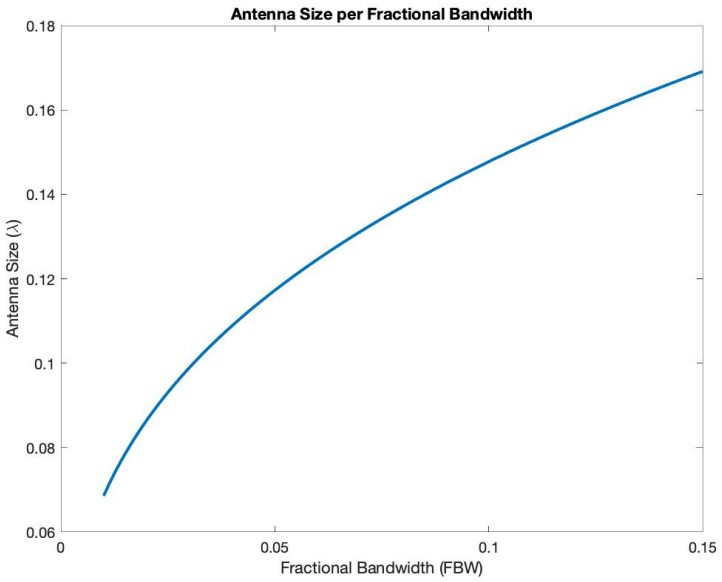

Figure 3.2: Antenna Size per Fractional Bandwidth

3.2.2 Maximum Theoretical Gain per Kilometers

To get a more accurate understanding of the limitations of the antenna size, the realized gain of the antenna must be considered concerning the calculated Quality Factor in Equation 3.3. However, by extracting the size of the antenna with Equation 3.5, we can directly use this to find the max attainable gain of the antenna. In fact, in [21], the corresponding approximate gain of an omnidirectional antenna for a given Quality Factor is defined as

$$G \approx \frac{2}{\pi} \times \frac{2\pi a}{\lambda} = \frac{4a}{\lambda} \tag{3.6}$$

where λ is the free-space operating wavelength and a is the radius of the sphere that encloses the antenna. By utilizing Equations 3.6 and 3.5, it can be stated that the maximum theoretical Gain for an antenna size of 0.15λ is approximately -2dB, which is shown in Figure 3.3(a). Since 0.15λ is the minimum antenna size, the larger the an-

tenna gets the more antenna gain can be theoretically achieved. In Figure 3.3(b), the theoretical achievable antenna gain and bandwidth is shown for a given antenna size, with a dashed line indicating the antenna size at 0.15λ.

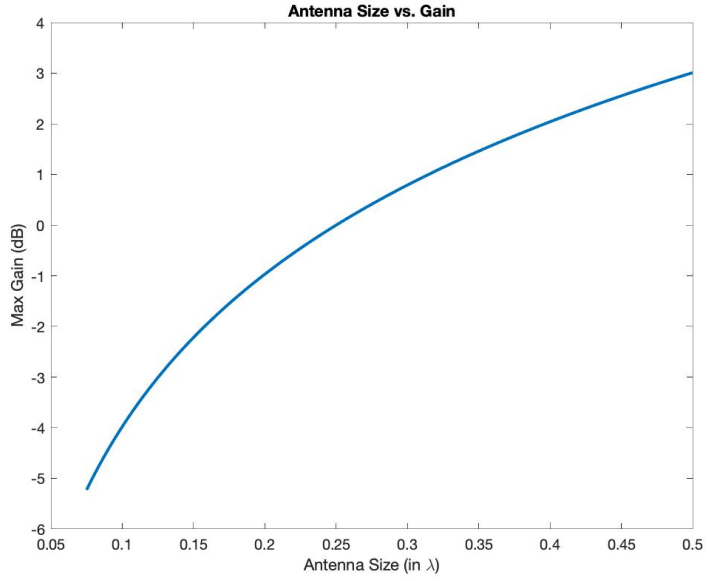

(a)

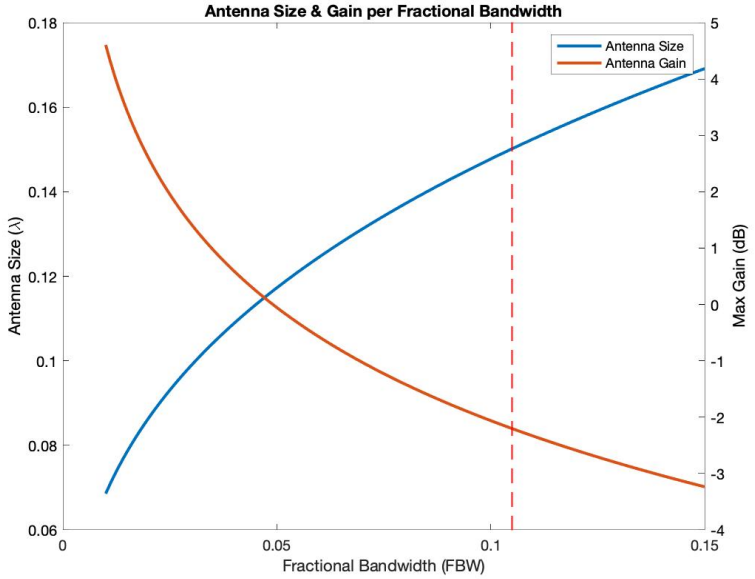

(b)

Figure 3.3: (a) Antenna Size per Realized Gain; (b) Antenna Size and Realized Gain per Fractional Bandwidth

Now that there are concrete theoretical parameters, such as realized gain, size, and bandwidth, the maximum detectable range can be calculated using the Radar Range equation. In [22], one version of the Radar Range equation that is suitable for mono-static system and the available parameters is expressed as

$$R_{max}^4 = \frac{P_t G_t A_e \sigma}{(4\pi)^2 k T_o B F_n (S/N)_{min}} \tag{3.7}$$

where P_t is the transmitted power, G_t is the gain of the transmitter/receiver, A_e is the antenna aperture of the transmitter, σ is the Radar Cross Section of the receiver, k is the Boltzmann's constant, T_o standard room temperature, B is the bandwidth of the transmitted signal, F_n is the Noise Figure, and $(S/N)_{min}$ is the minimum Signal-to-Noise ratio. The following parameters listed in Table 3.1 have been calculated and found in the datasheet of the WSR-88d radar [9]. It should be noted that the bandwidth of the transmitted signal is not explicitly listed in [9], however it can be calculated by knowing the pulse width of the signal which is listed. Since the WSR-88D radar transmits in short (1.57 microseconds) and long pulses (4.71 microseconds), the signal bandwidth was found by taking $\frac{1}{\tau}$, where τ is the pulse width of the short pulse.

Table 3.1: Radar Range Equation Input Parameters

Transmit Power (kW)	P_t	700
Transmitter/Receiver (dB)	G_t	45.5
Antenna Aperture (m^2)	A_e	31.29
Boltzmann's constant (J/K)	k	1.38×10^{-23}
Room Temperature (K)	T_o	290
Bandwidth ($\frac{1}{\tau}$)	B	6.37e5
Noise Figure (dB)	F_n	2.7
Minimum Signal-to-Noise (dB)	$(S/N)_{min}$	0

The only parameter that is not listed in Table 3.1 is the Radar Cross Section (σ) of the tag. Since the Hybrid RFID tag has active components, such as the RF switch, the radar cross-section will vary depending on which state it is in. The Radar Cross Section for a modulated backscatter application is defined as

$$\sigma_{RCS} = \frac{\lambda^2 G_t^2}{4\pi} |\Gamma_{A,B}|^2 \tag{3.8}$$

where λ is the wavelength at the operating frequency, G_t is the gain of the tag antenna, and $\Gamma_{A,B}$ is the reflection coefficient at the antenna for state A or state B [23]. In [8], it is stated that the Hybrid RFID tag has an RF switch that allows the tag to switch between a reflective state with the closed switch and an absorbing state with the open switch. It can implied that an ideal reflection coefficient for the reflective state is $\Gamma_{A,B} = 1$ while the absorbing state is $\Gamma_{A,B} = 0$. A more accurate representation of the reflection coefficient can be correlated to the Modulation factor. In [8], the modulation factor used is $M = 0.25$, which will be used in place of $|\Gamma_{A,B}|^2$ term in Equation 3.8. Besides, it is important to note that the Hybrid RFID tag has an amplifier for the input signal to

have enough power to switch off the counter. With this amplification of roughly 6 dB, stated in [8], we can account for this additional gain in Equation 3.8 by splitting the G_t^2 term into $G_{t1} \times (G_{t2} + 6dB)$. By doing this, we can account for the amplification gain of the system by adding it to one of the Gain terms. With all the parameters known for the Radar Range equation, the approximate Gain per kilometer is determined in Figure 3.4. The relationship between theoretical antenna gain versus range, with a mark at the -2dB for both the realized gain and the realized gain including the amplifier gain. It is shown, in Figure 3.4, that there is an increase of approximately 46 kilometers by including the amplification of the gain. The max range per realized gain is also plotted across various modulation factors to see how that affects range in Figure 3.5.

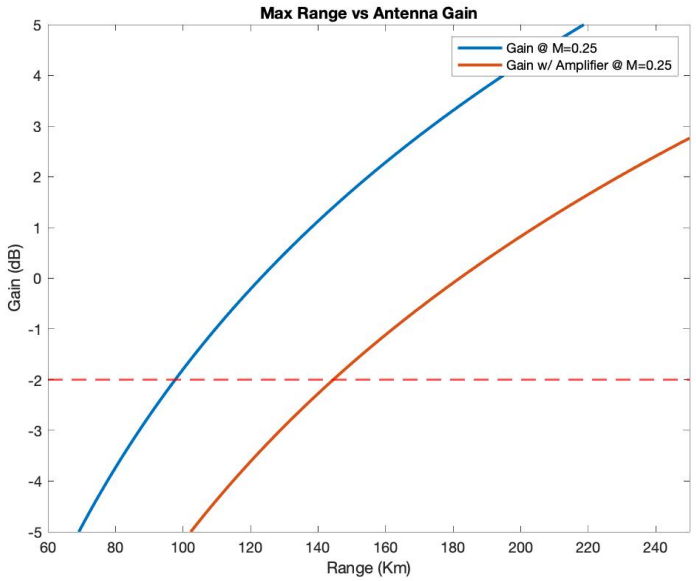

Figure 3.4: Max Range per Realized Gain

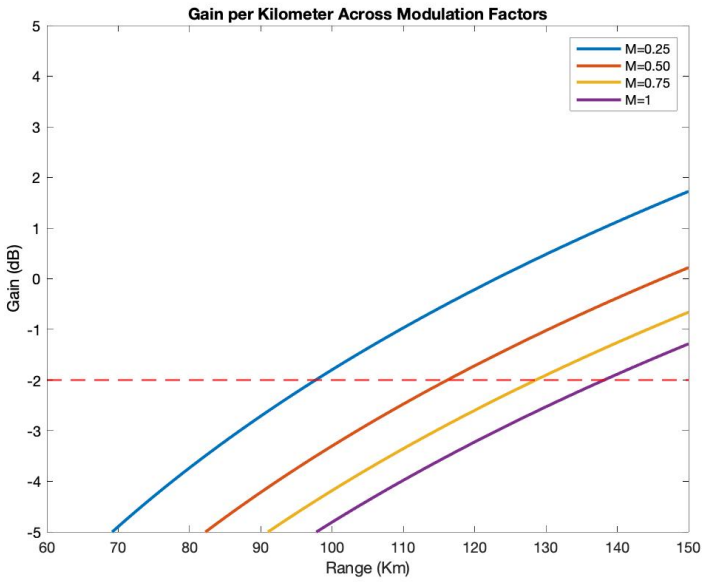

Figure 3.5: Max Range per Realized Gain Across Modulation Factors

Also, to put it more in perspective, Figure 3.6 shows what the theoretical range would be for an antenna with -2dB of realized gain (with and without the amplifier gain) on a google maps image starting at the location of the NEXRAD WSR-88d Radar. The Black ring, in Figure 3.6, is the max range at 144 kilometers, which includes the amplifier gain, that the Hybrid RFID tag would be able to be read by the radar while the red ring is the max range at 97 kilometers, which does not include the amplifier gain.

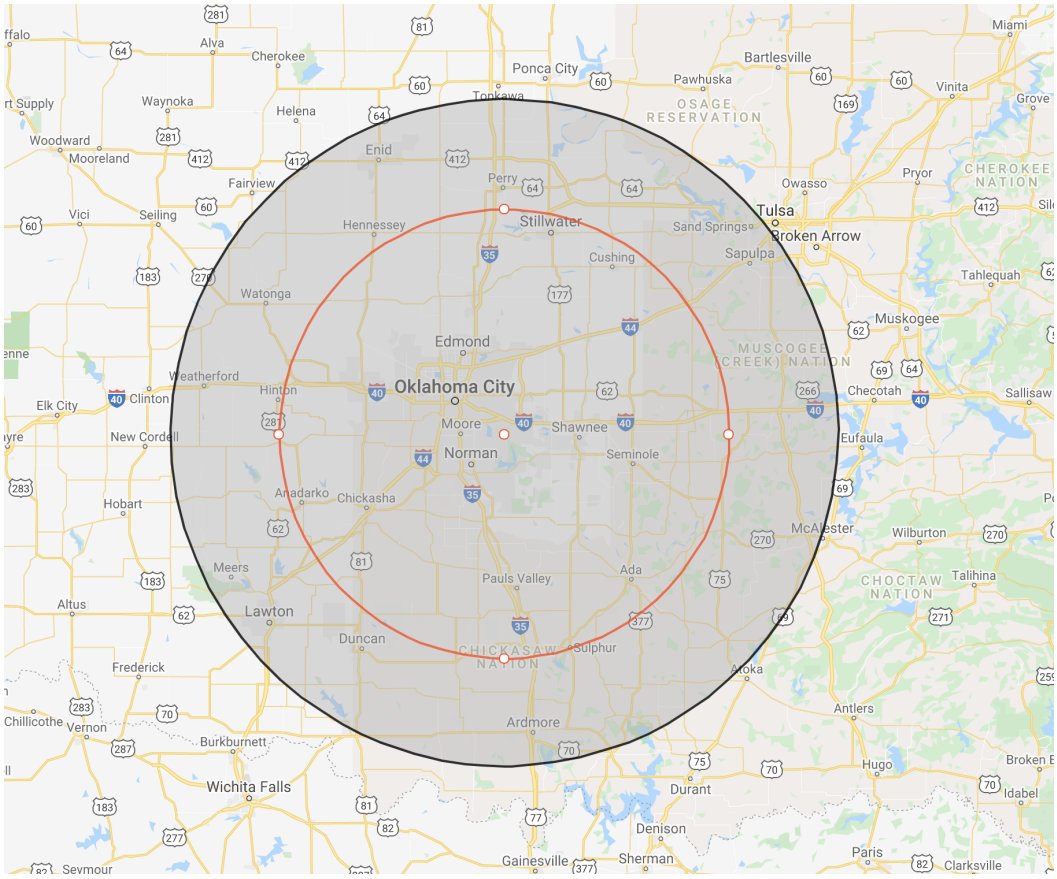

Figure 3.6: In Black: Range at 144 Kilometers; In Red: Range at 97 Kilometers

3.3 Achievable Bird size tagging

With an understanding of how small the designed antenna can be, the size of the bird that can be tagged can also be determined by analyzing the weight of the tag components and the material used for the antenna. For the Hybrid RFID tag, the size and weight of the proposed components have been determined in [8]. In Table 3.2, the weight of each selected component for the Hybrid RFID tag is listed. In [8], it is stated that the total weight of the selected components combined with the weight of the proposed 30 mil 1"x1.5" FR4 board is 10.988 g.

Table 3.2: List of Components and their corresponding weight for the Hybrid RFID Tag from [8]

Part Description	Part Number	Weight (g)
RF Switch	HMC550ae	0.016
Envelop Detector	LTC5505-2	0.012
Binary Counter	SN74HC393NSR	0.2
Quad-Amplifier	LM324AN	0.260
Watch Battery	ECR2450	6.8
Battery Holder	BU2450SM-JJ-GTR	2.37
FR4 Board	N/A	1.33

Since the smallest calculated theoretical antenna size is 0.15λ with a bandwidth of 2.7 GHz to 3 GHz, the following weight analysis will consider this as the minimum size the antenna may be. In addition to the antenna size, the antenna design will also constitute how much material is needed. It was decided that the amount of material needed to construct the crossed loop antenna design was set as the baseline. Copper wire and stainless steel memory wire was chosen as probable material used to construct the antenna. For the crossed loop design, with five turns to construct the loop and utilizing 0.15λ (at 2.85 GHz) as the diameter of the loops, the length of material needed is approximately 500 mm of wire. With all of these parameters, Table 3.3 shows the calculated weight of both copper wire and stainless steel memory wire at 22 gauge and 20 gauge, which were arbitrarily chosen as the initial gauge for this weight analysis.

Table 3.3: Weight Comparison between Copper and stainless steel memory wire

Wire Gauge	Copper wire	Stainless Steel Memory wire
22 AWG	1.45 grams	0.45 grams
20 AWG	1.755 grams	0.545 grams

With these antenna weight variations in mind, an approximate calculated weight for the Hybrid RFID tag can range between 11.44 grams and 12.74 grams. Since the Hybrid RFID tag has to be less than 5% of a bird's body weight, this implies that the minimum weight of a bird has to be between 228.8 g and 254.8 g to be able to tag it. In Figure 3.7, the different weight classes of birds in comparison to what current tracking technology can be used, which also satisfy the less than 5% weight requirement, is shown. In comparison with that figure, the current approximate weight of the Hybrid RFID tag only allows large birds to be tagged without exceeding the weight limit.

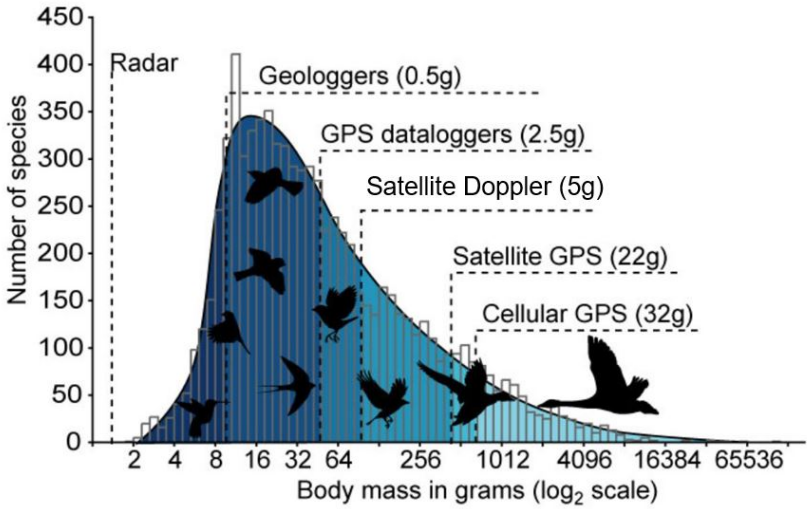

Figure 3.7: Weight Classes of Birds with current tracking technology

With future work in mind, the Hybrid RFID Tag can be modified slightly to reduce weight and allow smaller birds to be tagged. To start, the current design for the tag

utilizes a surface mount Quad-Amplifier that weighs approximately 0.260 g. Since the design only utilizes an amplifier to amplify the input signal into a digital binary counter, there was no need for the additional amplifiers. A simple replacement with a single amplifier surface mount chip (Part Number: MCP6001) would be a quick solution. A single Operational Amplifier that can operate at $3.0V$ and utilizes 100 μA for the supply current can be used instead of the Quad-Amplifier surface mount that was suggested in [8]. This single amplifier surface mount chip also has a significantly lower unit weight at 0.0063 g, which is listed on Mouser's website.

The weight of the Board can also be reduced by utilizing a flex board material rather than FR4 board material. Flex circuit boards can be beneficial especially when designing for low size constraints and low weight constraints, which make them particularly useful for this application. The flex circuit board can be fabricated with multiple layers for a variety of applications. However, since this application calls for the lowest weight possible, it is decided that the proposed flex circuit board be constructed out of a single layer. With this in mind, all Flex Inc. is one of many companies that fabricate flex boards. This company also provides a design guide that lists design characteristics and fabrication limitations for flex circuit boards [24]. In Figure 3.8, a diagram from the design guide shows what a single layer of flex board material is made out of.



Figure 3.8: Single Layer of Flex Board Material from [24]

To determine an approximate weight of a single layer flex circuit board material with 1/2 oz copper traces, the same proposed form factor of 1.5" by 1" proposed by [8]

was used as a baseline. Also, an assumption was made that the copper layer is the main contributor to the flex board material weight. With this in mind, it is understood that 1/2 oz copper traces refers to the thickness of the copper trace when 1/2 oz of copper material is spread out on a 1' by 1' area. This thickness corresponds to 0.7 mil of copper trace thickness. With 1/2 oz being the weight of the copper material, the ratio of the 1' by 1' area and the 1.5" by 1" area was found and then multiplied by 1/2 oz. This total weight, for a form factor of 1.5 " by 1", came to be 0.15 g. It is important to note that this weight assumes only the weight of the copper layer and it assumes that the entire form factor 1.5" by 1" is covered completely with 1/2 oz copper. With that being said, it is understood that this calculated weight is a rough overestimated approximation that can be used as a baseline weight for the flex board material.

Lastly, the size and weight of the proposed battery and battery holder is another weight limitation with it being the majority weight of the Hybrid RFID tag. For future work, it is important to find a power source, whether it is a smaller battery or a single solar cell, that would provide a significantly low size and weight to the Hybrid RFID tag. This power source would be the main determining factor of the weight of the tag, which would determine the size of birds that can be tagged. With current tracking technologies in mind, finding a single solar cell for his proposed Hybrid RFID tag can be possible with further investigation. One current tracking technology called LifeTag from Cellular Tracking technologies has a weight of 0.45 g and appears to be powered with a single solar cell [25]. This LifeTag is shown in Figure 3.9. For this weight analysis, to make the tag as small and low weight as possible, it is proposed that a similar single solar cell power source, with a total weight between 0.16 g to 0.36 g or less, is used in the future for the Hybrid RFID tag. With this in mind, the newly proposed components and their corresponding weights are listed in Table 3.4.

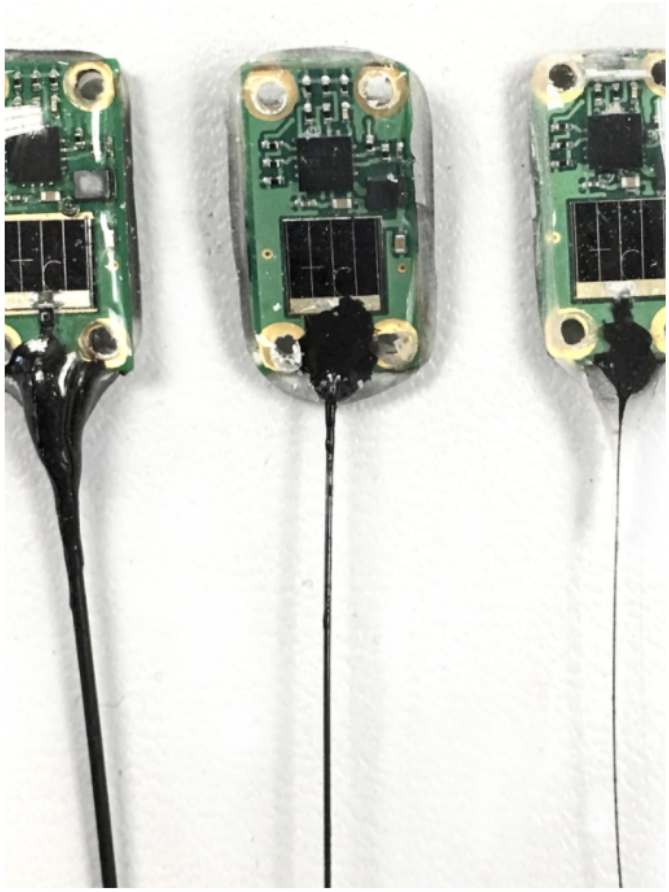

Figure 3.9: LifeTag from Cellular Tracking technologies from [25]

Table 3.4: List of newly proposed Components and their corresponding weight for the Hybrid RFID Tag

Part Description	Part Number	Weight (g)
RF Switch	HMC550ae	0.016
Envelop Detector	LTC5505-2	0.012
Binary Counter	SN74HC393NSR	0.2
Single Operational Amplifier chip	MCP6001	0.0063
Power Source	N/A	0.16 - 0.36
Flex Board Material	N/A	0.15

By adding the weight of the newly proposed components, the calculated weight range of the hybrid RFID tag (without the antenna weight) is between 0.502 g to 0.742 g. With the proposed antenna weight that was previously calculated for 22 AWG and 20 AWG copper wire, the Hybrid RFID tag has a new proposed weight between 0.952 g to 2.257 g. This new weight range is significantly less than the proposed 10.988 g proposed in [8]. With 5% weight attachment restriction, birds that weigh between 19.04 g to 45.14 g could be tagged theoretically. When referring to Figure 3.7, it is important to note that the amount of bird classifications that could be tagged has significantly increased with the new calculated weight of the Hybrid RFID tag.

3.4 Conclusion

In conclusion, a material and weight analysis was done to see what the minimum achievable bird size can be tagged and a theoretical maximum range using the Hybrid RFID tag. First, an initial theoretical antenna size was proposed by knowing the Quality factor. This proposed minimum antenna size was calculated to be 0.15λ with

a theoretical maximum range of 43 km with an antenna gain of -2 dB. Besides, once this minimum antenna size was calculated, a material weight analysis was done to see what the theoretical weight would be. With the proposed copper wire and stainless steel wire, the theoretical weight of a dipole-loop combination antenna design would be between 0.45 g and 1.755 g. This would bring the total weight of the Hybrid RFID tag to between 11.44 g and 12.74 g. However, with future work in mind, a reasonable consideration to utilize flex board, replacing the quad amplifier with a single amplifier, and with the hope that a single solar cell power supply be used (between the weight of 0.16 g to 0.36 g), this would reduce the total theoretical weight of the Hybrid RFID tag between 0.952 g and 2.257 g. This newly proposed weight, considering the proposed modification that can be done with future work, would allow tagging birds that weigh between 19.04 g and 45.14 g.

Chapter 4

Antenna Simulation Analysis

4.1 Introduction

In this chapter, the Curved Folded Dipole Antenna (CFDA), designed by Taylor Poydence in [26], is introduced and discussed how it is a good basis to start with due to its size and radiation pattern. The CFDA is also be redesigned to 2.85 GHz and analyzed to see how well it fits this thesis in terms of size and bandwidth. More specifically, bandwidth is first analyzed by looking at the frequency span of 2.7 GHz to 3 GHz and seeing if those frequency span satisfy $VSWR < 2$ by varying certain antenna dimensions. Additionally, bandwidth is also analyzed by looking at the Quality Factor of the antenna and seeing if it decreases or increases as a trend when varying those same antenna dimensions. Lastly, bandwidth will be analyzed by calculating a certain gain threshold and looking at the Realized Gain across frequency to see if the frequency span of interest is above that calculated gain threshold. With this bandwidth analysis, the CFDA will be more confidently understood and know that it satisfies the bandwidth definition chosen.

4.2 Curved Folded Dipole Antenna

To try to design an antenna that meets the design requirements, outlined in Chapter 4, an antenna designed by Taylor Poydence in [26] was used as a base structure and is further developed to meet the design requirements. In [26], Taylor designs and tests several quasi-isotropic antennas for Unmanned Aircraft System applications. To mention a couple, the Rubber Duck and Cloverleaf antenna, which are typical quasi-isotropic antennas, were simulated and analyzed the far-field realized gain. Furthermore, Taylor targeted his focus on purely planar quasi-isotropic antennas and analyzed their performance on curved structures and thin substrates [26]. The Curved Folded Dipole Antenna (CFDA), which is shown in Figure 4.1, is a planar folded dipole antenna that is circularly curved onto itself with a small gap where the ends meet and has a single feed line connection. In Figure 4.1, the Curved Folded Dipole Antenna is shown and illustrates $w1$ and $w2$ being the inner and outer width of the folded dipole, d being the gap between $w1$ and $w2$, and θ being the curvature angle of the CFDA.

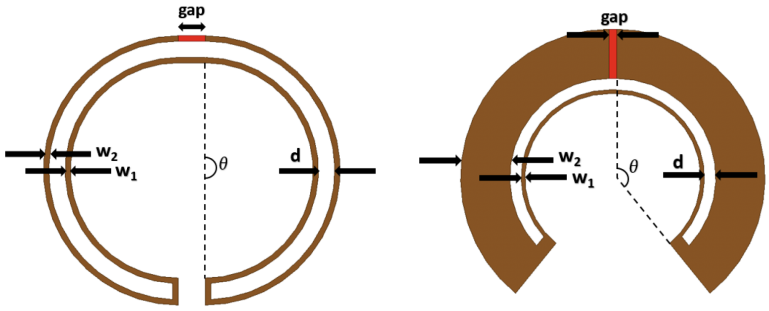

Figure 4.1: Curved Folded Dipole Antenna from [26]

In [26], the CFDA was designed to operate at 915 MHz and was analyzed to show how flexible the CFDA design is as a quasi-isotropic antenna. This analysis was done by simulating the effects of the curvature angle would have on the Peak real impedance and the radiation efficiency. This comparison was also done with and without a 10 mil

Rogers 5880 substrate. The results of this analysis are shown in Figure 4.2. Also, the return loss at selected angles was shown for the CFDA with a 50 Ω feed port in Figure 4.3.

Curvature Angle (deg)	Peak Real Impedance (Ω)		Radiation Efficiency	
	Air	Rogers 5880	Air	Rogers 5880
1.000	275.77	252.99	0.986	0.980
45.000	254.11	230.75	0.985	0.978
90.000	188.54	166.47	0.978	0.972
120.000	135.35	118.64	0.970	0.961
150.000	85.58	75.06	0.951	0.937
180.000	47.93	43.14	0.908	0.881

Figure 4.2: Curvature Analysis on Impedance and Radiation efficiency from [26]

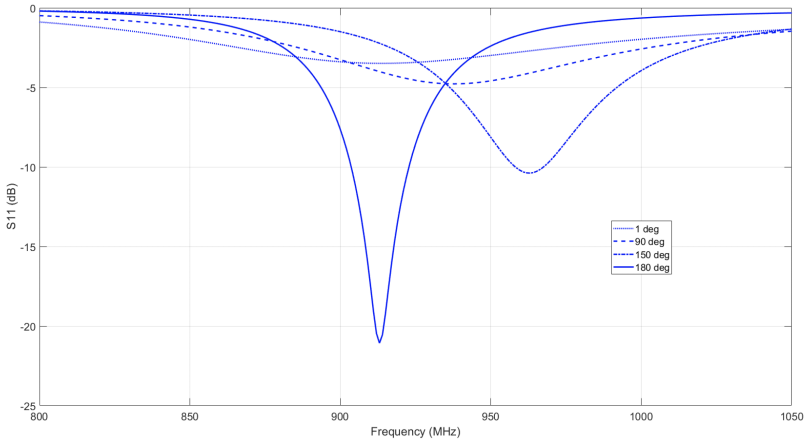

Figure 4.3: Return Loss (S11) at selected curvature angles from [26]

This curvature angle analysis was extended to the far-field radiation pattern in both the E-plane and H-plane, which was already defined in Figure 4.4 in [26]. It was shown that a trend in the H-Plane far-field radiation pattern went from a circle to an oblong pattern with an increase of curvature angle [26]. The E-plane radiation pattern nulls decreased and trended toward an oblong shape with an increase of curvature angle. These trends in the far-field radiation pattern are shown in Figure 4.5

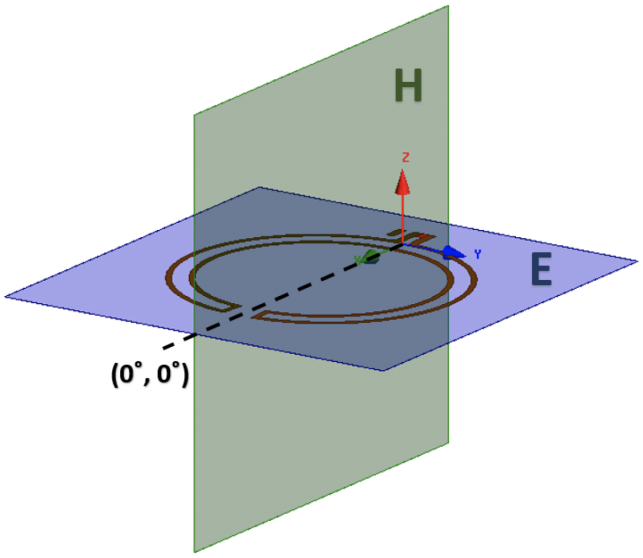

Figure 4.4: Far field radiation pattern E and H plane reference from [26]

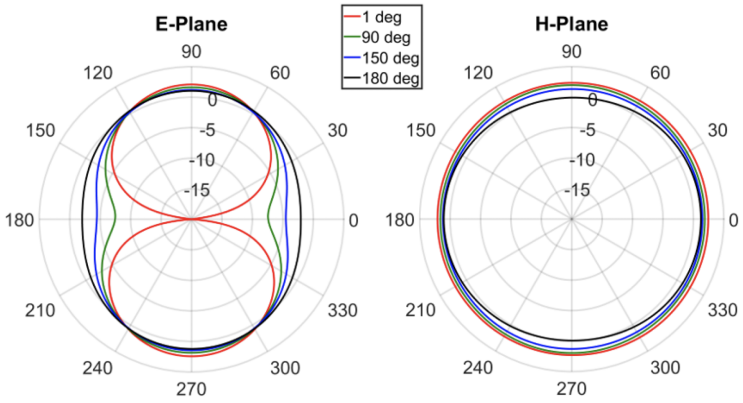

Figure 4.5: Far Field radiation pattern trends across Curvature angle from [26]

By utilizing the CFDA designed in [26], it can be used as a base structure and develop to meet the design antenna requirements for this application. This CFDA design provides several antenna parameter advantages than by designing by scratch. First, this antenna has a relatively small footprint compared to its $\lambda/2$ folded dipole footprint due

to the curvature angle θ, which for this thesis will remain at $\theta = 180$ to allow for a more omnidirectional far-field radiation pattern for the E-plane. This size difference in footprint, with a resonance at 915 MHz, can be shown in Figure 4.6. This planar CFDA can also be easily integrated onto a single-layer flex board, which will allow for better mounting positioning on a bird's body. To make this CFDA design applicable, it must meet the design requirements which include having an operational bandwidth of 2.7 GHz to 3 GHz with a center resonant frequency of 2.85 GHz (which is a Fractional Bandwidth of 10.5%), have an omnidirectional far-field radiation pattern in the azimuth plane (which would be the E-plane for how it was previously defined), and have a small enough footprint to be able to mount on a relatively small bird.

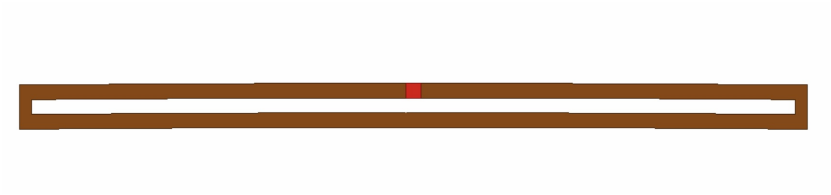

(a)

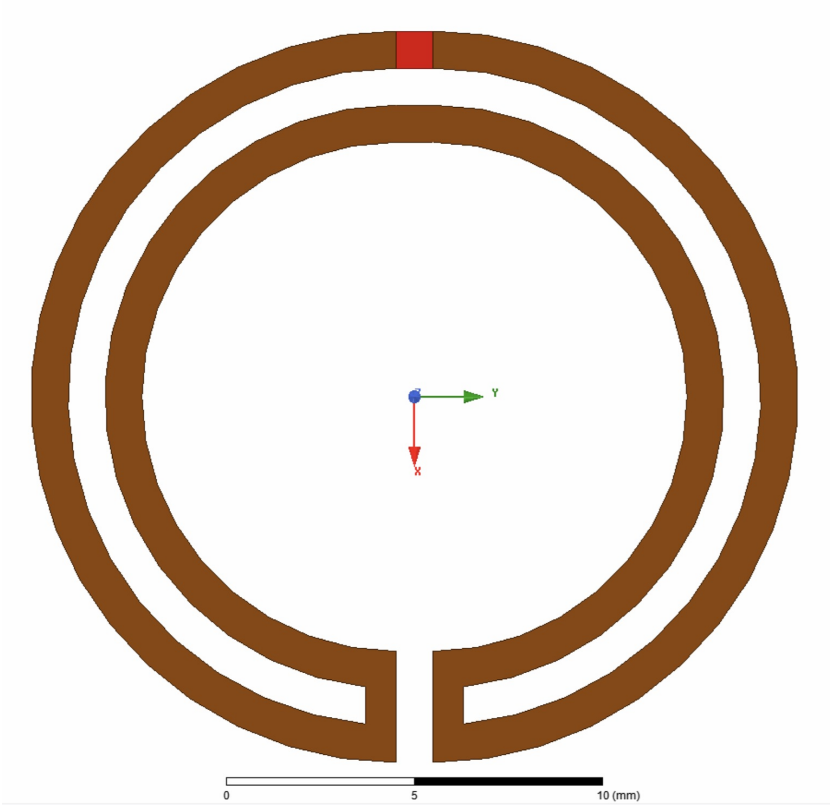

(b)

Figure 4.6: Size difference in (a) $\theta = 0$ and (b) $\theta = 180$

4.3 Bandwidth Analysis

It was decided that achieving the Fractional Bandwidth of 10.5% was the priority in making this CFDA design applicable to implement it into the hybrid RFID tag. It was previously calculated that the Fractional Bandwidth (FBW) needed for this antenna

needed to be 10.5%. To achieve this, an FBW analysis was done on several simulations to help identify trends in FBW by adjusting several antenna parameters. The antenna parameters that were analyzed were the outer ribbon width ($w2$) and the inner ribbon width ($w1$) of the CFDA, which is shown in Figure 4.1. In [27], a planar folded dipole similar to the CFDA, but without the curvature angle, was analyzed by adjusting several antenna parameters. However, it was ultimately concluded that to get wideband properties, $w2$ should increase while $w1$ decreases [27]. With this knowledge, it was decided that a parametric sweep would be done on $w1$ and $w2$ to see the effects on BW. In the CFDA HFSS design, the original design was set to 1mm for each ribbon width ($w1$ and $w2$). To see the effects on BW, an arbitrary parametric sweep from 1mm to 7 mm was simulated on the outer ribbon width ($w2$), while the inner ribbon width ($w1$) was swept at 0.5 mm and 1 mm. When simulating the CFDA antenna, two different size footprints were used. The larger footprint size of the CFDA antenna, which correlates to a size of $\lambda/2$ at 2.85 GHz at $\theta = 0$, produces a 21 mm diameter footprint at $\theta = 180$. The smaller footprint, which correlates to a size of $\lambda/4$ at 2.85 GHz at $\theta = 0$, produces a 13.5 mm diameter footprint. For clarity, this thesis will reference the footprint size by its millimeter unit size rather than its electrical size to help with size comparison. It is also important to note that the CFDA antenna size, when simulated with the parametric sweep, will be kept at the same approximate diameter even though the outer and inner ribbon width will change in surface area. In Figure 4.7, the antenna footprint is shown to be the same even compared to the larger outer ribbon width as described. Lastly, since the small (13.5 mm) and large (21 mm) designs stay the same overall diameter with their respective sizes, there is also a limitation on how large of an outer ribbon sweep can be simulated in HFSS. For example, the large footprint is only swept up to 7 mm for the outer ribbon width and the small footprint it is swept up to 3 mm. Past these values for each footprint, HFSS can not render a physical shape with those constraints.

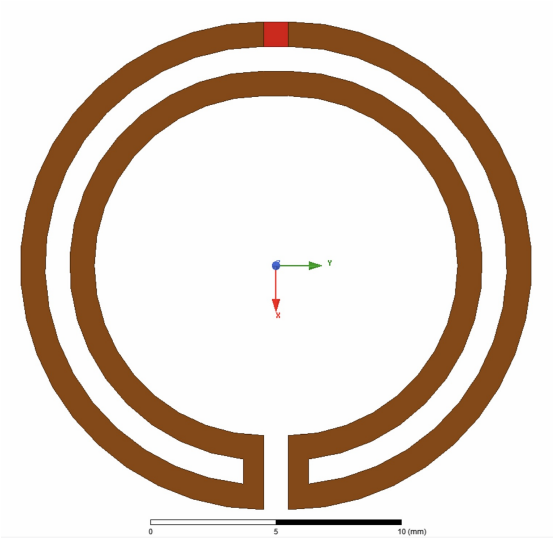

(a)

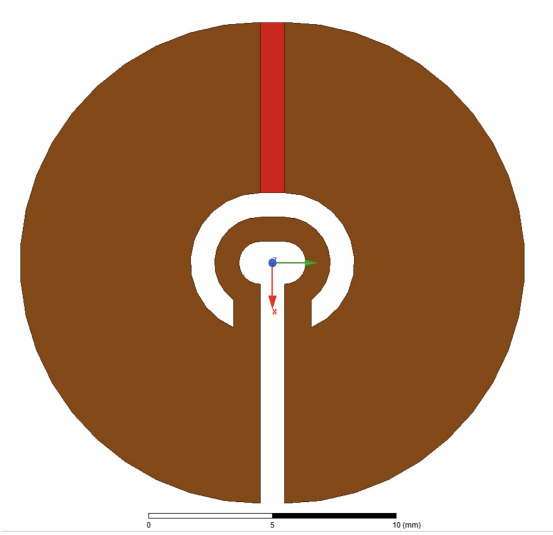

(b)

Figure 4.7: Same Footprint shown for CFDA with (a) $w2$=1 mm and (b) $w2$=7 mm

For this bandwidth analysis, FBW was calculated and found by three different methods. The first method finds FBW by plotting Voltage Standing Wave Ratio (VSWR), defining $VSWR < 2$ (as the impedance match specification), and correlating those data points to a minimum and maximum frequency points to calculate the FBW. This

method was done first to see if it was feasible to increase bandwidth to what was needed for the system. To do this, VSWR first needed to be calculated and plotted across frequency. In [20], VSWR is defined as

$$VSWR = \frac{1 + |\Gamma|}{1 - |\Gamma|} \tag{4.1}$$

where Γ is the reflection coefficient. This reflection coefficient is defined as

$$\Gamma = \frac{Z_{in} - Z_0}{Z_{in} + Z_0} \tag{4.2}$$

where Z_{in} is the input impedance of the antenna and Z_0 is the port impedance of the antenna, which is set at 50 Ω [20]. By combining these definitions, VSWR can be rewritten as

$$VSWR = \frac{1 + |\frac{Z_{in} - Z_0}{Z_{in} + Z_0}|}{1 - |\frac{Z_{in} - Z_0}{Z_{in} + Z_0}|}. \tag{4.3}$$

With Equation 4.3, VSWR can be calculated and plotted across frequency for the CFDA, which will help identify the minimum and maximum frequency points that correlate with the impedance match specification ($VSWR < 2$). Once those minimum and maximum frequency points are known, the difference between them can be utilized as the Bandwidth (BW), which will allow Equation 3.2 to calculate the Fractional Bandwidth (FBW). The results of this process is shown in Figure 4.8 and Figure 4.9 for both the small and large footprint. In more detail, Figure 4.8 shows the calculated FBW at outer ribbon widths ranging from 1 mm to 7 mm for the large footprint (21 mm in diameter) while also plotting it at various port impedance's. As it shows in Figure 4.8, there is a significant increase in FBW as the outer ribbon width ($w2$) gets close to 7 mm. It also shows that a 50 Ω is the optimal port impedance that would provide the most

FBW for the large footprint across various outer ribbon widths. In Figure 4.9, FBW was calculated for the smaller footprint (13.5 mm in diameter) at outer ribbon widths ranging from 1mm to 3mm, which was also shown across various port impedance's. Unlike the results of the larger footprint, Figure 4.9 shows that FBW is optimal at an outer ribbon width of $w2$ = 2 mm with a port impedance between 75 Ω and 100 Ω. Although these results show an increase of FBW (greater than 10.5%) at various widths, it is important to further the bandwidth analysis to confirm which antenna designs will provide enough fractional bandwidth.

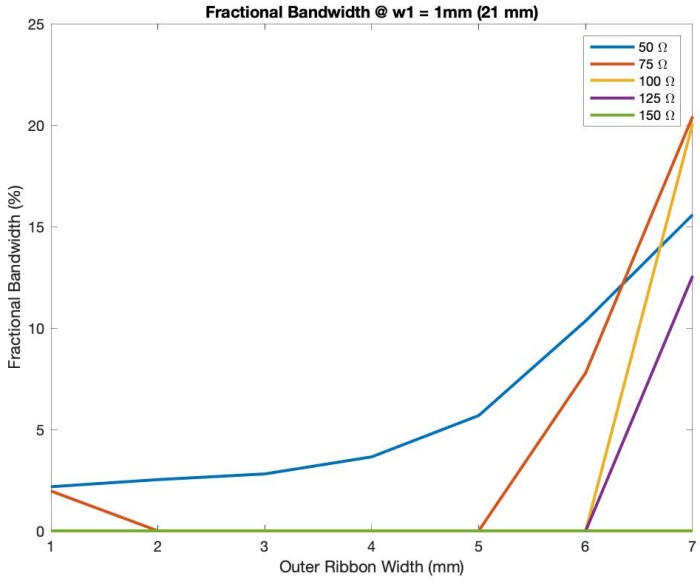

Figure 4.8: Fractional Bandwidth swept across Various outer ribbon widths for 21 mm footprint antenna

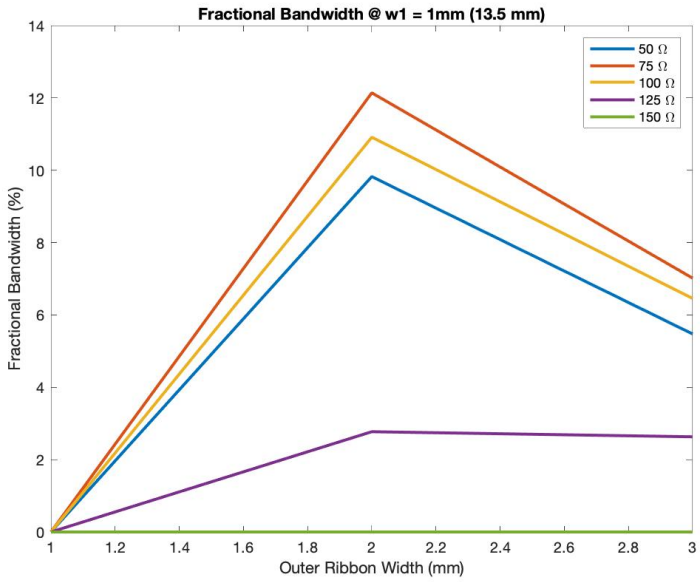

Figure 4.9: Fractional Bandwidth swept across Various outer ribbon widths for 13.5 mm footprint antenna

The second method of the FBW analysis was done by calculating the Antenna Quality Factor (Q_A) and approximately finding the FBW by taking $\frac{1}{Q_A}$. In [28], Best defines the Quality Factor of an antenna as

$$Q_A(\omega_0) = \frac{\omega_0}{2R}\sqrt{R'(\omega_0)^2 + (X'(\omega_0) + \frac{|X(\omega_0)|}{\omega_0})^2} \tag{4.4}$$

where R and X are the frequency dependant feed point resistance and reactance of the antenna, respectively, and ω_0 is the angular frequency. However, this method of calculating FBW is an approximation and was intended to show rough approximations of the FBW trends. Similar to the previous analysis, both the large and small CFDA footprints were simulated across their respected outer ribbon widths and by varying $w1$ = 0.5 mm and $w1$ = 1 mm. It is important to note that in all four figures, there is a slight difference in Q values at 2 GHz. This is because there were three different

frequency set-ups (0.5 GHz to 2 GHz, 2 GHz to 4 GHz, and 4 GHz to 6 GHz) used when simulating this CFDA in HFSS, which causes this difference in Q values. In Figure 4.11 and Figure 4.10, the Quality Factor (Q) is shown for the larger design (21 mm) at $w1$ = 0.5 mm and $w1$ = 1 mm. For both the figures, the general trend of Q starts high for lower frequencies and rapidly decreases to a steady trend at the frequencies of interests (2.7 GHz to 3 GHz). At higher frequencies greater than 3.5 GHz, the outer ribbon widths greatly affect Q. However, since the frequencies of interest are between 2.7 GHz to 3 GHz, the outer ribbon width does not have too much effect on Q.

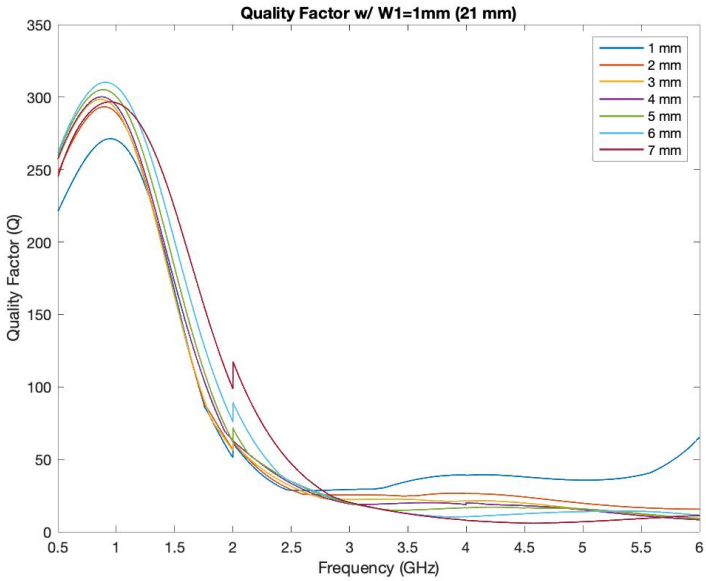

Figure 4.10: Quality Factor for 21 mm footprint antenna with $w1$ = 1 mm

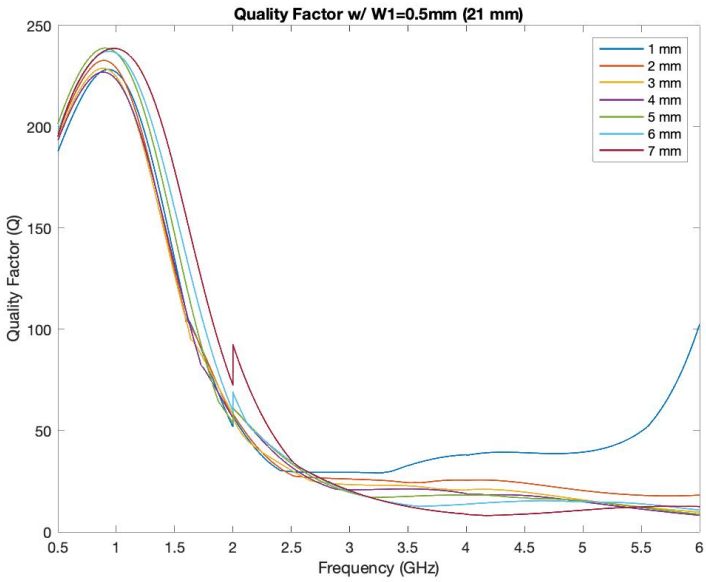

Figure 4.11: Quality Factor for 21 mm footprint antenna with $w1$ = 0.5 mm

Similarly, in Figure 4.13 and Figure 4.12 represents the Quality Factor (Q) for the smaller design (13.5 mm) at $w1$ = 0.5 mm and $w1$ = 1 mm. In these figures, the general trend of Q starts high at lower frequencies, decreases linearly between 2 GHz to 3.5 GHz, and then steadily plateaus greater than 4 GHz. Comparing both the small and large footprint, the smaller footprint has higher Q values across the frequency span, which would imply less FBW compared to the larger footprint. All four of these figures show a slight decrease in Q across the frequency span between inner ribbon widths $w1$ = 0.5 mm and $w1$ = 1 mm. Since there is a slight decrease in Q, the general trend is that the inner ribbon width of $w1$ = 0.5 mm will provide slightly more FBW across all variations of designs.

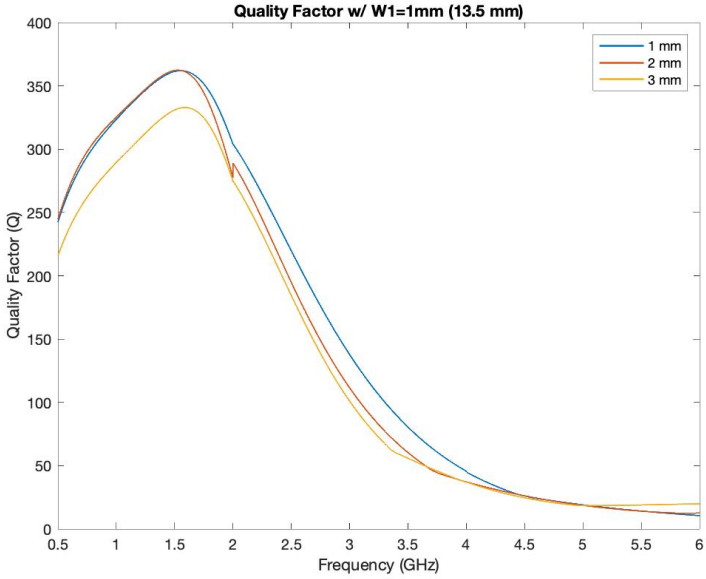

Figure 4.12: Quality Factor for 13.5 mm footprint antenna with $w1$ = 1 mm

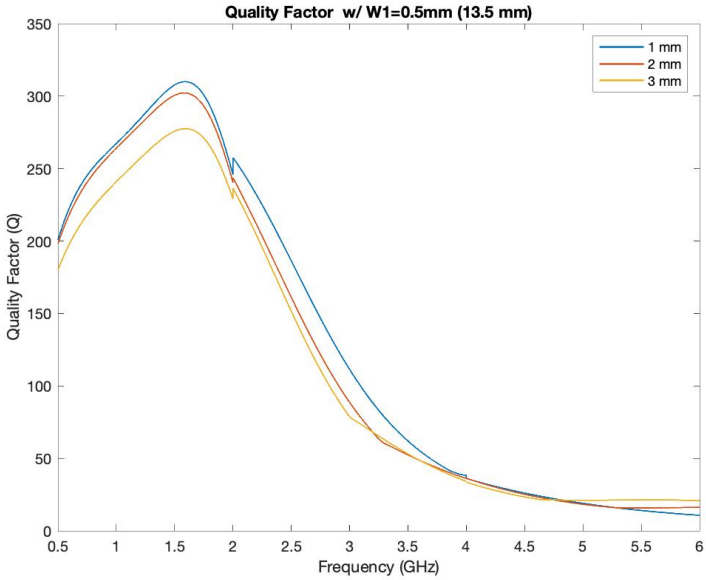

Figure 4.13: Quality Factor for 13.5 mm footprint antenna with $w1$ = 0.5 mm

The third method used to analyze bandwidth was done by plotting realized gain

across frequency. In the previous methods, the defined bandwidth was 10.5% FBW and the methods of calculating $VSWR$ and Q were used to find FBW. However, with this method, bandwidth is defined differently. In this chapter, realized gain was plotted across frequency to see what frequency points are above a certain gain threshold. This gain threshold was determined by knowing the point detection target range. In [9], it is listed that the point target detection of a 4 cm^2 target can be detected at a range of 100 km by the WSR-88d weather radar. If the target of 4 cm^2 is considered the Effective Aperture (A_e) of the target, the gain of the antenna (G_t) can be found with

$$A_e = \frac{\lambda^2 G_t}{4\pi}[18]. \tag{4.5}$$

In fact, by simply inputting the known parameters in Equation 4.5, it can be calculated that the gain of the antenna for a 4 cm^2 target at 100 kilometers should be -3.43 dB. This calculated gain can be considered the gain threshold for this bandwidth analysis as long as the CFDA has the same or larger Effective Aperture. Since the CFDA has a physical area slightly larger than 4 cm^2, it is known that the Effective Aperture of the CFDA is larger than 4 cm^2. This will allow -3.43 dB to be a minimum threshold for a target, with that effective aperture or larger, to be detected at 100 km. With that being said, by knowing the gain threshold, realized gain can be plotted across frequency to see if the desired band (2.7 to 3 GHz) is above this threshold. This effectively defines bandwidth to be $G_{Realized} > -3.43dB$ across 2.7 GHz - 3 GHz.

By knowing the redefined bandwidth requirement, the realized gain of the CFDA can be analyzed across frequency. It is important to note that only a few specific designs were plotted and were chosen based on what provided the lowest calculated Q in Figure 4.11 around the desired operating frequency (2.85 GHz). With that being said, the three chosen designs were with the CFDA having $w1$ =0.5 with $w2$ at 4 mm, 5 mm, and 6 mm.

In Figure 4.14, the realized gain for these three designs was plotted across frequency with a dashed line at -3.43 dB indicating the gain threshold needed. In this figure, it is shown that the best overall design that has a greater dB value than -3.43 dB, across the frequency span of 2.7 GHz - 3 GHz, is where $w2$ = 4 mm while $w1$ =0.5 for the 21 mm antenna footprint. With this being known, this particular design can also be plotted across port impedance to see how it affects its performance in terms of realized gain. In Figure 4.15, this design is plotted across various port impedance's ranging from 50 ohms up to 150 ohms. The overall results in this figure show that it lessens the magnitude of the realized gain but appears to broaden the number of frequency points above the -3.43 dB threshold.

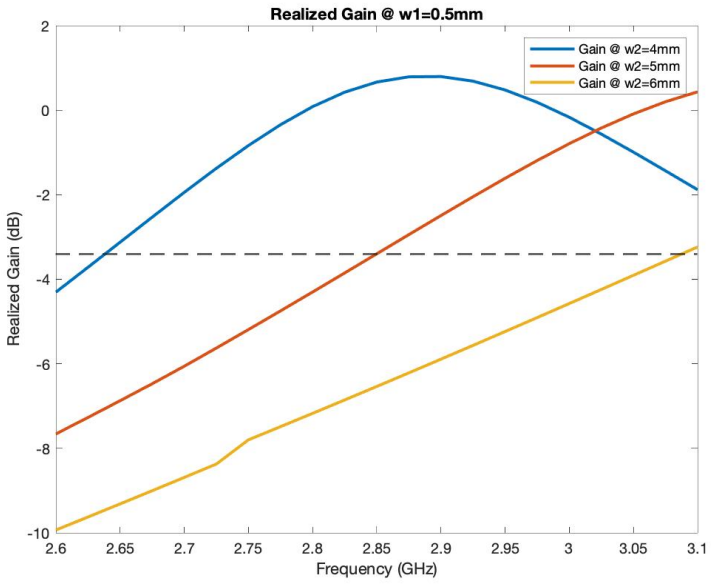

Figure 4.14: Realized Gain across frequency for 21 mm footprint CFDA with various $w2$ widths

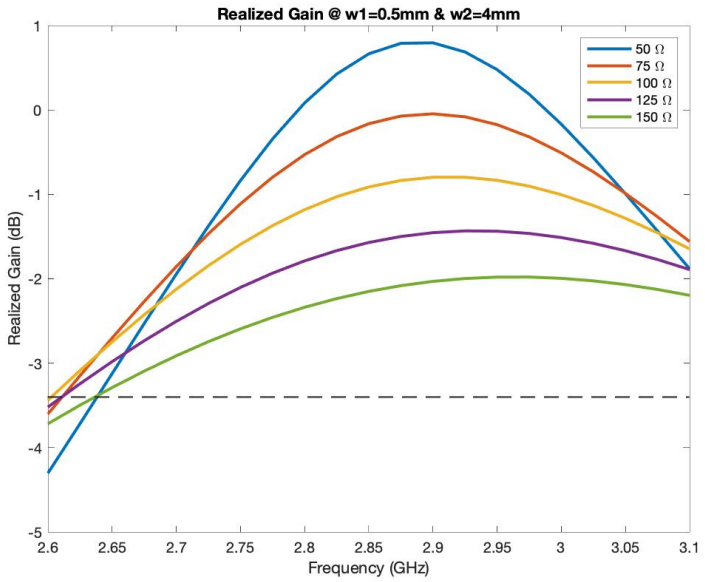

Figure 4.15: Realized Gain across frequency for 21 mm footprint CFDA with $w2$= 4mm and $w1$ = 0.5 mm

4.4 Conclusion

In conclusion, the Curved Folded Dipole Antenna (CFDA) was introduced and discussed the curved angle analysis that was done by Taylor Poydence in [26]. The CFDA was justified as a great baseline to start with due to its compact size due to its curvature and its quasi-isotropic radiation pattern shown in Figure 4.5. The CFDA was analyzed by varying the widths of the inner ($w1$) and outer ($w2$) ribbon widths and showing the general trends in bandwidth for a 21 mm and a 13.5 mm antenna footprint. These general trends in bandwidth were analyzed by first defining bandwidth as $VSWR < 2$ to see if the frequency span of 2.7 GHz to 3 GHz satisfied the bandwidth definition. These results were plotted in terms of Fractional Bandwidth across various widths, in Figure 4.8 and Figure 4.9, and shows that the general trend of bandwidth increases with width

increase. In another method of bandwidth analysis, bandwidth trends were analyzed by plotting the antenna Quality Factor. In comparison between Figure 4.10 and 4.11 for the larger antenna footprint and between Figure 4.12 and 4.13 for the smaller antenna footprint, it was shown that the general trend in quality factor decreases in magnitude when the inner ribbon width ($w1$) also decreases; this would mean that as quality factor decreases, bandwidth would increase for smaller inner ribbon widths ($w1$). These trend analyses allowed for a better understanding that a smaller inner ribbon width with a larger outer ribbon width is needed to get more bandwidth. With that being said, the last method in the bandwidth analysis, with specific widths for both the inner and outer ribbon width, involved calculating a gain threshold needed to be seen by the WSR-88d weather radar from a certain distance. In the technical information of the WSR-88d's website, in [9], it is listed that a 4 cm^2 point target can be seen at 100 kilometers. By using the 4 cm^2 as the effective aperture, a minimum gain threshold of -3.43 dB was calculated to be seen at 100 kilometers by the WSR-88d weather radar. By having this gain threshold, realized gain of the CFDA was plotted across frequency in Figure 4.14 and was shown that the frequency span of interest (2.7 GHz to 3 GHz) met and exceeded the minimum gain threshold at $w1$ = 0.5 mm and $w2$ = 4 mm. This analysis in bandwidth trend gave a better understanding of what specific inner and outer ribbon width provided more bandwidth. In the next chapter, a bird model will be designed and verified to see how a bird would affect the parameters of the CFDA.

Chapter 5

Designing and Verifying Bird Model

5.1 Introduction

To advance knowledge about Bird measurements and modeling birds, this chapter will go into detail on what was done to make a simple Bird Model. This Bird Model will allow for a more accurate representation of salvaged Bird carcasses compared to what was previously used in past for bird measurements. Salvaged carcasses of Dark-eyed Junco (*Junco Hyemalis*) will be used to do measurements and those results will be used to find a permittivity and conductivity value that will best represent the Birds.

5.2 Designing Bird Model

By knowing a few optimal CFDA designs, it was decided that a bird model needed to be created to see how a bird's body would affect the CFDA electromagnetically. This is important to do because the CFDA will eventually be implemented as a tag that will be attached to a bird's body for tracking purposes. By creating an accurate bird model, it will provide more insight into how the CFDA will be affected by the bird's size and shape. This bird model would be created in HFSS and then verified on whether or not the bird model is accurate through measurements. The first step of

this process is to create a bird model in HFSS that could serve as a basis for initial simulations. This could be challenging since the biological body of a bird is made up of different materials (tissues, blood, organs, etc ...) that could range in permittivities and conductivities values. This process of defining permittivities and conductivities of a bird's biological material could become excessively complicated, especially since there no known values for bird biological material yet. However, in [29], a simple bird model was created to see how a bird would affect the efficiency and impedance of the monopole antenna using for tracking birds. This simple bird model was shaped like an ellipsoid and was approximated by using the average permittivity and conductivity values of biological human materials (such as muscle, brain, and fat) at the desired frequency. This simple bird model is shown in Figure 5.1. As for their measurements, a sponge was carved out of the shape of a bird and was injected with biological saline to represent the body of a bird [29]. Similar to [29], a simple bird model, in a shape of an ellipsoid, was desired to serve as a basis in HFSS.

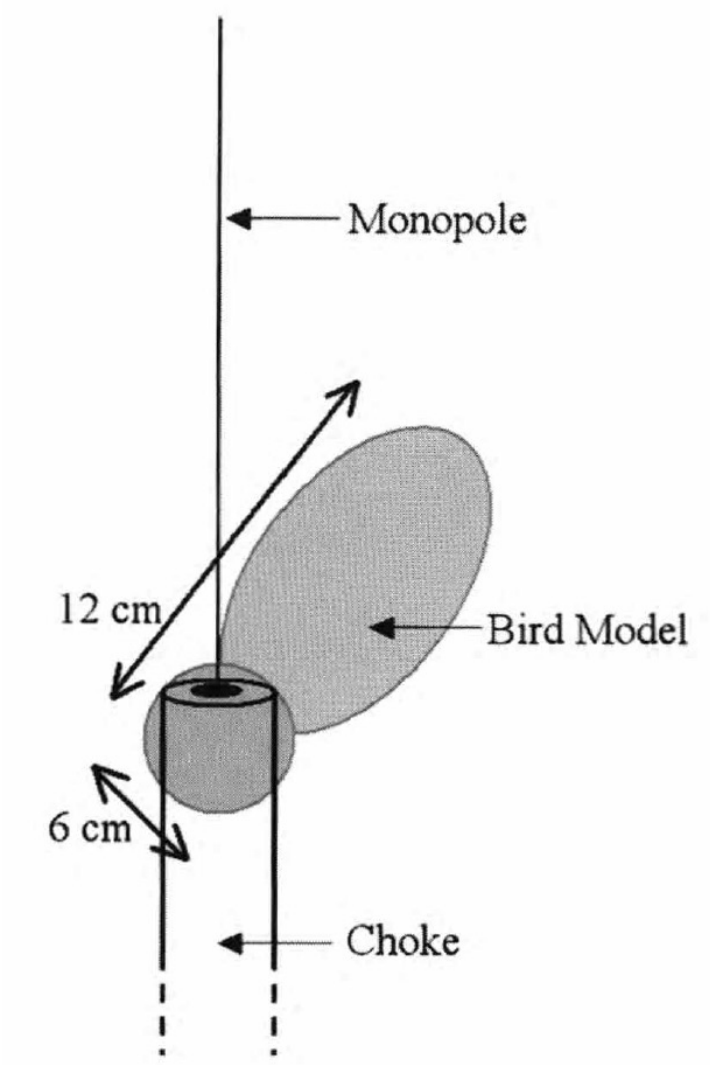

Figure 5.1: Simple Bird Model from [29]

In addition to the shape of the bird model, a consensus was made to add slightly more detail to the bird model. More specifically, it was decided that parts of the respiratory system of the bird would be added to the bird model to be slightly more accurate. In a bird's anatomy, the main organs of the respiratory system include a pair of lungs and several air-sacs that surround the lungs, which can be shown in Figure 5.2. Unlike the human anatomy, a bird's lung does not collapse. The air-sacs are the organs that

compress and expand, which allows air to be circulated through the lungs [30].

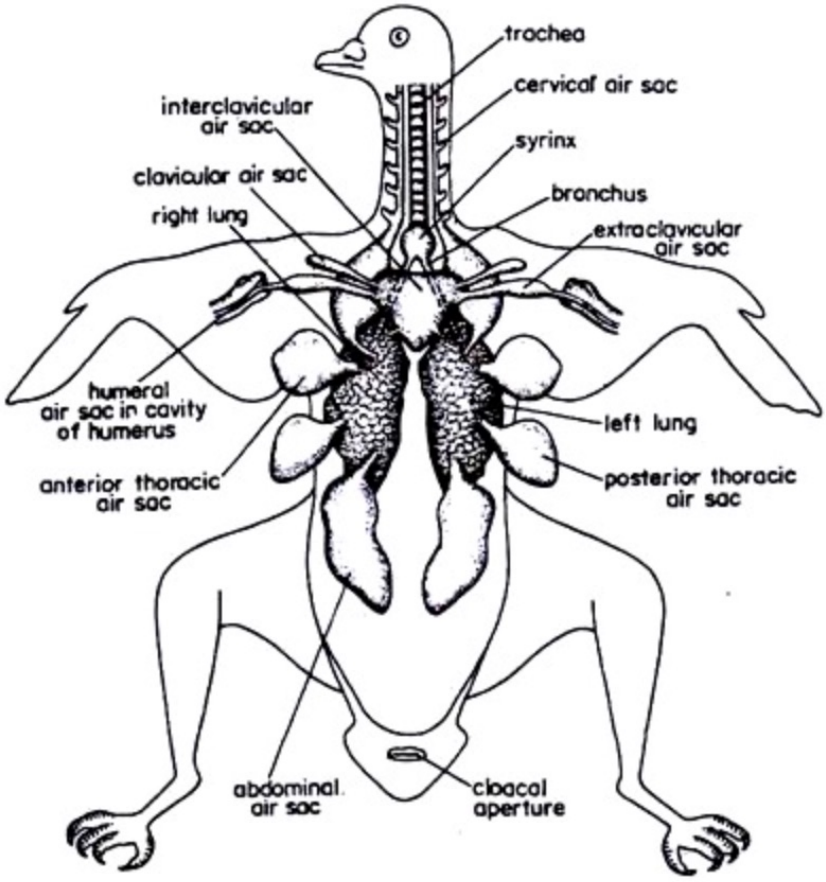

Figure 5.2: Diagram of Pigeon's Air-sacs from [30]

By knowing this, there will be two bird models made, one with inflated air-sacs and one with deflated air-sacs, which will allow us to see the effects it will have on an antenna if any at all. The original bird model designed in Solidworks was approximated to be the size of a penguin. However, as a preferred classification of birds, it was scaled down to represent a Dark-eyed Junco (*Junco Hyemalis*). Dark-eyed Juncos (*Junco Hyemalis*), shown in Figure 5.3, are typically 20-25 grams in weight and have a body length (from head to the end of tail) of 5.5 inches.



Figure 5.3: Dark-Eyed Junco from [31]

With this relatively small size and weight, it makes Dark-eyed juncos great to model after. In Figure 5.4 and Figure 5.5, the bird models are shown with the inflated and deflated air-sacs, respectively, and have approximately the same size as the Dark-eyed Junco. The overall length and width of Bird models are 70 mm and 35 mm, respectively. Figure 5.4 indicates where the head and the tail of the bird would be to understand its orientation. It is important to note that the air-sacs and lungs shown in Figure 5.4 and Figure 5.5 were approximated to be a certain size concerning the body. This is a visual approximation of the size of the lungs and air sacs. To get a more accurate depiction of the size of the lungs and air-sacs, a bird would have to be dissected to be further analyzed and measured. For purposes of labeling, the HFSS bird model with the inflated air-sacs, shown in Figure 5.4, will be used as a basis for the Bird model and will later show the difference between the inflated and deflated bird model.

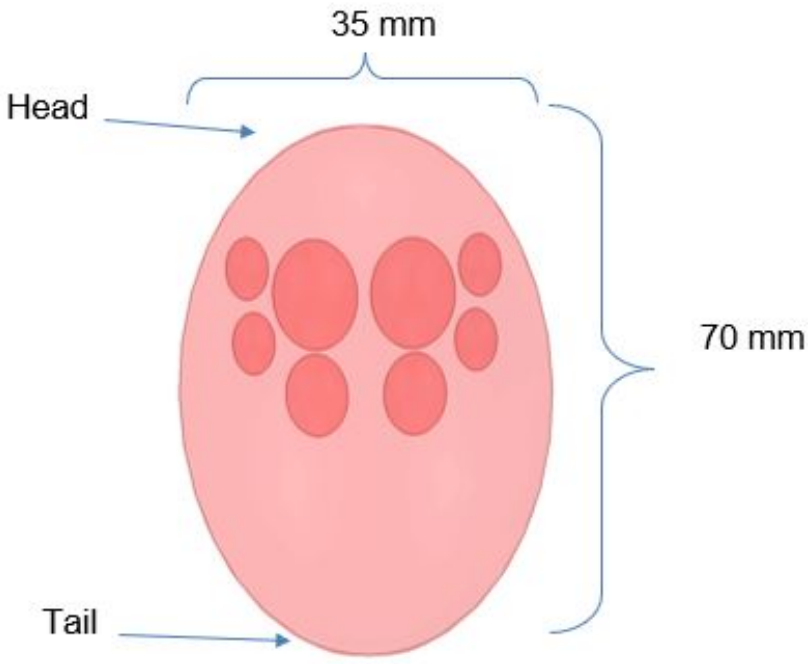

Figure 5.4: Bird Model with Inflated Air-sacs

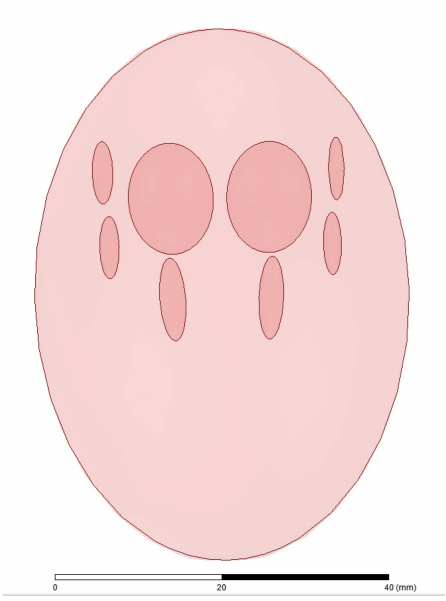

Figure 5.5: Bird Model with Deflated Air-sacs

5.3 Verifying Bird Model

To attempt to create a bird model in HFSS, the first step is to understand that the bird model designed, shown in Figure 5.4, will be used as a homogeneous media model. This means that a single value of dielectric permittivity (ϵ_r) and conductivity (σ) value will represent the bird model in HFSS. These values of ϵ_r and σ for bird biological material are not known in current academia. In [29], a bird model was created for measurements composed of a sponge filled with Saline. To be a little bit more accurate, the ϵ_r and σ values will need to know and verified with actual bird measurements (using Dark-eyed Juncos) for comparison. This was done by first taking measurements with birds with a simple reference antenna.

A Ribbon Monopole Antenna was decided to be a great simple antenna to fabricate and measure for reference. Since the antenna is only composed of a ground plane and a ribbon monopole, it is easy to simulate and fabricate. This ribbon monopole antenna was designed at the operating frequency of 2.85 GHz and was simulated in HFSS. In Figure 5.6, the ribbon monopole designed in HFSS is shown. The ribbon itself (the radiator) was simulated as a 1/2 oz copper trace material backed with Rogers 5880 substrate with a thickness of 30 mils. The length of the radiator was tuned to resonant at 2.85 GHz, which is slightly smaller than a quarter wavelength to accommodate for fringing. The ground plane was designed to be a square with a length of each side being twice the wavelength (approximately 21.43 cm) and used 1/2 oz copper Rogers 4350 material with a thickness of 60 mils. Also, to make the simulation more accurate, the 50-ohm coax connector was incorporated in the simulation design.

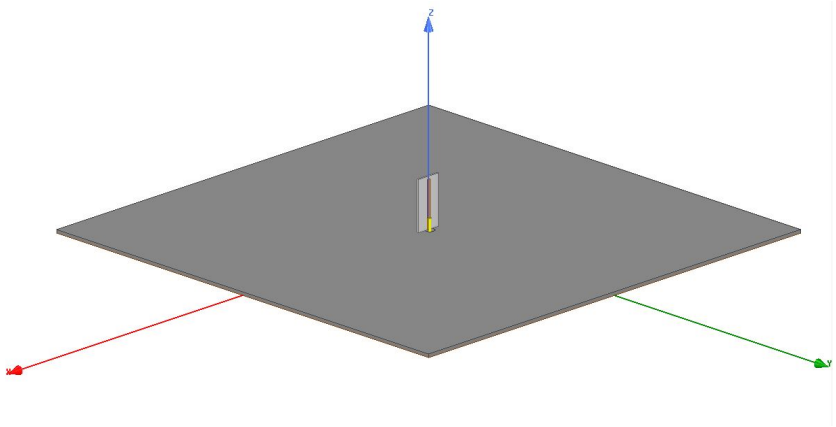

Figure 5.6: Dimetric View of the Simulated Ribbon Monopole with an operating frequency of 2.85 GHz

Once this was simulated, the monopole antenna was fabricated and measured for comparison. This ribbon monopole was fabricated via the photo-lithography process. In Figure 5.7, a before and after picture is shown of how the Rogers 5880 substrate and an inverted mask are used to create a batch of ribbon monopole. In Figure 5.8, a picture of the fabricated ribbon monopole is shown after the 50-ohm coax connector was soldered onto the Ribbon trace and the ground plane. The white substrate is the Rogers 4350 substrate material

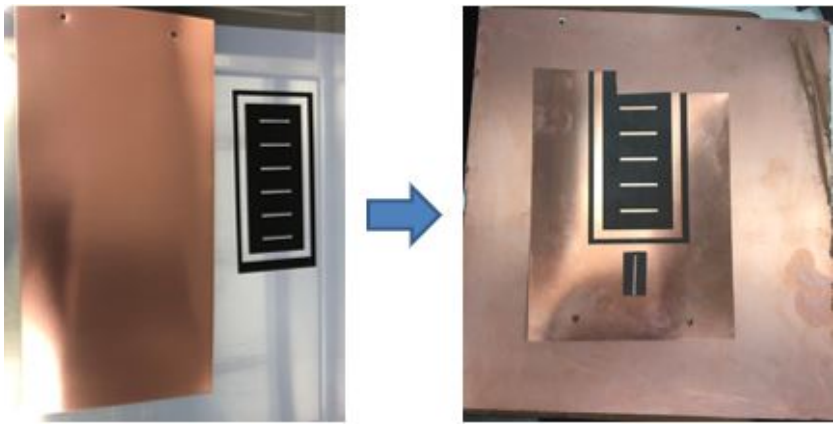

Figure 5.7: Before and After image of the Rogers 5880 substrate with inverted Mask fabricated via Photo-lithography process



(a) (b)

Figure 5.8: Fabricated Ribbon Monopole with an operating frequency of 2.85 GHz (a) Top view of Ribbon monopole (b) Bottom view of ground plane with soldered coax connector

Once the ribbon monopole was fabricated, a Network Analyzer was used to measure the insertion loss (S_{11}) and the input impedance (Z_{11}) to compare it to the simulated results. Comparing the measured and simulated results, it will allow for a more ac-

curate comparison when measuring the ribbon monopole with and without the actual birds attached to it. In Figure 5.9, the magnitude of the insertion loss ($|S_{11}|$) is shown for both the measured and simulated monopole antenna. It is shown that the measured and simulated monopole antenna has a great agreement with $|S_{11}|$ and matches each other fairly well. In Figure 5.10, the input impedance (Z_{11}) is shown for the measured and simulated monopole antenna and it appears to match fairly well between them. The resonance is at 2.85 GHz for both the simulated and measured input impedance. There is a slight discrepancy between the simulated and the measured monopole imaginary impedance past 3.2 GHz. This is most likely due to the fabrication tolerances of designing this monopole antenna in-house. For instance, the ground plane is about 0.5 mm within the desired size considering it was cut using a paper cutter and measured with a ruler. With that being said, due to the simplified method in fabricating the monopole antenna, there are slight differences in the measured results compared to the simulated results. However, it is accurate enough for this application especially since it is aligned very well between 2.7 GHz to 3 GHz.

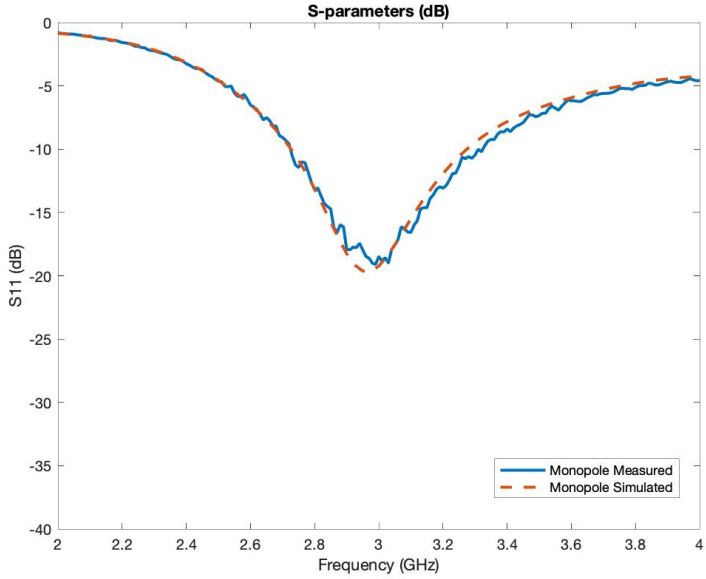

Figure 5.9: Magnitude of Insertion Loss ($|S_{11}|$) in dB plotted across frequency

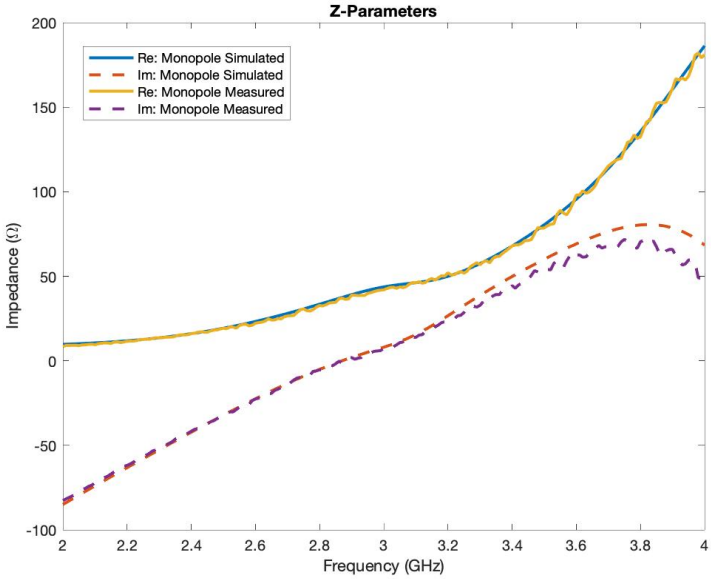

Figure 5.10: Input impedance (Z_{11}) plotted across frequency

Far-field radiation pattern measurements were done to also compare to the simu-

lated ribbon monopole. The far-field measurements were done in an anechoic chamber for accuracy. To accurately compare the simulated radiation patterns to the measured radiation patterns, three radiation pattern cut planes were chosen for comparison. The first was the Azimuth cut plane, which is important since an omnidirectional radiation pattern is desired in the azimuth plane for the antenna that goes on the bird. When measuring the fabricated ribbon monopole antenna, a simple cardboard box was used to sit the antenna on while it was measured in the anechoic chamber, which can be seen in Figure 5.11. The Co-polarized azimuth radiation pattern (Gain) for the measured and the simulated monopole antenna can be seen in Figure 5.12. Based on that figure, it is clear that the azimuth far-field radiation pattern of the measured monopole did align well with the simulated radiation pattern. One thing to note on the radiation patterns is the slight dip in the radiation pattern between 270 and 240 markers on the polar plot for Figure 5.12. This dip is common for all of the measured radiation patterns and is caused by the placement of the coax cable used for measurements that can be seen on the right side in Figure 5.11.

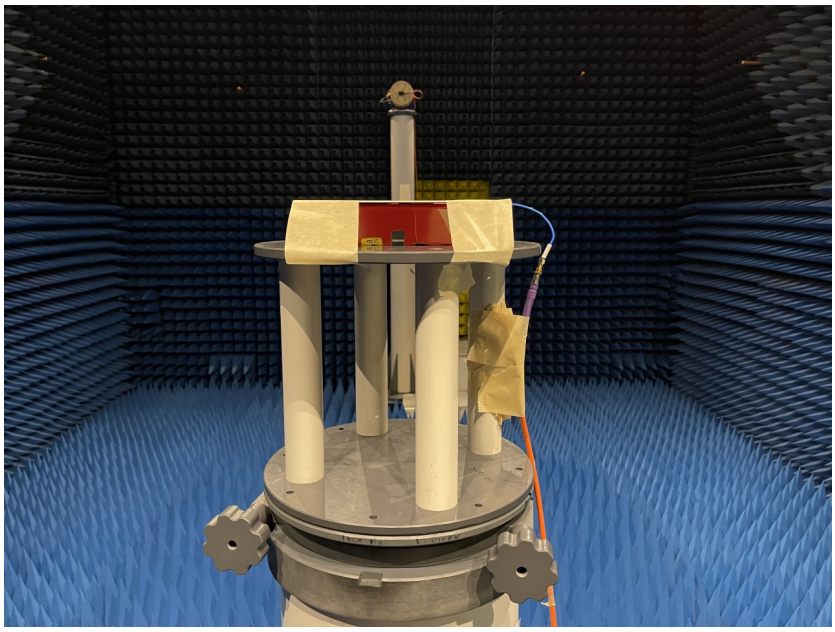

Figure 5.11: Azimuth far-field radiation measurement set-up in anechoic chamber

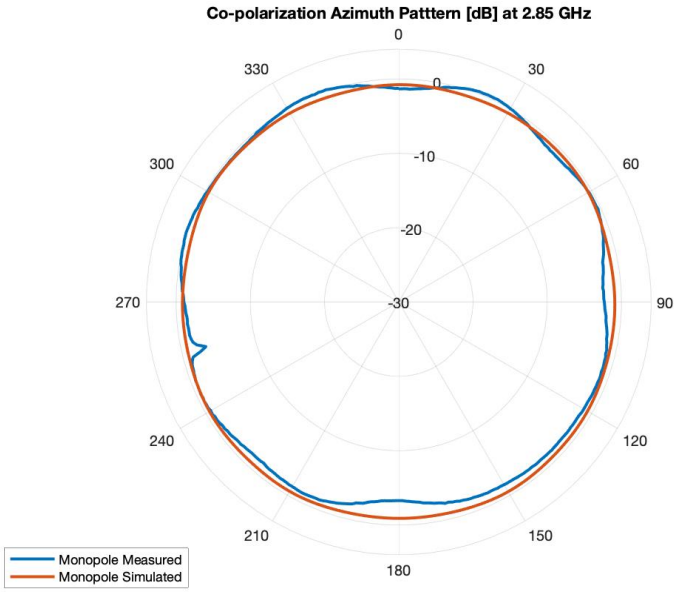

Figure 5.12: Co-polarized Azimuth far-field radiation pattern measurement compared to simulated radiation pattern

Similarly, two elevation radiation cut planes were also measured at $\Phi = 0$ and $\Phi = 90$ for the simulated and measured ribbon monopole antenna. In Figure 5.13, the set-up used to measure the far-field elevation radiation patterns in the anechoic chamber at $\Phi = 0$ and $\Phi = 90$ are shown. In this figure, a grey 3D printed slot mount is shown and was used to hold the monopole by the ground plane for far-field measurements. In Figure 5.14, the measured Co-polarized elevation radiation pattern at $\Phi = 0$ is shown in comparison to the simulated results. This figure shows that the measured results of the ribbon monopole do match well with the simulated results with the slight differences in the nulls. In Figure 5.15, measured Co-polarized elevation radiation pattern at $\Phi = 90$ is shown in comparison to the simulated results. The radiation pattern between the measured and simulated monopole does align well except for the slight shift in the null. For this application, the measured elevation radiation patterns in both Figure 5.14 and Figure 5.15 are considered accurate enough to be used for measurements and simulation comparison.

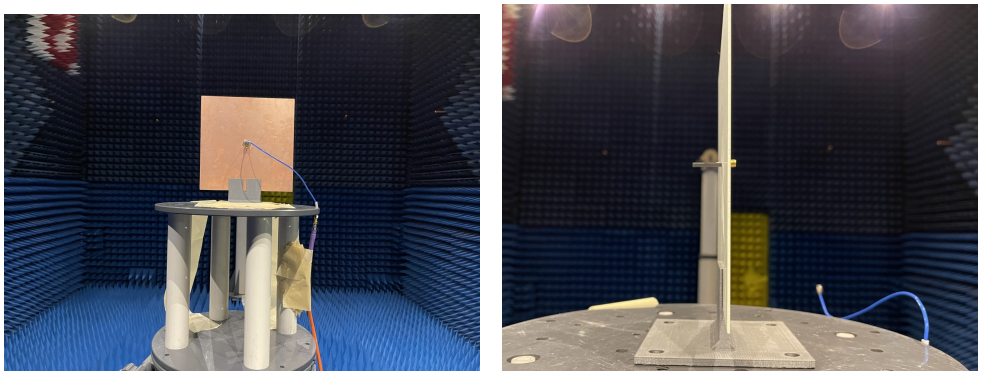

(a) (b)

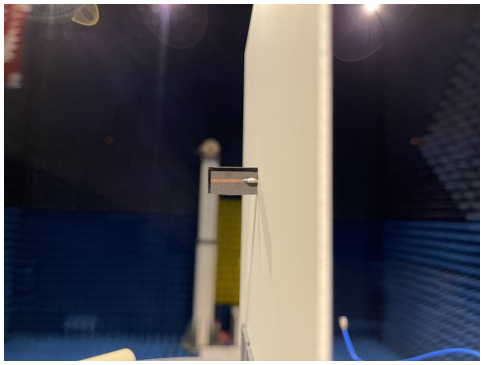

(c)

Figure 5.13: Elevation far-field radiation pattern set-up in anechoic chamber (a) Elevation set-up with 3D mount (b) Side-view of Monopole orientated for $\Phi = 0$ (c) Side-view of Monopole orientated for $\Phi = 90$

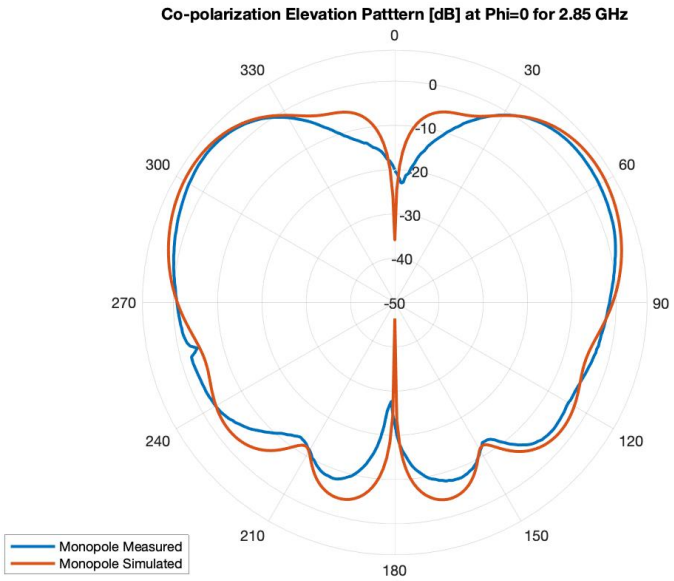

Figure 5.14: Co-polarized Elevation far-field radiation pattern measurement compared to simulated radiation pattern at $\Phi = 0$

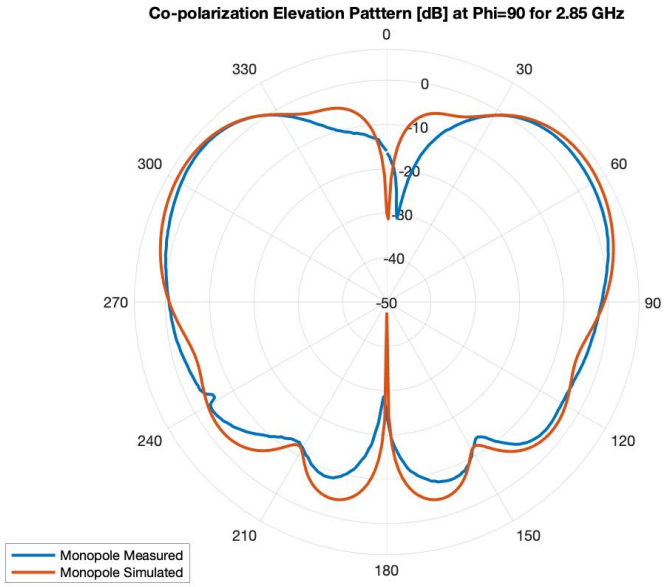

Figure 5.15: Co-polarized Elevation far-field radiation pattern measurement compared to simulated radiation pattern at $\Phi = 90$

With the fabricated monopole accurately modeled to what was simulated, the monopole antenna was then measured with actual birds to analyze the impact the birds would have. The Dark-eyed Juncos (*Junco Hyemalis*) used for measurements are salvaged carcasses and were kept frozen for preservation. It is important to note that the Birds (salvaged carcasses) were thawed before any measurement was taken. The first challenge in measuring the birds with the monopole antenna was figuring out how to mount the bird in a particular position. A typical tag mounted on a bird is usually placed on the lower back on the back using a leg-loop harness just like it is shown in Figure 5.16.

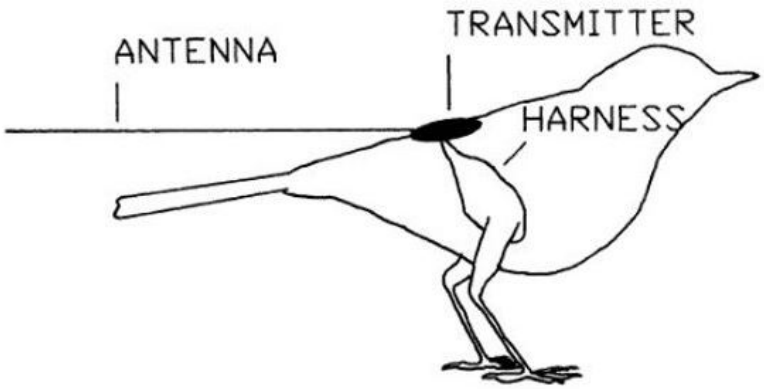

Figure 5.16: Illustration of a leg-loop harness for bird trackers from [32]

To position the bird where the ribbon monopole is position on the lower back, a styrofoam base with a cut-out to insert the bird was used. This styrofoam mount was used to position the lower back of the bird right up against the ribbon monopole. To have the lower back of the bird model right up against the ribbon monopole in HFSS, the bird model was angled enough and was positioned against the ribbon monopole. The ribbon monopole was positioned to have the ribbon copper trace to face outward and away from the bird model. The ground plane of the monopole antenna is larger than the bird model. This makes it difficult to be able to accurately position the bird

model in HFSS, but it is convenient enough to use it as a platform to place the styrofoam mount on to hold the bird in position. In Figure 5.17, the simulated ribbon monopole antenna is shown with the bird model positioned like previously mentioned (antenna close to the lower back). This figure shows a dimetric view of the bird model with respect to the monopole and a side view of the bird model to show it is angled. This is an accurate representation of how the carcasses of the birds were placed with respect to the monopole antenna during the measurements.

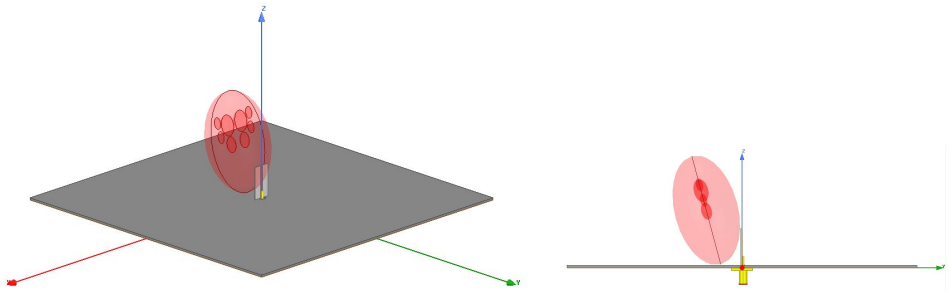

(a) (b)

Figure 5.17: Simulated ribbon monopole with Bird Model GHz (a) Dimetric view of Bird model with monopole (b) Side view of Bird Model with monopole

Similarly, like the fabricated monopole was compared to the simulated, it is desired to compare measurements of the fabricated monopole with and without birds attached. This is particularly useful to show how the carcasses of the birds would impact the antenna's impedance, insertion loss, and far-field measurements. Once it is known how the bird impacts the antenna through measurements, this can be used as a reference and try to simulate various permittivity and conductivity values for the bird model in HFSS to accurately represent a Dark-eyed Junco (*Junco Hyemalis*). It is important to note that two different Dark-eyed Juncos (*Junco Hyemalis*), used for the bird measurements, are labeled as Bird 1 and Bird 2 for comparison. Bird 1 had been dead and frozen for about a year and a half while Bird 2 had a more recent death of about 2 weeks prior to

measurements being taken. In physical appearance, Bird 1 is slightly bigger (about 10 to 15 mm in additional length) than Bird 2.

In Figure 5.18, the magnitude of the insertion loss ($|S_{11}|$) plotted for Bird 1, Bird 2, the previously shown simulated and fabricated monopole. This figure shows that Bird 1 and Bird 2 slightly shifted the resonance and in the case of Bird 2 provided a higher insertion loss dip. In Figure 5.19, the input impedance (Z_{11}) is shown for both Bird 1 and Bird 2 compared to the measured monopole antenna. Similarly to the previous figure, it shows that the birds provide a slight shift in impedance, with a greater difference being towards the higher frequencies. Both of these figures illustrate that birds did not have too much of an impact on the ribbon monopole. The slight shift of resonance and impedance is manageable for this application.

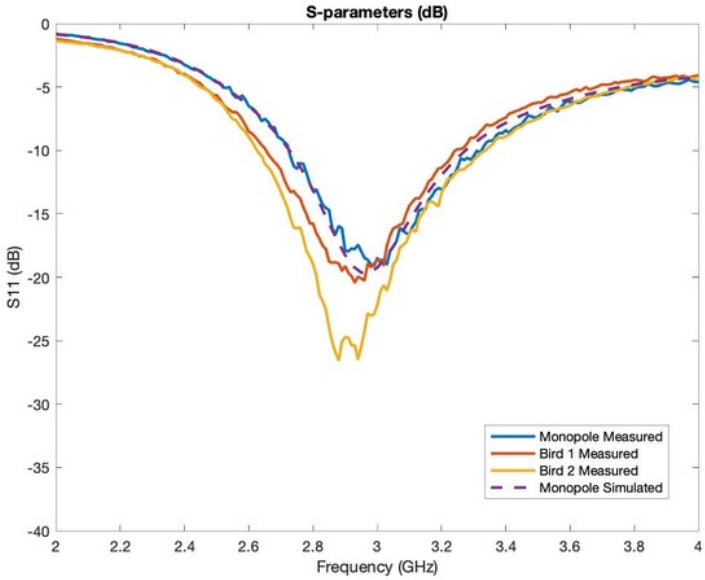

Figure 5.18: Magnitude of Insertion Loss ($|S_{11}|$) in dB plotted across frequency for bird measurements compared to monopole

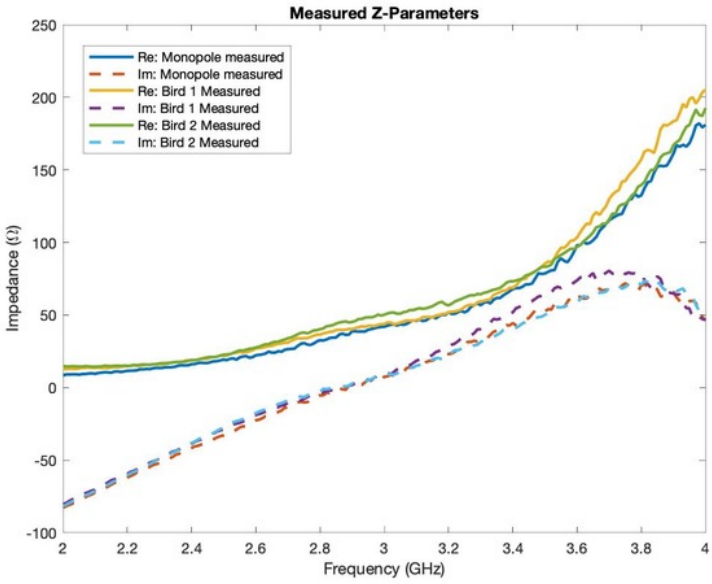

Figure 5.19: Input impedance (Z_{11}) plotted across frequency for bird measurements compared to monopole

In addition, far-field radiation pattern measurements were also taken for comparison. In Figure 5.20, the Co-polarized Azimuth radiation pattern is shown for Bird 1, bird 2, and the measured monopole antenna. In this figure, it is very noticeable that the birds do have much more of an effect on the ribbon monopole antenna. For both birds, there is a dip in Gain (dB) around markers 90 and 270, which is up to a 12 dB difference compared to the monopole antenna. The radiation dip around marker 270 also includes the dip from the coax cable that was explained in the set-up earlier in this chapter. This dip in radiation pattern shows that the bird's body is more complex than expected.

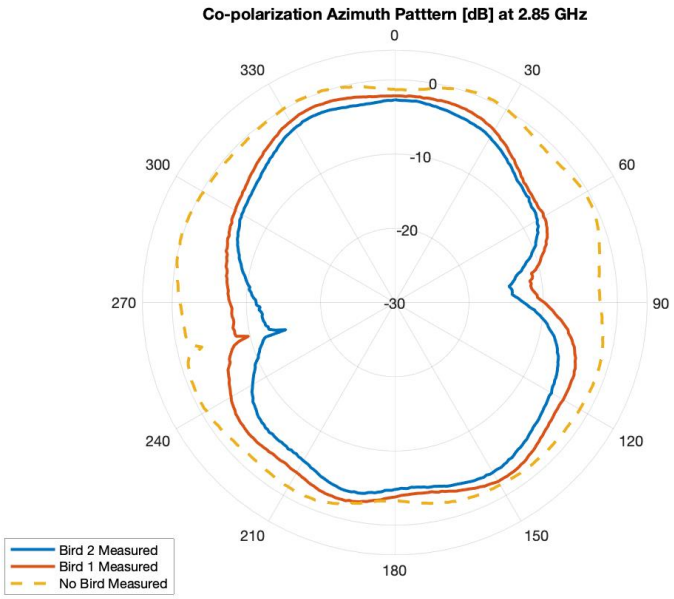

Figure 5.20: Co-polarized Azimuth far-field radiation pattern with and without birds

In Figure 5.21, the Co-polarized Elevation radiation pattern at $\Phi = 0$ is shown for Bird 1, Bird 2, and the monopole antenna. In this figure, it appears that the birds do impact the radiation pattern slightly. Bird 1 appears to match well with the monopole antenna while Bird 2 appears to have a greater difference in Gain compared to the monopole antenna. In Figure 5.22, the Co-polarized Elevation radiation pattern at $\Phi = 90$ is shown for Bird 1, Bird 2, and the monopole antenna. This figure shows that the birds do not differ from the monopole for the majority of the radiation pattern. However, one big noticeable difference is that there is no longer a null at the top of the radiation pattern when the birds are attached.

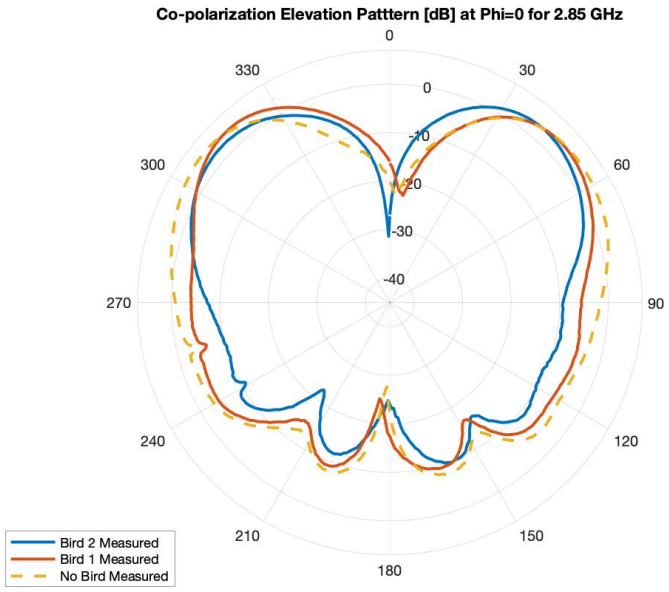

Figure 5.21: Co-polarized Elevation far-field radiation pattern with and without birds at $\Phi = 0$

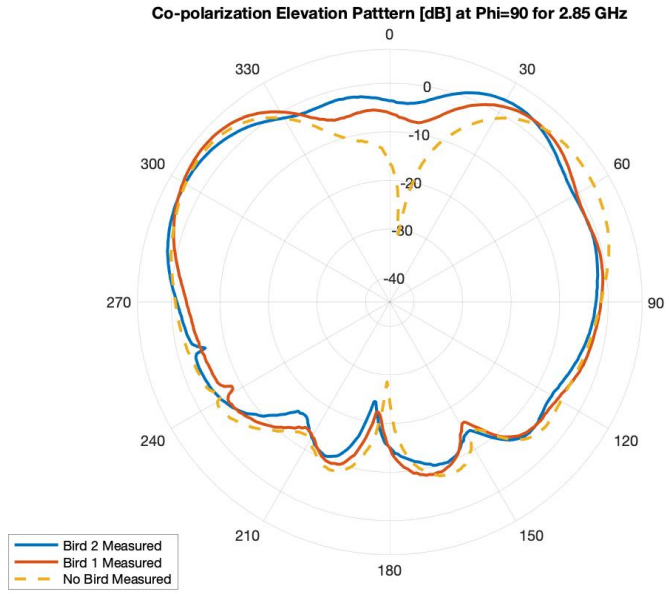

Figure 5.22: Co-polarized Elevation far-field radiation pattern with and without birds at $\Phi = 90$

Now that there are measured results with the Dark-eyed Juncos (*Junco Hyemalis*), permittivity and conductivity values can be found to attempt to match the measured results. This was done by running several larger parametric sweeps in HFSS to find values that match closely with the measured. For the parametric sweeps, the permittivity values ranged from 1 to 60 with a step size of 1 and the conductivity values were preset to 0.001, 0.01, 0.1, 1, and 10 $[S/m]$. With this large parametric sweep, the input impedance was analyzed at various combinations and was compared to the measured results. With this analysis, a trend appears that lower permittivity and conductivity values were needed to match the measured results. With this knowledge, another parametric sweep was done for smaller values of permittivity ranging from 1 to 5 (with a step size of 0.05) and conductivity values ranging from 0.001 to 0.1 S/m (with a step size of 0.001). In the end, out of all the parametric sweeps done in HFSS, a conclusion was made that a permittivity (ϵ_r) value of 1.2 and a conductivity (σ) value of 0.004 $[S/m]$ were chosen to be a more accurate representation of the Dark-eyed Juncos (*Junco Hyemalis*).

It is important to note that there were two previously bird models designed; one bird model included inflated air-sacs while the other had deflated air-sacs. By using $\epsilon_r = 1.2$ and $\sigma = 0.004[S/m]$, a direct comparison can be shown to see the difference inflated or deflated air-sacs. In Figure 5.23 and Figure 5.24, the magnitude insertion loss ($|S_{11}|$) and the input impedance (Z_{11}) are shown, respectfully, for the bird models with inflated and deflated air-sacs. In these figures, it is clearly shown that there is no difference between the two bird models.

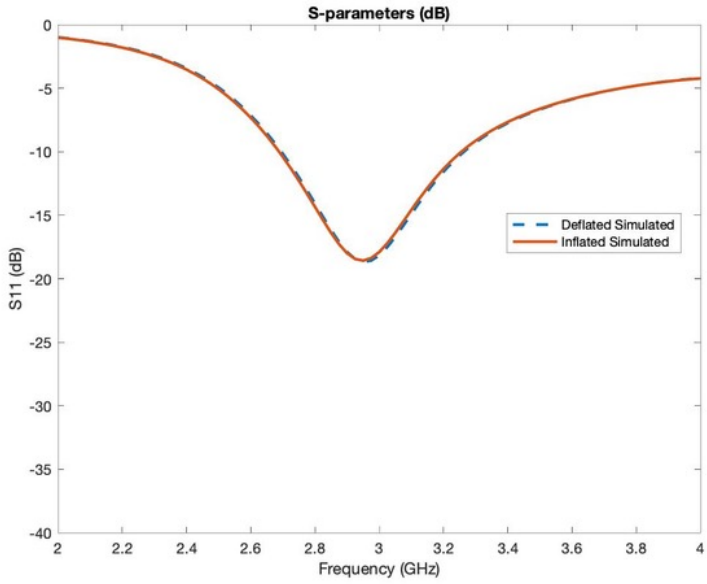

Figure 5.23: Magnitude of Insertion Loss ($|S_{11}|$) in dB plotted across frequency for Inflated Bird Model vs Deflated Bird Model

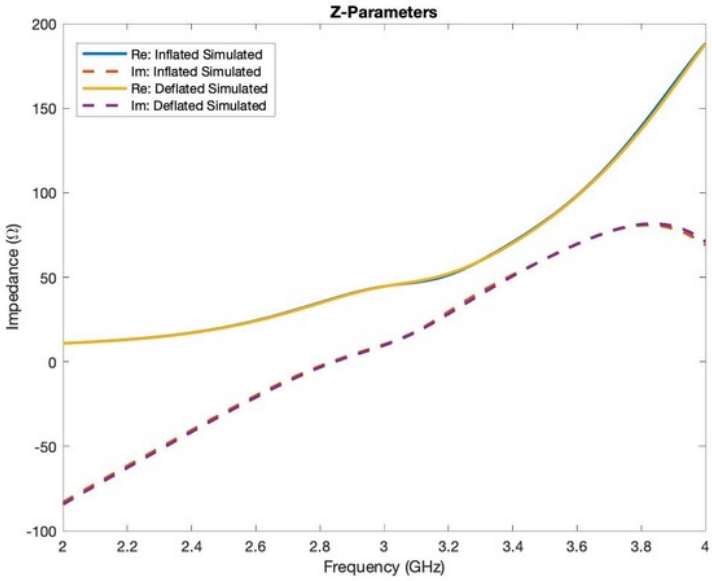

Figure 5.24: Input impedance (Z_{11}) plotted across frequency for Inflated Bird Model vs Deflated Bird Model

Additionally, this can also be seen for the Co-polarized far-field radiation patterns for both Azimuth (shown in Figure 5.25) and the Elevation at $\Phi = 0$ and $\Phi = 90$ (shown in Figure 5.26 and Figure 5.27, respectfully. With there being no difference between the inflated and deflated bird models, it is inferred that the amount of air in the air-sacs minimally affects the results. With that being said, for future references, the inflated bird model will be referred to as the 'Bird Model' since there is no tangible difference between models.

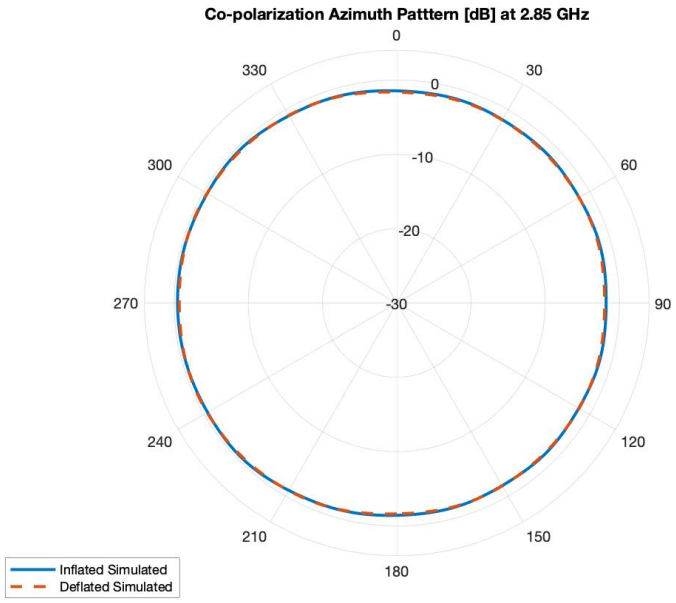

Figure 5.25: Co-polarized Azimuth far-field radiation pattern for the Inflated Bird Model vs the Deflated Bird Model

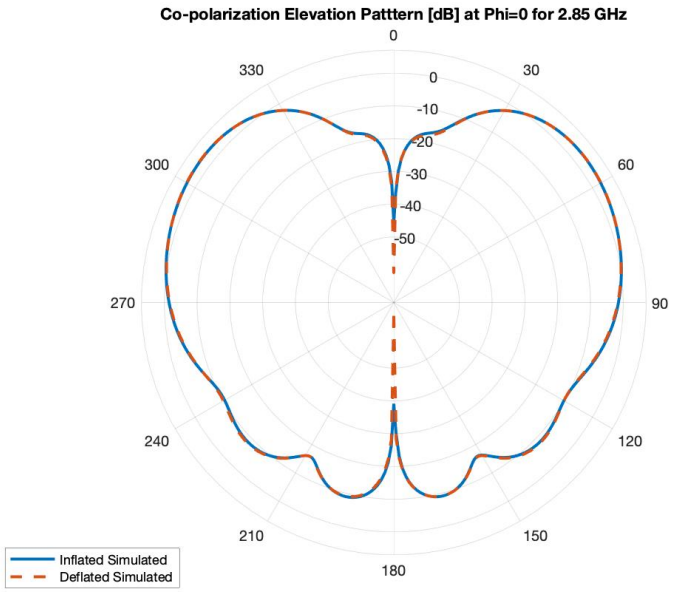

Figure 5.26: Co-polarized Elevation far-field radiation pattern for the Inflated Bird Model vs the Deflated Bird Model at $\Phi = 0$

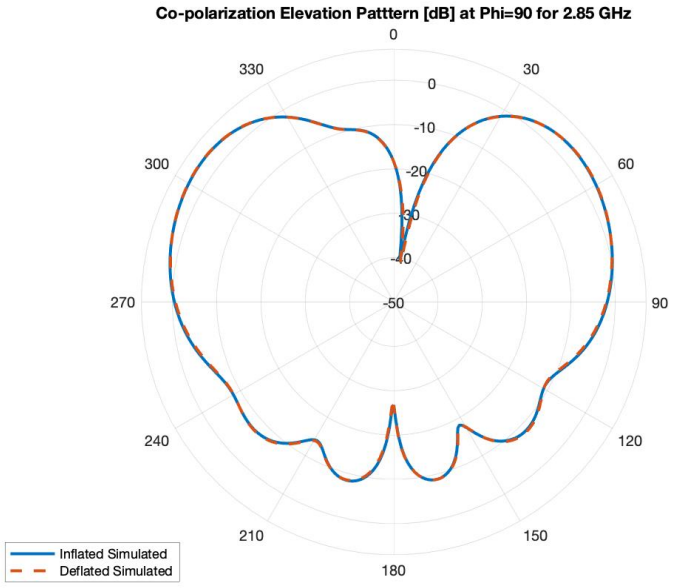

Figure 5.27: Co-polarized Elevation far-field radiation pattern for the Inflated Bird Model vs the Deflated Bird Model at $\Phi = 90$

With known permittivity and conductivity values for the bird model, a direct comparison can be made between the HFSS bird model and the two salvaged carcasses (Bird 1 and Bird 2). Also, a Saline model was simulated in HFSS to show the difference between what was previously done with measurements in [29]. As mentioned previously, in [29], a sponge filled with Saline, which was carved in the shape of a bird, was used to represent a Bird for measurements. This Saline model (with $\epsilon_r = 75$ and $\sigma = 2[S/m]$) was simulated in HFSS to compare to the Bird model designed in this thesis. It is also important to note that the Saline model was positioned in the same position as shown in Figure 5.17 and was modeled without air-sacs and lungs (appearing as a solid ellipsoid shape). In Figure 5.28, the magnitude of the insertion loss ($|S_{11}|$) is shown for both Bird 1, Bird 2, the Bird model with the permittivity and conductivity values listed previously, and the Saline model. This figure shows that the Bird model does align close to what was measured with Bird 1 while Bird 2 has a greater insertion loss at its resonance. It also shows that the Saline model shifts the resonance of the insertion loss down to 2.5 GHz. In Figure 5.29, the input impedance was plotted for Bird 1, Bird 2, the Saline Model, and the HFSS Bird model. As shown in this figure, the bird model does match an average of both Bird 1 and Bird 2 across the frequency span. However, for the Saline model, it shows that it has a significantly higher impedance shift compared to the Bird model. Based on Figure 5.28 and Figure 5.29, it shows that the Saline model is not an accurate representation of a bird while the Bird model (with $\epsilon_r = 1.2$ and $\sigma = 0.004[S/m]$) is.

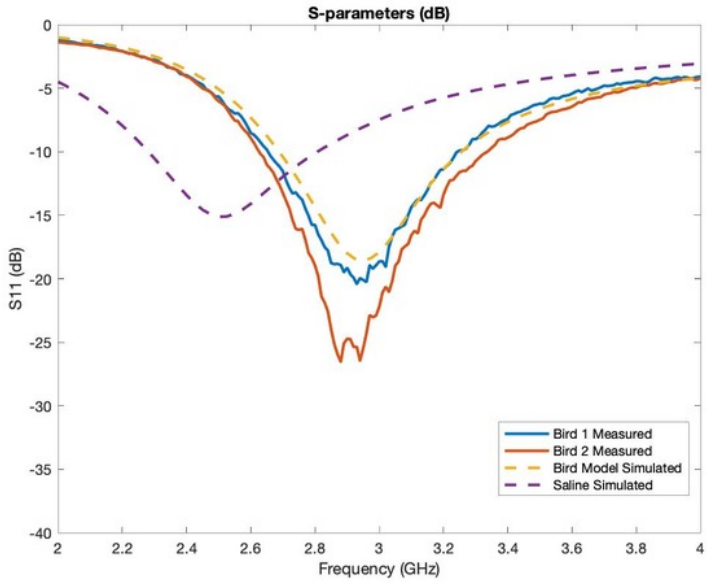

Figure 5.28: Magnitude of Insertion Loss ($|S_{11}|$) in dB plotted across frequency for bird measurements compared to Bird Model

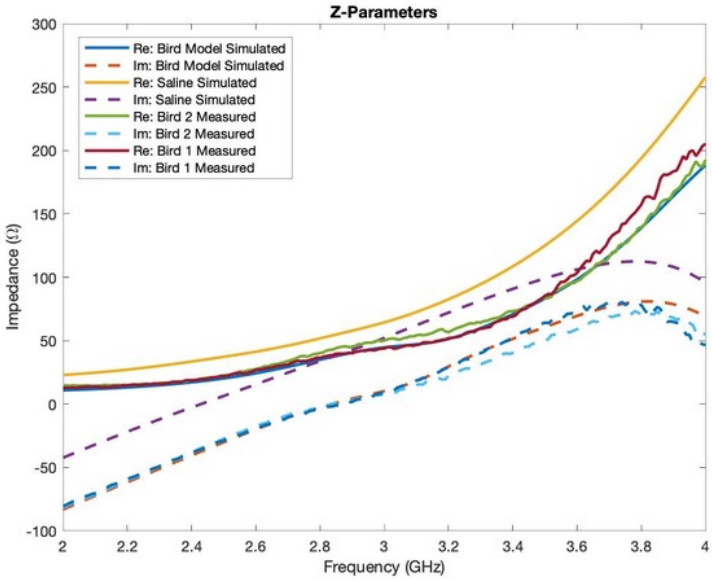

Figure 5.29: Input impedance (Z_{11}) plotted across frequency for bird measurements compared to Bird Model

In Figure 5.30, the Co-polarized Azimuth radiation pattern is shown for Bird 1, Bird 2, the Bird model (with $\epsilon_r = 1.2$ and $\sigma = 0.004[S/m]$), and the Saline model (with $\epsilon_r = 75$ and $\sigma = 2[S/m]$). For the Bird model compared to Bird 1 and Bird 2, it does appear to be that there is a decrease in Gain around the 90 markers and the 270 markers on the polar plot. It is unclear what is causing this dip in radiation pattern Gain. It is clear, however, that the bird is an oversimplified model of actual bird anatomy. Future work will need to be done to characterize more features of a bird's body to match what has been measured. For Future work, finding a way to characterize the Birds head and beak will probably be the next step. By characterizing more significant features of the bird's anatomy, the dips in radiation could be further explained and shown in comparison to measurements. For the Azimuth radiation pattern, the Saline model does appear to align better with the measured Bird carcasses (Bird 1 and Bird 2).

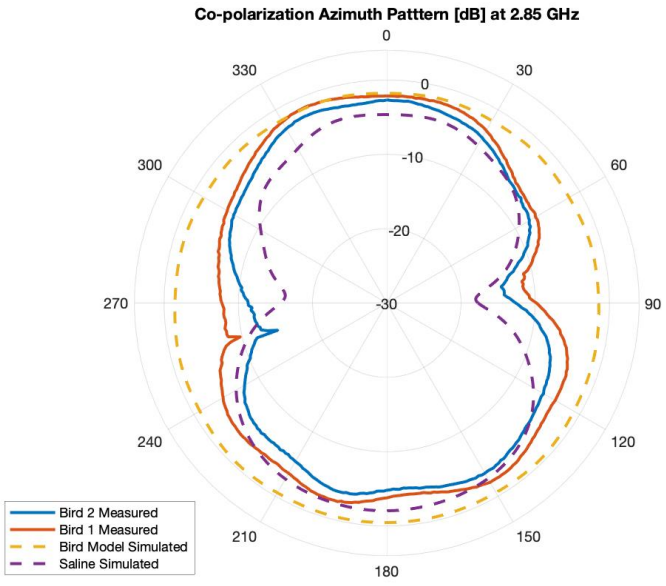

Figure 5.30: Co-polarized Azimuth far-field radiation pattern for birds measurements compared to Bird Model

In Figure 5.31, the Co-polarized Elevation radiation pattern at $\Phi = 0$, for the bird carcasses (Bird 1 and Bird 2), the Bird model and the Saline model. This figure shows that the Saline model has significantly less gain across the radiation pattern. For the Bird model, it appears that it aligns more closely with the impact of the bird carcasses has on the monopole antenna. In Figure 5.32, the Co-polarized Elevation radiation pattern at $\Phi = 90$ for the bird carcasses (Bird 1 and Bird 2), the Bird model and the Saline model. In this figure, there are differences from both the Bird model and the Saline model compared to the bird carcasses (Bird 1 and Bird 2). For the Saline model, it shows to have a bigger null at the bottom and slightly less gain along with one of the sides of the radiation pattern compared to the bird carcasses. For the Bird model, it appears to match most of the radiation patterns of the bird carcasses except for the null at the top of the pattern.

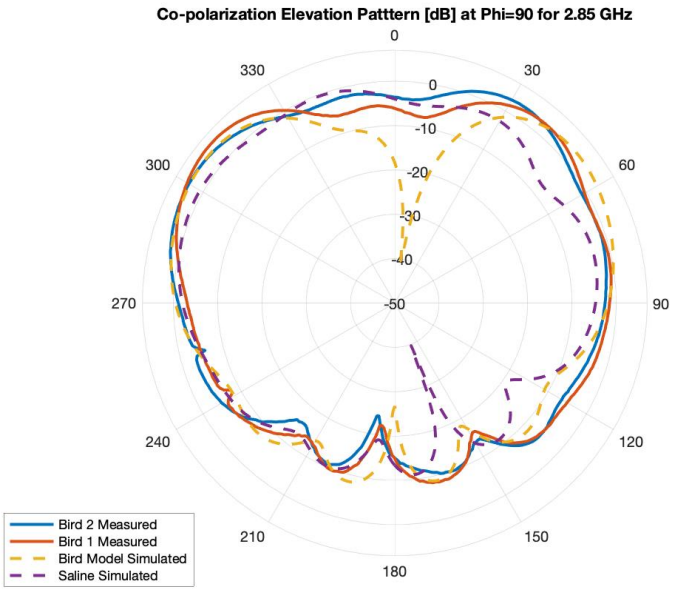

Figure 5.31: Co-polarized Elevation far-field radiation pattern for birds measurements compared to Bird Model at $\Phi = 0$

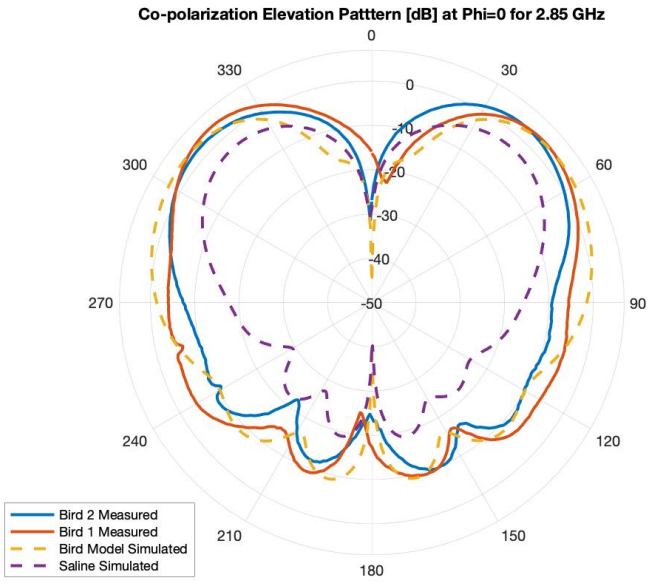

Figure 5.32: Co-polarized Elevation far-field radiation pattern for birds measurements compared to Bird Model at $\Phi = 90$

In another attempt to make the Bird Model more accurate compared to the Bird measurements, a few changes were made to the Bird Model. The Bird model was changed by making an inner and outer volume with the same permittivity values, but different conductivity values. The inner volume was done by shrinking the original bird model (with inflated air-sacs) by about 1.15 inches. Then an outer volume was created around the inner volume (the shrunk bird model) and made the same size as the original Bird Model which is shown in Figure 5.4. The reason this was done was to try to simulate the feather around the bird with the outer volume and have the inner volume represent the torso of the bird. An outer volume with a permittivity of 1.2 and a conductivity value of 0 S/m and an inner volume with a permittivity of 1.2 and a conductivity value of 3 S/m provided the best match between all the antennas parameters and radiation patterns. This Bird model is shown in Figure 5.33. It is important to note that the inner

volume is offset and not centered. This was done to represent the abundance of feathers at the tail end of the Bird.

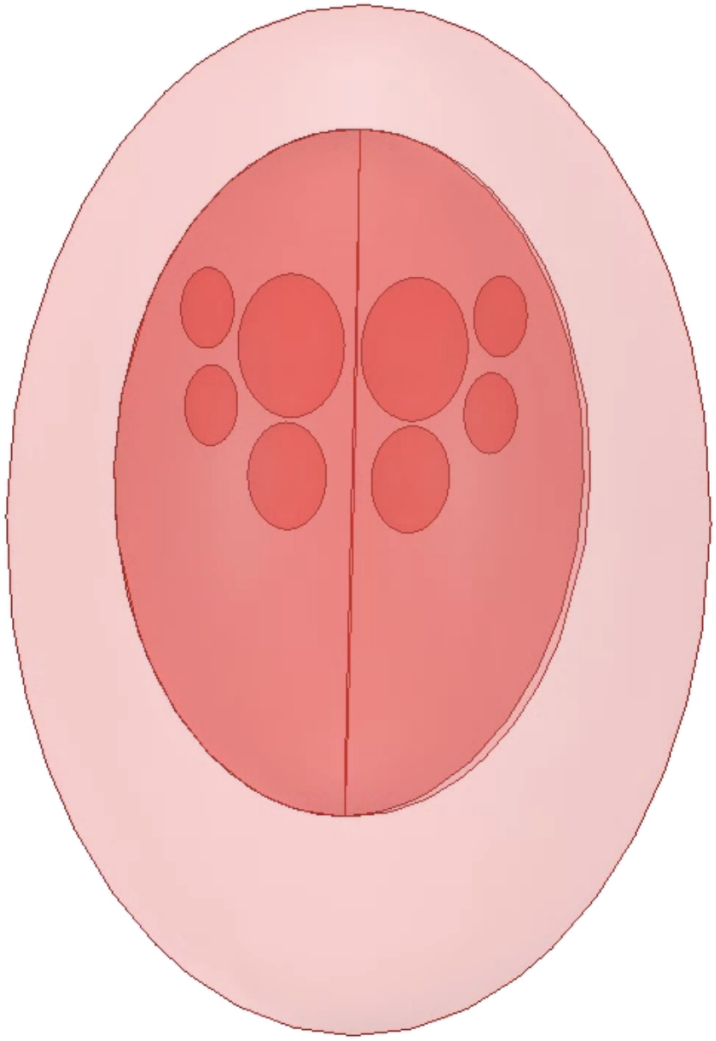

Figure 5.33: Final Bird Model with Inner and Outer Volume

By using $\epsilon_r = 1.2$ and $\sigma = 3[S/m]$ for the inner volume and $\epsilon_r = 1.2$ and $\sigma = 0[S/m]$ for the outer volume, the Bird model appears to match more closely with the results of the birds. In Figure 5.34, the magnitude of the insertion loss ($|S_{11}|$) is shown for the Bird Model (with the previously listed permittivity and conductivity values), the

Saline model, and the Salvaged Bird carcasses (Bird 1 and Bird 2). This figure showed that the Bird Model does have a lower magnitude of insertion loss, but it is overall a more accurate model than the Saline Model. In Figure 5.35, the input impedance was plotted for the Bird Model, the Saline Model, and the salvaged Bird carcasses. This figure shows that the Bird Model closely matches the salvaged bird carcasses and is more accurate than the Saline model.

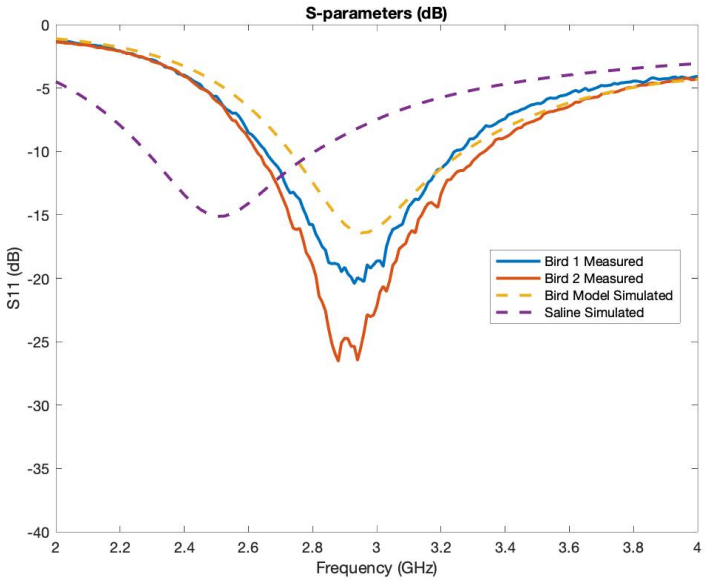

Figure 5.34: Magnitude of Insertion Loss ($|S_{11}|$) in dB plotted across frequency for bird measurements compared to the Final Bird Model

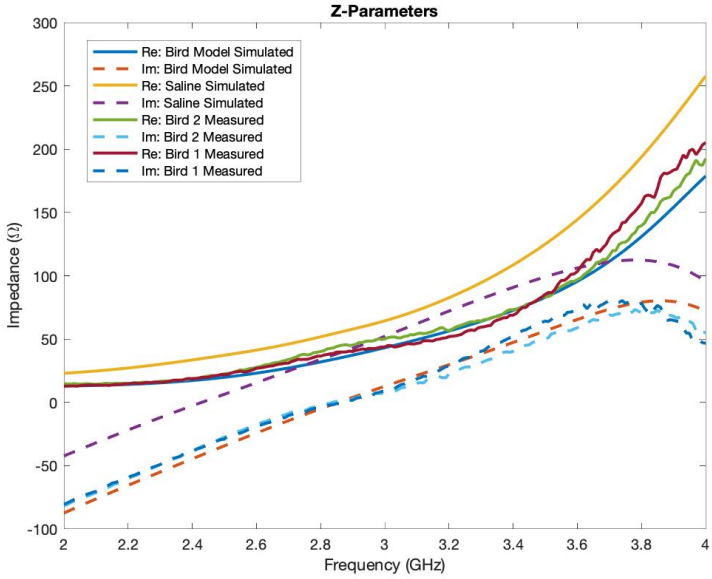

Figure 5.35: Input impedance (Z_{11}) plotted across frequency for bird measurements compared to the Final Bird Model

In Figure 5.36, the Co-polarized Azimuth radiation pattern (at 2.85 GHz) is shown for the Final Bird Model, the Saline Model, and both of the salvaged bird carcasses. This figure shows a better match with the results of Bird and Bird 2 in terms of the overall radiation pattern. It is important to note that the Saline model does have deep nulls on the sides compared to the Bird Model. For future work, finding a way for the Bird Model to characterize these nulls to match more closely to the birds would be the goal.

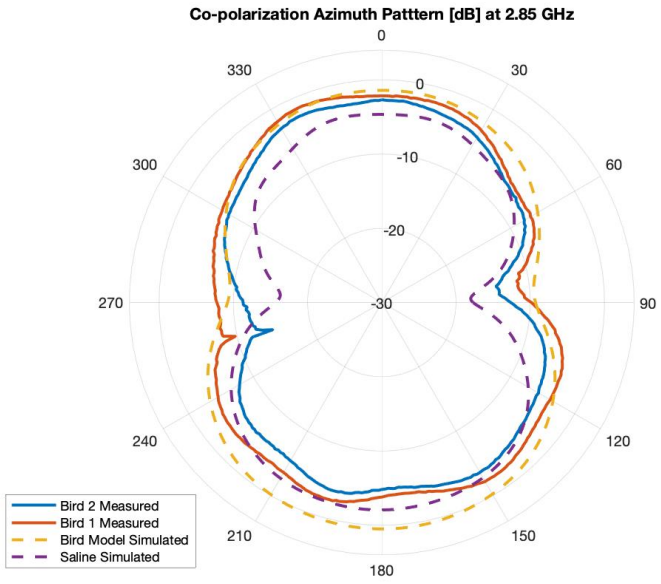

Figure 5.36: Co-polarized Azimuth far-field radiation pattern for birds measurements compared to Final Bird Model

In Figure 5.37 and Figure 5.38, the co-polarized Elevation radiation pattern is shown at $\Phi = 0$ and $\Phi = 90$, respectively. For the Elevation pattern at $\Phi = 0$, it shows that the Saline Model has the overall radiation, but a lower amplitude compared to the results of the birds. However, the Bird Model is still better and matches the radiation pattern of the salvaged birds more than the Saline Model overall. For the Elevation radiation pattern at $\Phi = 90$, it shows that the Bird Model does not have a null at the top of the radiation pattern and matches the birds exceptionally well. Overall, it appears that the Final Bird Model, with $\epsilon_r = 1.2$ and $\sigma = 3[S/m]$ for the inner volume and $\epsilon_r = 1.2$ and $\sigma = 0[S/m]$ for the outer volume, is a more accurate representation of a salvaged Bird carcass compared to the Saline Model from previous methods.

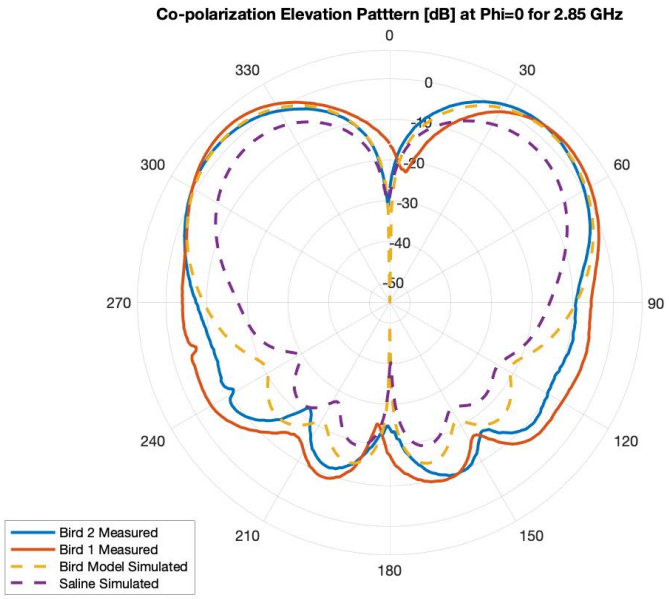

Figure 5.37: Co-polarized Elevation far-field radiation pattern for birds measurements compared to the Final Bird Model at $\Phi = 0$

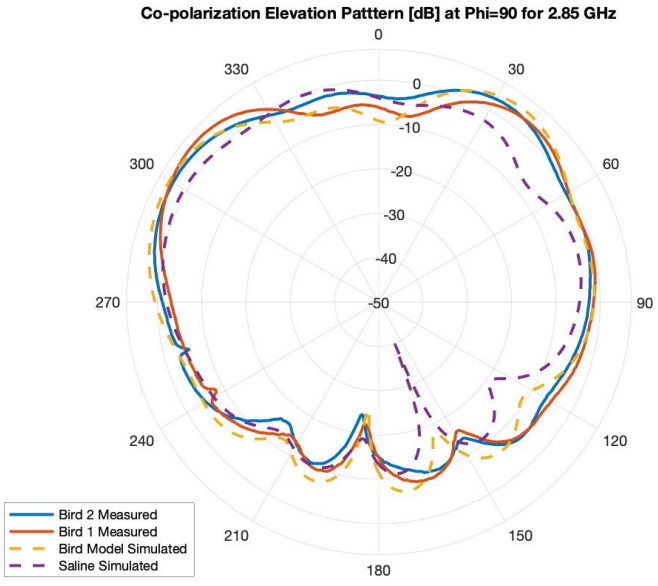

Figure 5.38: Co-polarized Elevation far-field radiation pattern for birds measurements compared to the Final Bird Model at $\Phi = 90$

5.4 Conclusion

In conclusion, salvaged carcasses of Dark-eyed Junco (*Junco Hyemalis*) were used to do Insertion Loss, Impedance, and Far-Field Radiation Patterns measurements on a Ribbon Monopole antenna. The measurement results with the salvaged carcasses were used as a baseline to see how they affect the measured parameters of the antenna. The Final Bird Phantom Model was designed to have $\epsilon_r = 1.2$ and $\sigma = 3[S/m]$ for the inner volume and $\epsilon_r = 1.2$ and $\sigma = 0[S/m]$ for the outer volume. With these permittivity and conductivity values, a simple bird model was able to provide a more accurate representation of a salvaged bird carcass, especially compared to the previous methods of using Saline to represent a bird.

Chapter 6

CFDA Measurements

6.1 Introduction

In this chapter, the Curved Folded Dipole Antenna will be fabricated and measured for analysis. A Balun will be fabricated to feed the CFDA to obtain measurements. Far-field measurements of the CFDA with and without the salvaged bird carcasses will be obtained and analyze the effect the birds have on the CFDA. Lastly, the CFDA will be simulated with the Bird Model to see how it affects the performance of the CFDA.

6.2 CFDA Measurements

The Curved Folded Dipole Antenna (CFDA) was slightly modified to simulate what would be fabricated. To continue from Chapter 4, it was decided that a CFDA with an outer ribbon width ($w2$) of 4 mm and an inner ribbon width ($w1$) of 0.5 mm provided the best results to be seen by the WSR-88D weather Radar at 100 Km. In HFSS, a 5 mil Rogers 5880 substrate was added as a backing substrate to the CFDA. In addition to this, soldering pads were added to feed the antenna via twin leads once it was fabricated. These changes in HFSS can be seen in Figure 6.1. Once these changes were added, the CFDA was tuned to resonant at 2.85 GHz by changing the size of the antenna. Once

this was done, the CFDA was fabricated using the Photo-Lithography process in-house. The fabricated Curved Folded Dipole Antenna with $w1 = 0.5mm$ and $w2 = 4mm$ is shown in Figure 6.2. A penny coin was included in the figure for size comparison.

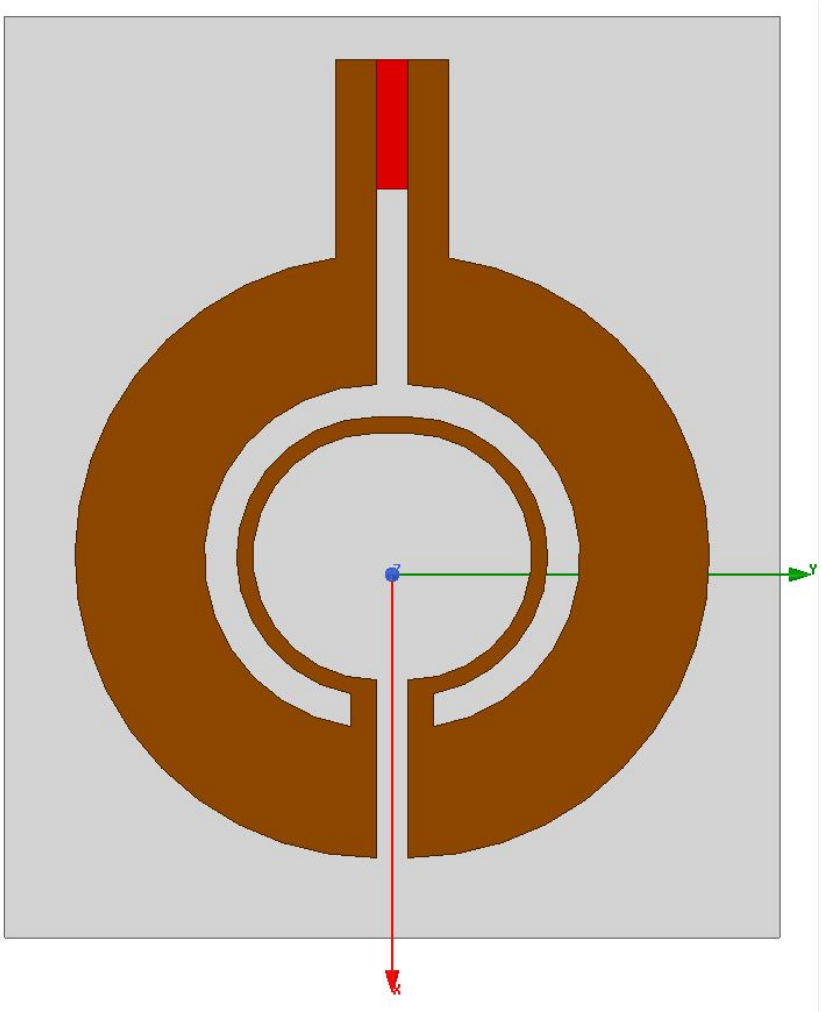

Figure 6.1: Curved Folded Dipole Antenna in HFSS with an inner ribbon width ($w1$) of 0.5 mm and an outer ribbon width ($w2$) of 4 mm

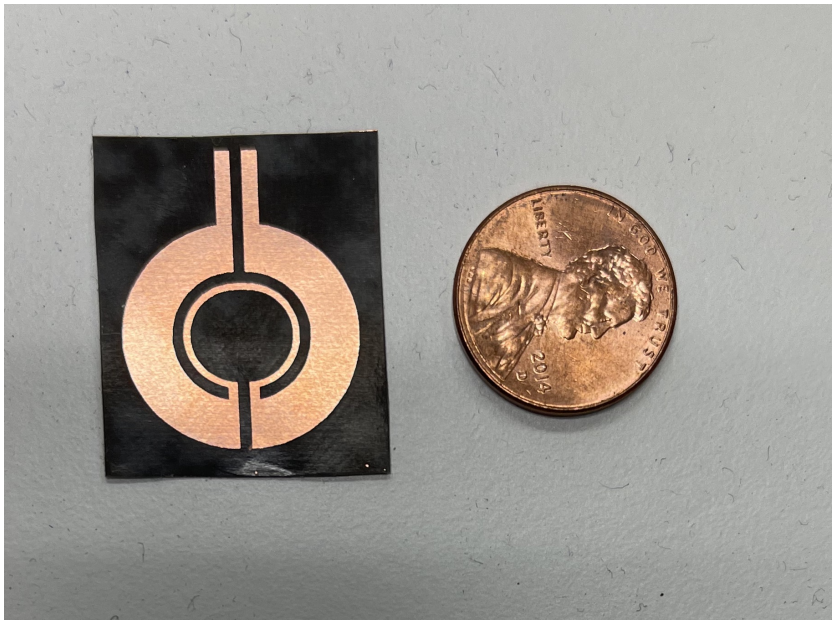

Figure 6.2: Fabricated Curved Folded Dipole Antenna next to a 1 cent coin (penny) for Size comparison

To feed the CFDA, a Bazooka Balun was used to deal with common-mode currents within the Frequency span of interest. This was done because the CFDA is a balanced structure while a coax cable (commonly used for measurements) is an unbalanced structure. A Bazooka Balun was designed to be $\frac{\lambda}{4}$ at 2.85 GHz in HFSS and was simulated to plot the Common Mode Rejection Ratio (CMRR). By tuning the length of the Balun and making it slightly smaller than a $\frac{\lambda}{4}$ (with a length of 42 mm and a width of 0.5 inches), a CMRR above 40 dB was achieved centered at 2.85 GHz. The Bazooka Balun was then fabricated in-house using 3D printing methods and was then electroplated to add a layer of copper. 3D printing and electroplating the Balun, provided more accuracy to get the Balun close to the simulated length. In Figure 6.3, (a) the fabricated Bazooka Balun is shown and (b) the Common Mode Rejection Ratio (CMRR) for that fabricated Balun is also shown. It was decided that a CMRR above 25 dB (within 2.7 GHz and 3 GHz) is sufficient for this application considering the

bandwidth of operation. Since the CFDA will be measured with the Bazooka Balun, the CFDA was simulated with the Balun attached to it in HFSS.

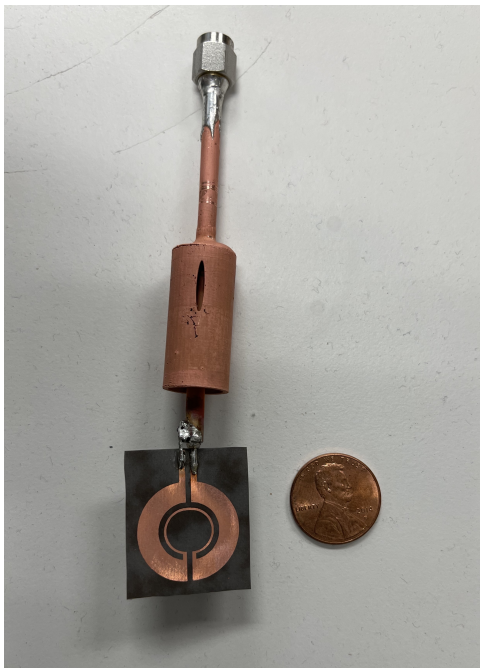

(a)

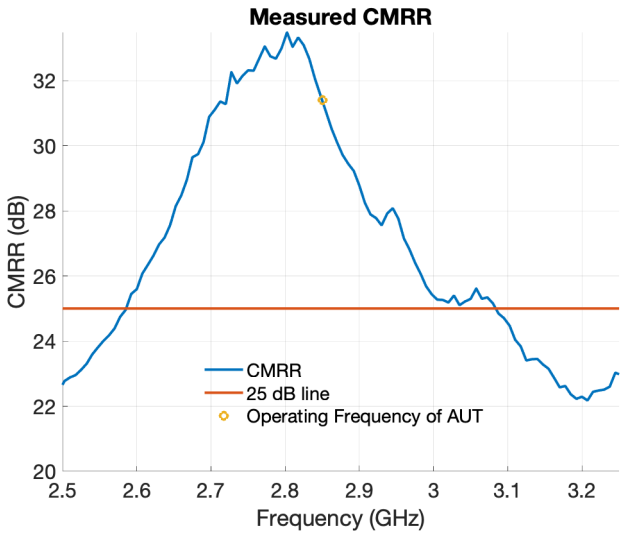

(b)

Figure 6.3: (a) Fabricated Bazooka Balun soldered to CFDA (b) Common Mode Rejection Ratio (CMRR) in dB plotted across frequency

In Figure 6.4 and Figure 6.5, the magnitude of the insertion loss ($|S_{11}|$) and the input impedance (Z_{11}) is shown for the CFDA with and without the Bazooka Balun and the measured results. In Figure 6.4, it does show that the Bazooka Balun is affecting the measured results of the CFDA since the response of the simulated and fabricated CFDA with the Balun does match more closely. This does, however, show that even with the Balun model in HFSS, the fabricated Bazooka Balun is impacting the CFDA more than what is simulated. In Figure 6.5, it shows that the impedance parameters of the simulated response similar to the measured results, but it is shifted higher in frequency. An uncertainty when simulating the Balun is the dielectric of the semi-rigid coax cable used for measurements. In Figure 6.6, several dielectric constants were simulated in HFSS, and was shown that a dielectric of 3.5 provides a better match to the measured results. However, with a permittivity of 3.5, the impedance parameters are lower in magnitude. The behavior of the antenna is only limited to do the feeding method. Once the antenna is attached to the Hybrid RFID circuit, a chip Balun will be used to feed the CFDA instead. This will reduce the impact on the CFDA results.

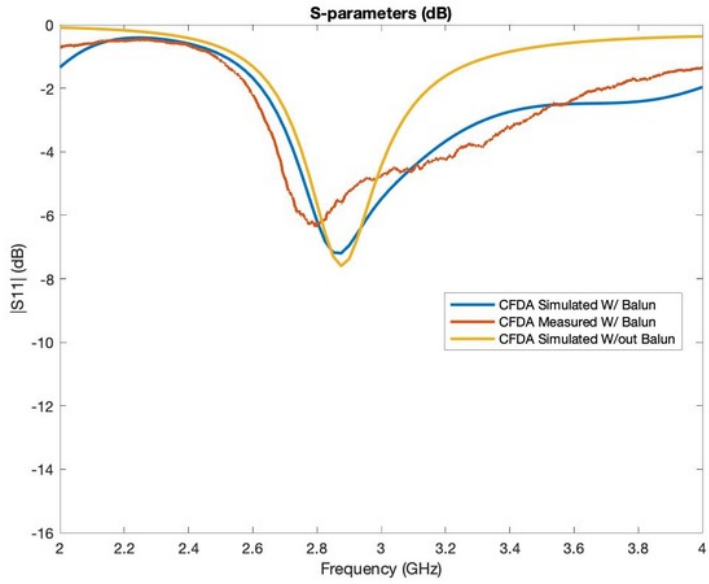

Figure 6.4: Magnitude of Insertion Loss ($|S_{11}|$) in dB plotted across frequency for the Simulated vs Measured CFDA

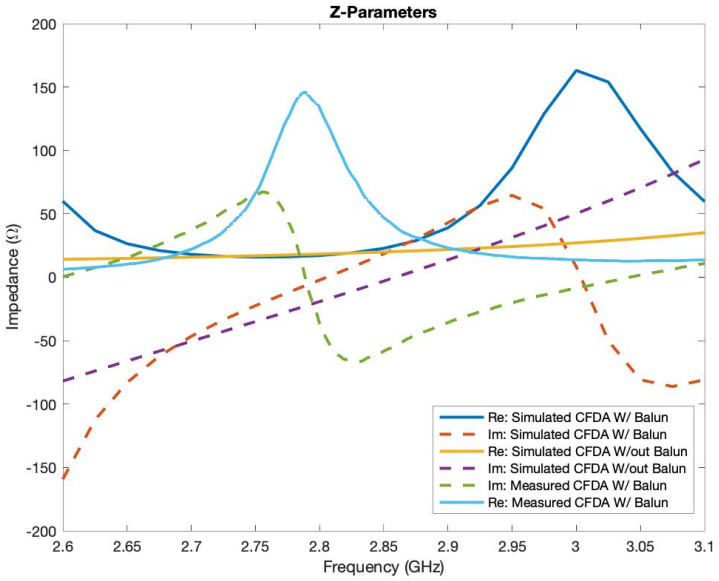

Figure 6.5: Input impedance (Z_{11}) plotted across frequency for the Simulated vs Measured CFDA

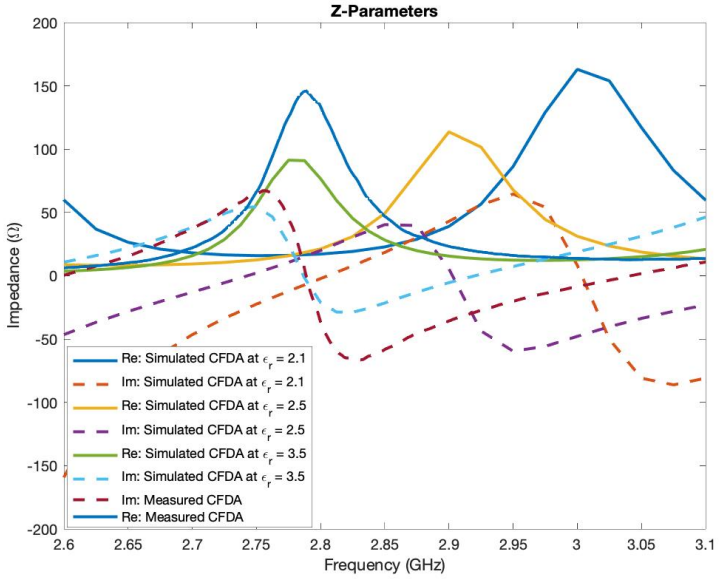

Figure 6.6: Input impedance (Z_{11}) plotted across frequency for the Simulated vs Measured CFDA at various Dielectric constants

In Figure 6.7, the set-up that was used to take the far-field Azimuth radiation pattern is shown. In Figure 6.8, the co-polarized Azimuth radiation pattern is shown for the Curved Folded Dipole Antenna (CFDA) with and without the Balun in HFSS and the measured results with the Balun. This figure shows that the Azimuth radiation pattern in HFSS is omnidirectional for the CFDA without the Bazooka Balun. It also shows that once a Bazooka Balun is included, it starts to affect the radiation pattern of the CFDA. It shows that there is a null produced around mark 270 on the polar plot.



Figure 6.7: Azimuth radiation pattern Set-up for CFDA

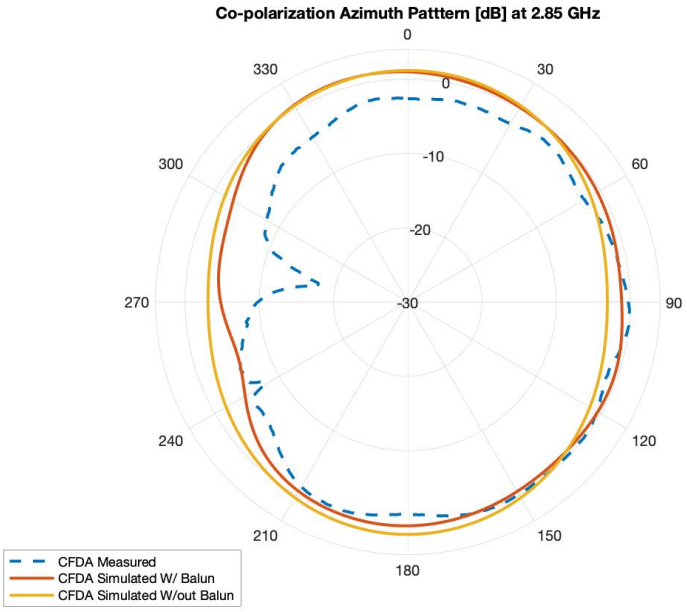

Figure 6.8: Co-polarized Azimuth far-field radiation pattern for CFDA (Simulated vs Measured)

This null in the measured radiation pattern can be accredited to the cable currents of the Balun. In Figure 6.9, surface currents are plotted on the surface of the outer conductor of the Balun in HFSS. This shows that as the frequency gets higher, the amount of surface currents increases, especially past the Balun. This means that the Balun is not working properly at higher frequencies. In Figure 6.10, the radiation pattern is overlaid with the CFDA and the Balun and it does show the rear end of the Balun is positioned where the null is being created. This figure also shows that since there are fewer surface currents at 2.7 GHz, the null in the measured radiation pattern is reduced and no longer appears. Unfortunately, this is the impact the Bazooka Balun has on the CFDA in the measurements. For future applications, a better feeding method such as a chip Balun (when attaching it to the Hybrid RFID tag) can be used and prevent this effect it has on the radiation patterns.

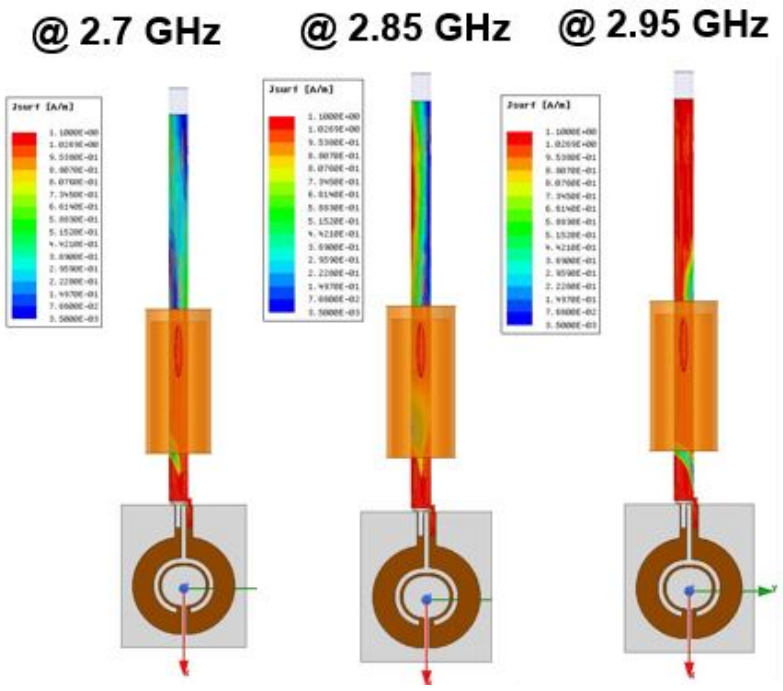

Figure 6.9: CFDA with Balun attached shown in HFSS with surface currents plotted on the Coax cable at 2.7 GHz, 2.85 GHz, and 2.95 GHz

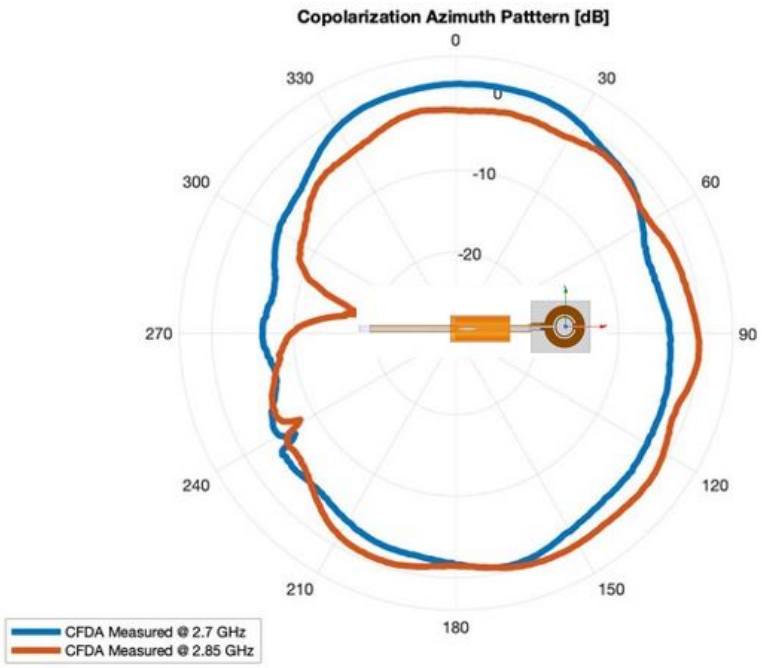

Figure 6.10: Measured Azimuth Radiation Pattern (at 2.85 GHz and 2.7 GHz) overlaid on top of the CFDA with Balun in HFSS

In Figure 6.11, the set-up that was used to take the far-field Elevation radiation pattern at $\Phi = 0$ and $\Phi = 90$ is shown. In Figure 6.12 and Figure 6.13, the Elevation radiation pattern at $\Phi = 0$ and $\Phi = 90$, respectively, is shown for the CFDA at 2.85 GHz. In Figure 6.12, it shows that the measured Elevation radiation pattern at $\Phi = 0$ is omnidirectional and does match with the CFDA with the Balun in the HFSS simulation. In Figure 6.13, the overall take from this figure shows that there a difference between the CFDA with and without a Balun. The nulls on the sides get reduced and become slightly shifted by adding the Bazooka Balun to the HFSS simulation. The measured results of the CFDA with the Balun (at 2.85 GHz) do show that these nulls are completely removed and it shows that there is a ripple in the radiation pattern at the bottom. This ripple can be accredited to the cable currents that are affecting the radiation pattern. In fact, by looking at the same cut plan but at 2.7 GHz (in Figure

6.14), it shows that the radiation patterns begins to match with the simulation results.

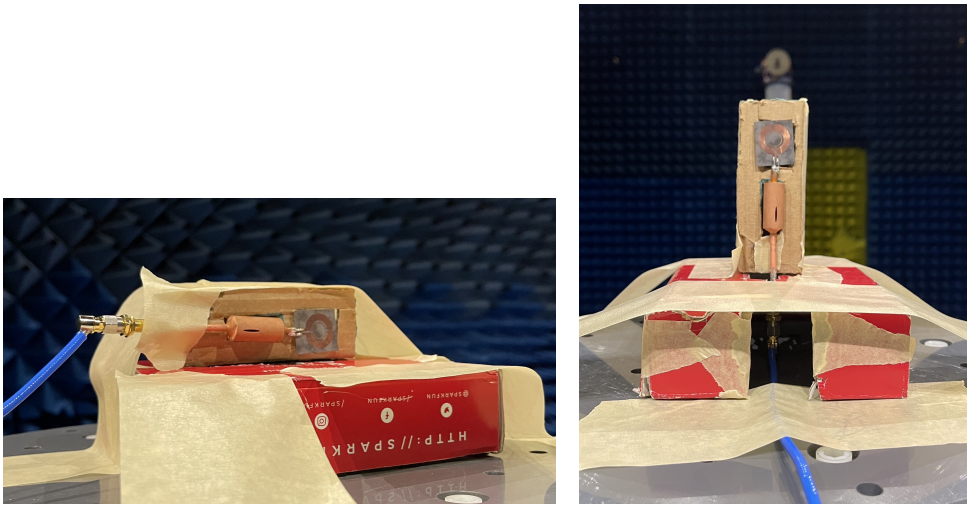

(a) (b)

Figure 6.11: Elevation radiation pattern Set-up for CFDA at (a) $\Phi = 0$ and (b) $\Phi = 90$

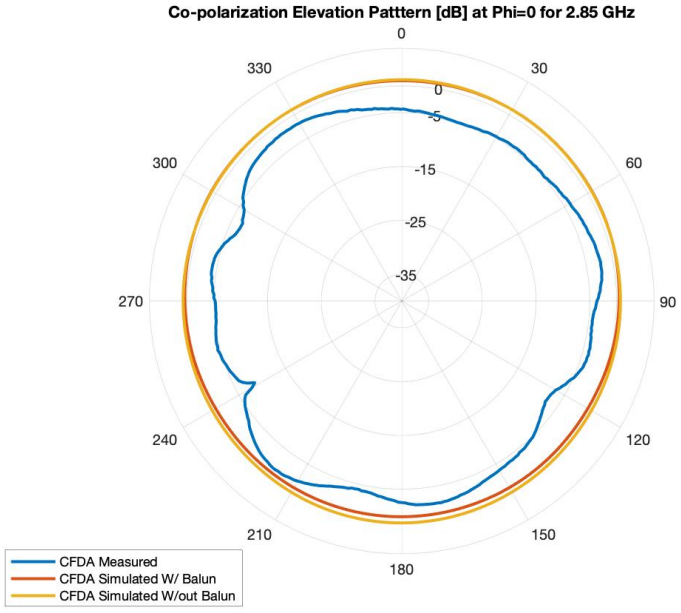

Figure 6.12: The Simulated Co-polarized Elevation far-field radiation pattern for the CFDA (for 2.85 GHz) at $\Phi = 0$

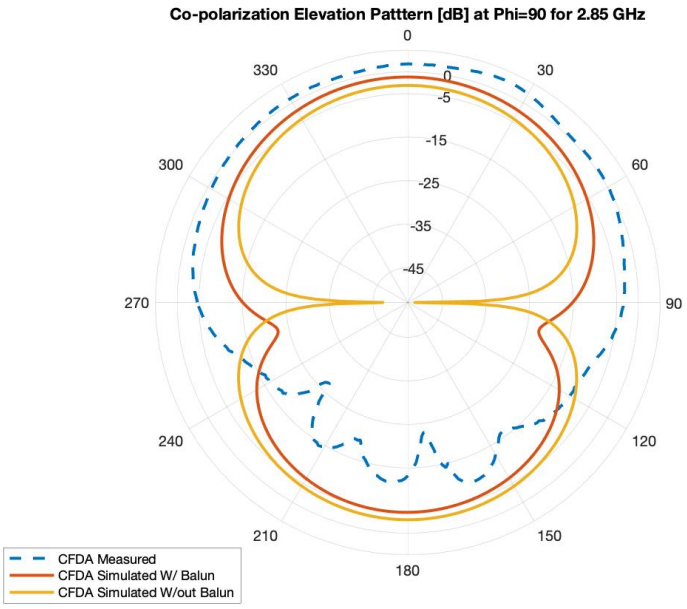

Figure 6.13: Co-polarized Elevation far-field radiation pattern for the CFDA (for 2.85 GHz) at $\Phi = 90$

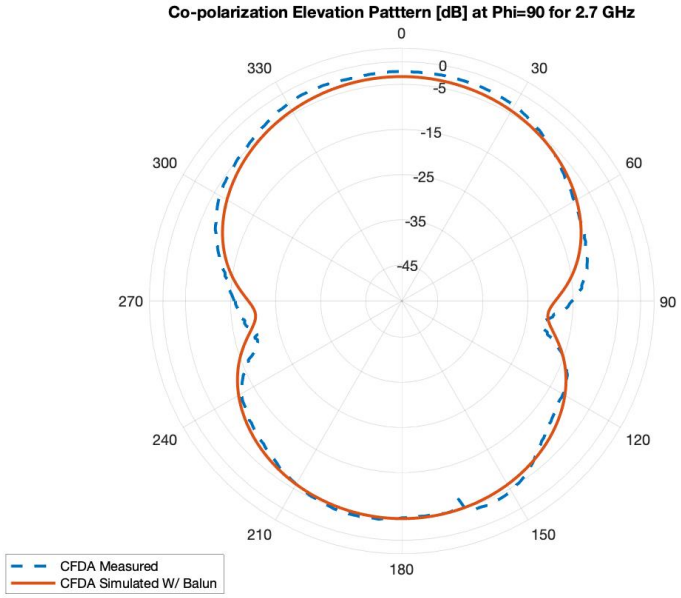

Figure 6.14: Co-polarized Elevation far-field radiation pattern for the CFDA (for 2.7 GHz) at $\Phi = 90$

Now that the CFDA has been validated with simulations and have accredited the mismatches in radiation pattern due to surface currents (cable currents), it is important to see how the CFDA is affected by the salvaged bird carcasses. Figure 6.15, shows how the salvaged carcasses were positioned with respect to the CFDA during the measurements. In Figure 6.16, the co-polarized Azimuth radiation pattern at 2.85 GHz is shown for the measured CFDA (with the Balun) and with Bird 1 and Bird 2 attached. This figure shows that the measured radiation pattern between Bird 1 and Bird 2 is consistent between them. When comparing the birds to the CFDA, the results vary in the magnitude of the radiation pattern, but the overall pattern stays consistent. It is important to note that the null of the CFDA is reduced and adds ripples in the radiation patterns when adding the birds in the measurements. In Figure 6.17, the same things are being compared, but at 2.7 GHz. This figure shows that with fewer cable currents, the Azimuth radiation pattern appears to become omnidirectional and the nulls are removed. They would infer that the salvaged bird carcasses do not have a great impact on the Azimuth radiation pattern.

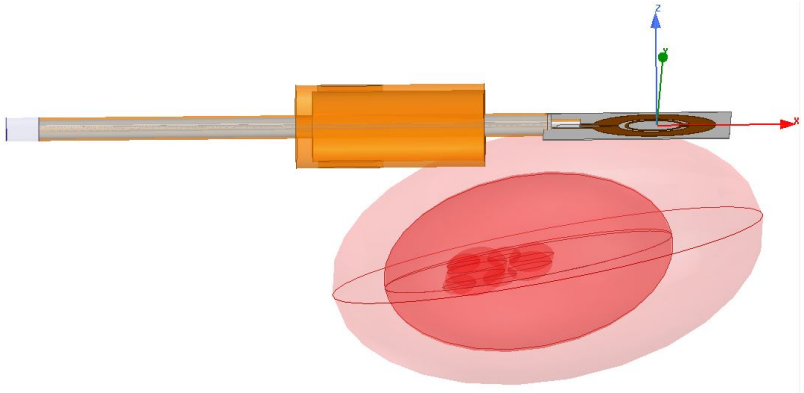

Figure 6.15: Representation of how salvaged bird carcasses were positioned for measurements

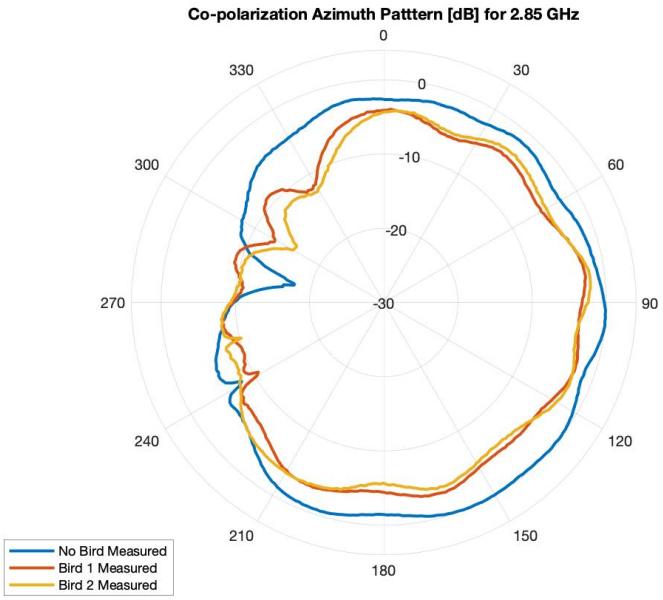

Figure 6.16: Co-polarized Azimuth far-field radiation pattern (at 2.85 GHz) for CFDA with salvaged bird carcasses

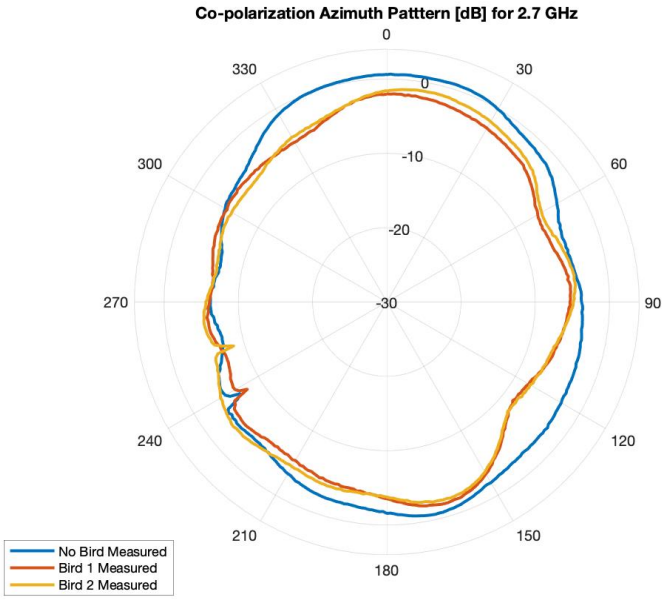

Figure 6.17: Co-polarized Azimuth far-field radiation pattern (at 2.7 GHz) for CFDA with salvaged bird carcasses

In Figure 6.18, the co-polarized Elevation radiation pattern for 2.85 GHz at $\Phi = 0$ is shown. This figure shows that Bird 1 and Bird 2 are consistent and match well for this cut plane, even when compared to the CFDA. This would infer that the Birds do not affect the radiation pattern much for this cut plane. In Figure 6.19, the co-polarized Elevation radiation pattern for 2.7 GHz at $\Phi = 0$ is shown. Similar to the previous figure, the cable currents, nor the birds, appear to affect this radiation cut plane. In Figure 6.20, the co-polarized Elevation radiation pattern for 2.85 GHz at $\Phi = 90$ is shown. In this figure, the results between Bird 1 and Bird 2 stay consistent when compared to each (other apart from some slight magnitude discrepancies). When comparing the measured CFDA (by itself) to the salvaged bird carcasses, it appears that the CFDA matches closely to the birds except for the ripple in the radiation pattern toward the bottom. When looking at the same cut plane, but at 2.7 GHz in Figure 6.21, the results begin to start matching more with each other. With fewer cable currents to affect the radiation pattern, Figure 6.21 shows that the salvaged bird carcasses make a minor impact on the CFDA.

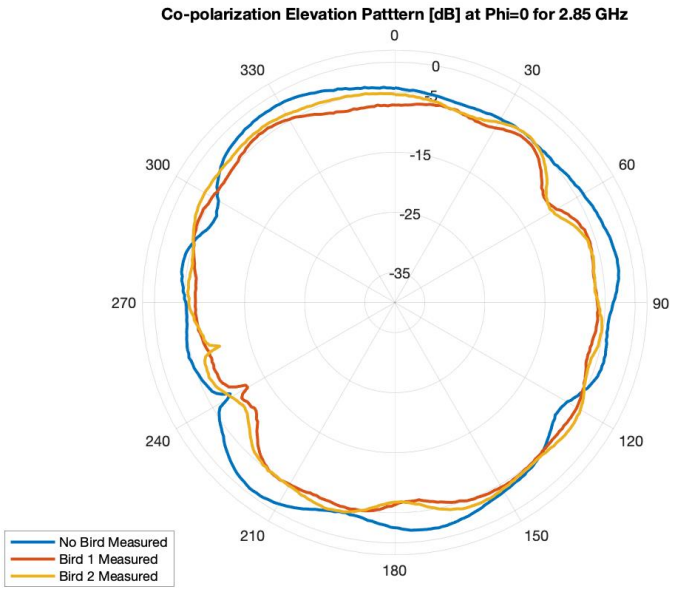

Figure 6.18: Co-polarized Elevation far-field radiation pattern for the CFDA (for 2.85 GHz) at $\Phi = 0$ with salvaged bird carcasses

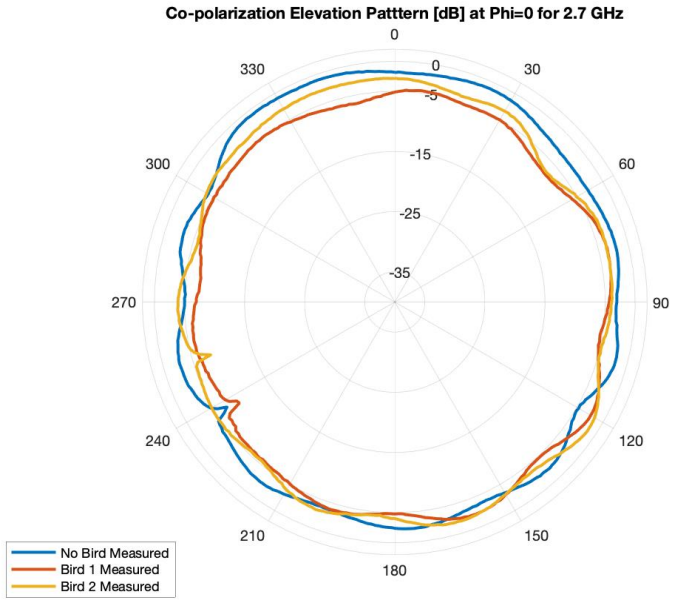

Figure 6.19: Co-polarized Elevation far-field radiation pattern for the CFDA (for 2.7 GHz) at $\Phi = 0$ with salvaged bird carcasses

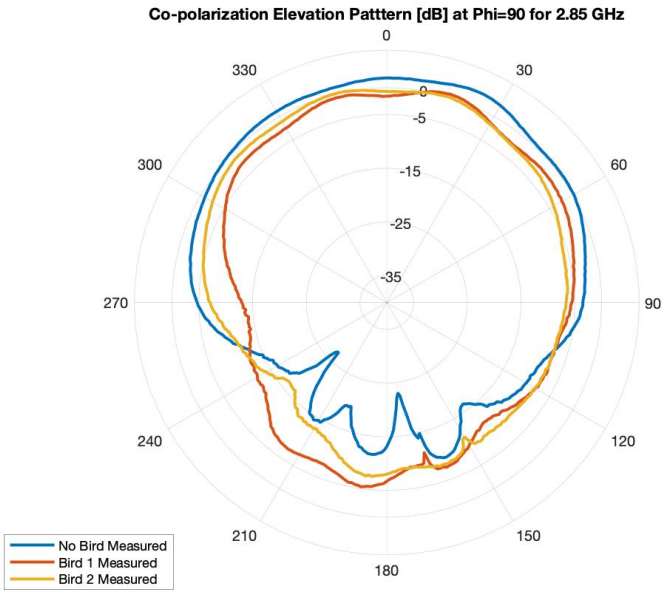

Figure 6.20: Co-polarized Elevation far-field radiation pattern for the CFDA (for 2.85 GHz) at $\Phi = 90$ with salvaged bird carcasses

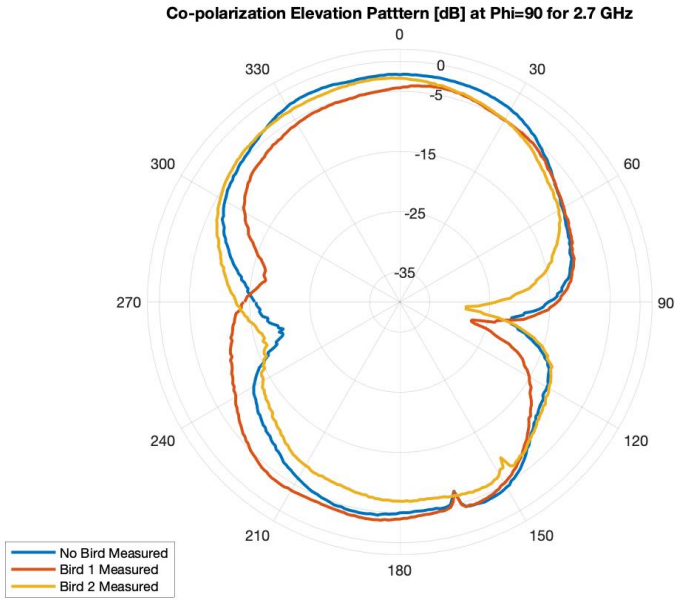

Figure 6.21: Co-polarized Elevation far-field radiation pattern for the CFDA (for 2.7 GHz) at $\Phi = 90$ with salvaged bird carcasses

By finding a better feeding method, the effects of surface currents (cable currents) can be eliminated and a proper comparison can be made for the radiation patterns at 2.85 GHz. For now, a comparison of the simulated CFDA (without a Balun) can be shown with and without the previously designed Bird Model. The position of the Bird Model with respect to the CFDA (for the simulated results) can be shown in Figure 6.22. In Figure 6.23 and Figure 6.24, the magnitude of the insertion loss ($|S_{11}|$) and the input impedance (Z_{11}) is shown, respectively, for the CFDA with and without the Bird Model. In Figure 6.23, it shows that the magnitude of the insertion loss will reduce when adding the Bird Model. Figure 6.24, shows that the Bird Model does not affect the impedance parameters of the CFDA, which means there would be no shift in resonance.

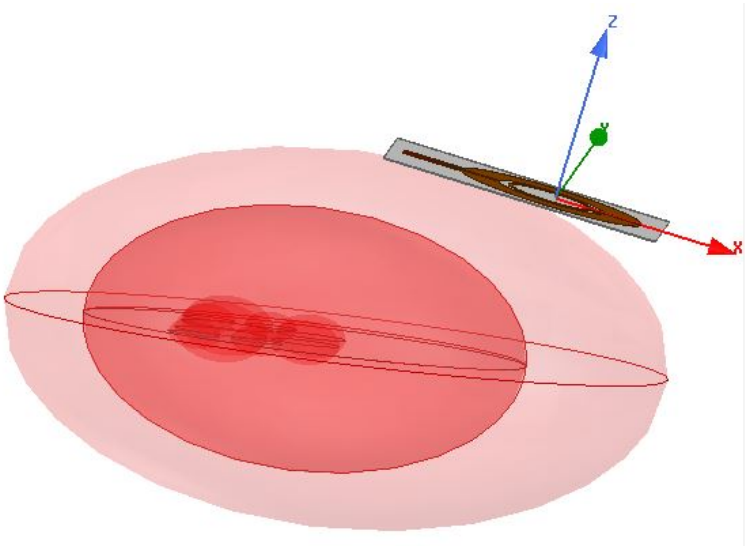

Figure 6.22: Representation of Bird Model was positioned for simulations

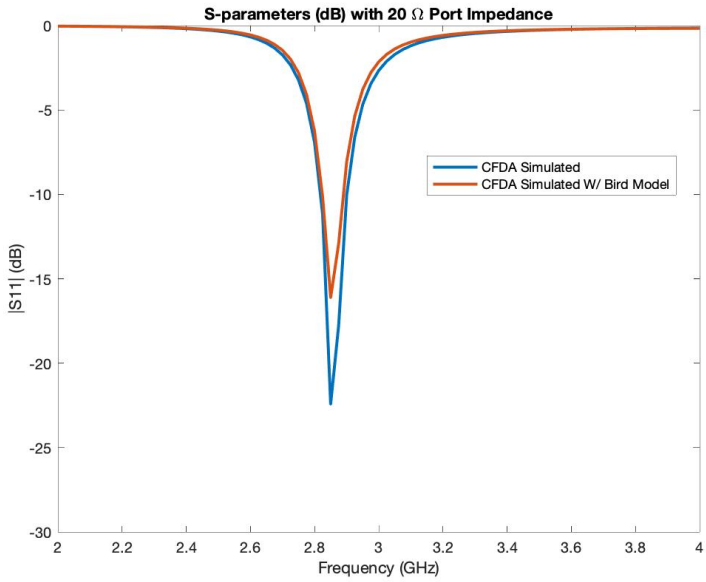

Figure 6.23: Magnitude of Insertion Loss ($|S_{11}|$) in dB plotted across frequency for the Simulated CFDA

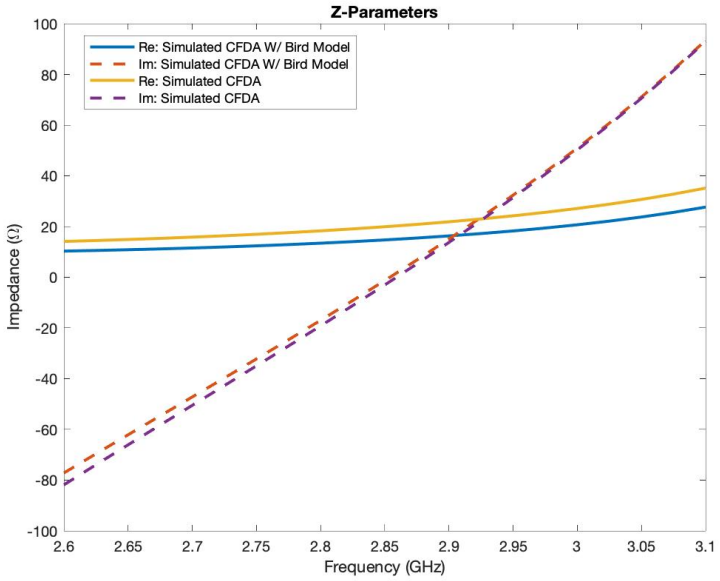

Figure 6.24: Input impedance (Z_{11}) plotted across frequency for the Simulated CFDA

In Figure 6.25, the simulated co-polarized Azimuth radiation pattern is shown for the CFDA (without a Balun) with and without the Bird Model. This figure does show that there is a slight impact of the azimuth radiation pattern when adding the Bird Model to the CFDA. However, the impact is minor and the overall pattern still stays omnidirectional. In Figure 6.26, the simulated co-polarized Elevation radiation patterns at $\Phi = 0$ and $\Phi = 90$ is shown for the CFDA with and without the Bird Model. The overall consensus in these figures shows that the Bird Model does not affect the radiation patterns of these cut planes. This infers that when this quasi-isotropic Curved Folded Dipole Antenna is attached to an actual bird, there will be minor effects on the overall performance of the antenna.

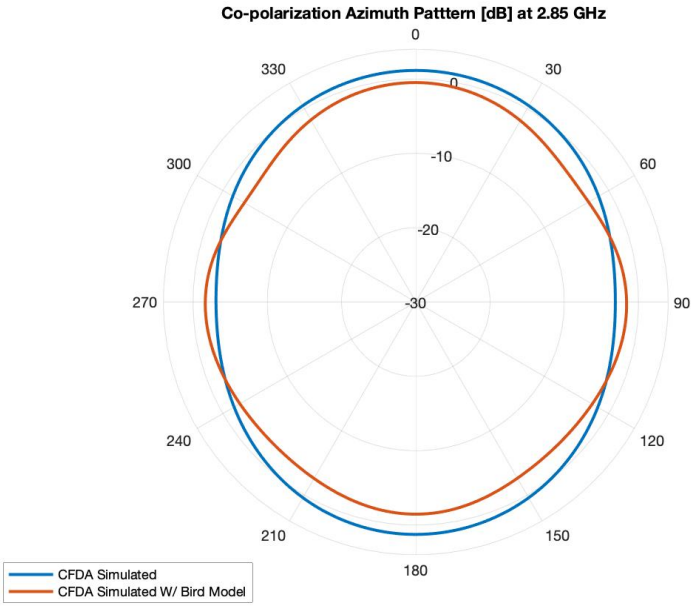

Figure 6.25: Simulated Co-polarized Azimuth far-field radiation pattern (at 2.85 GHz) for CFDA with Bird Model

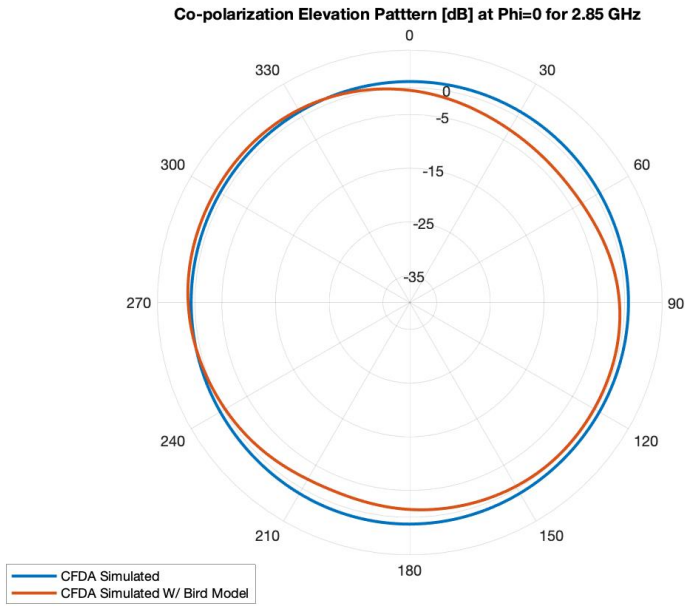

(a)

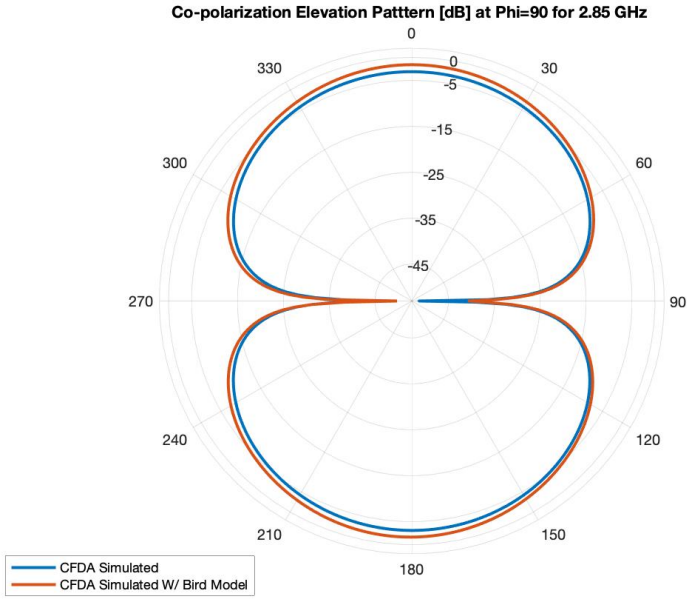

(b)

Figure 6.26: Simulated co-polarized Elevation radiation pattern (at 2.85 GHz) for CFDA with Bird Model (a) at $\Phi = 0$ and (b) at $\Phi = 90$

It is important to note that there is a null in the co-polarized radiation pattern for the Elevation cut plane for $\Phi = 90$. This null will not affect the overall performance of the CFDA because the total gain (considering both polarizations) is omnidirectional. This is shown in Figure 6.27 where the Elevation radiation pattern at $\Phi = 90$ is shown for the Phi polarization, Theta polarization, and the Total Gain.

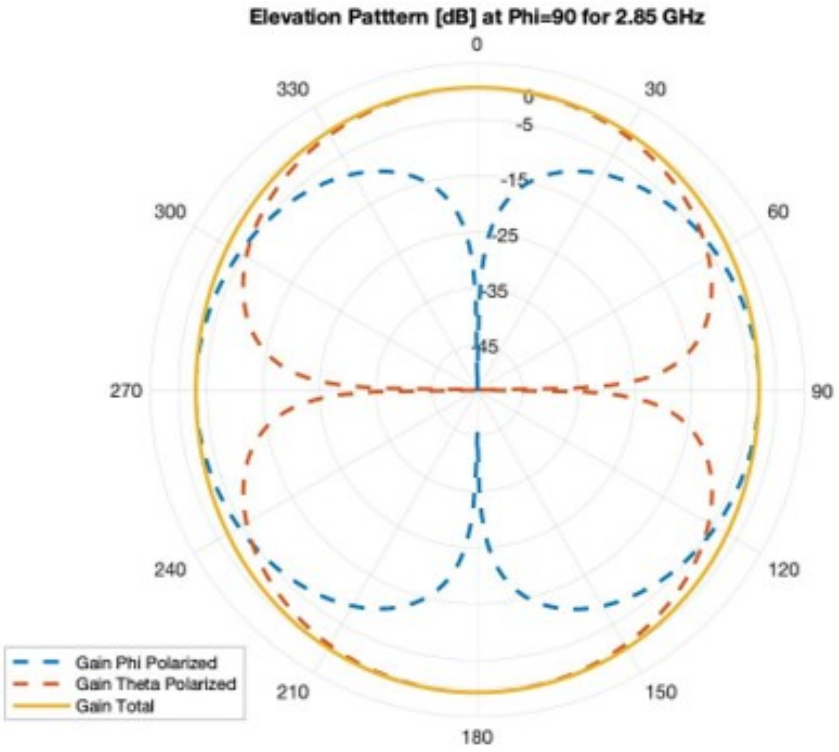

Figure 6.27: Simulated Elevation radiation pattern (at 2.85 GHz) for CFDA at $\Phi = 90$ for Phi polarized, Theta polarized, and total Gain

6.3 Conclusion

In conclusion, the Curved Folded Dipole Antenna (CFDA) was fabricated and measured in this chapter. A Bazooka Balun was designed and fabricated (using 3D printing and electroplating process) to be used as a feeding method for the CFDA and had a

Common Mode Rejection Ratio (CMRR) above 25 dB across the frequencies of interest. When measuring the CFDA with the Balun, it showed that the Balun affected the response of the CFDA. In addition, it was proven that cable currents from the Balun were causing the radiation patterns results to have abnormalities, such as ripple or a null in the radiation pattern. This was shown by plotting the surface currents (cable currents) on the simulated Balun design at 2.7 GHz, 2.85 GHz, and 2.95 GHz. At these frequencies, the surface currents increased as the frequency increased. By plotting the radiation pattern at 2.85 GHz (with surface currents) and 2.7 GHz (with fewer surface currents), the abnormalities in the radiation patterns were proven to have been caused by the cable currents. lastly, the simulated CFDA was also compared to Bird Model to see the overall effect of the Bird model on the CFDA.

Chapter 7

Hybrid RFID Circuit Layout

7.1 Introduction

In this chapter, the Hybrid RFID tag will be explained on how it is connected and what components will be used for the prototype. The changes on what components are used for this circuit layout will be explained and show how that reduces the overall weight of the circuit. Also, the designed circuit layout will be fabricated using a Laser ether and will be used for future measurements.

7.2 Hybrid RFID Circuit Layout

The working prototype of the Hybrid RFID tag was designed and measured in [8]. This design proved that the tag can backscatter in Amplitude Shift Keying (ASK) Modulation and provided a list of proposed components that can be used to build a circuit prototype. This list of the proposed components and their corresponding weight can be shown in Table 7.1. However, a few changes were made to the list of components that will be used for the circuit tag. In Table 7.2, the list of components that are being used to build a circuit layout prototype is shown. Some of the changes made include the use of a BR-1225A battery rather than an ECR2450 battery and using a Rogers 4350B

(with 30 mil thickness) rather than an FR4 board. It is also important to note that the CR1250 battery has a battery holder included with the battery. This change in battery source provided approximately a 9-gram reduction in weight which is significant. Also, it was decided to not use an amplifier for this first circuit layout prototype.

Table 7.1: List of Components and their corresponding weight for the Hybrid RFID Tag from [8]

Part Description	Part Number	Weight (g)
RF Switch	HMC550ae	0.016
Envelop Detector	LTC5505-2	0.012
Binary Counter	SN74HC393NSR	0.2
Quad-Amplifier	LM324AN	0.260
Watch Battery	ECR2450	6.8
Battery Holder	BU2450SM-JJ-GTR	2.37
FR4 Board	N/A	1.33

Table 7.2: Updated List of Key Components and their corresponding weight for the Hybrid RFID Tag for circuit layout prototype

Part Description	Part Number	Weight (g)
RF Switch	HMC550ae	0.016
Envelop Detector	LTC5505-2	0.012
4 Bit Binary Counter	74LVC161D	0.142
Watch Battery	BR-1225A	0.8
30 mil Rogers 4350B	N/A	N/A

Also, a general circuit schematic was provided in [8] to show how the components

connect. This circuit schematic is shown in Figure 7.1. To make a circuit layout, the packaging of each device (provided by the datasheets for each device) was used to create a circuit layout footprint. Based on the packaging information provided by the RF Detector datasheet, it was decided that all components have soldering pads of 0.754 mm (width) by 0.854 mm (length) in size. This would provide sufficient space to solder the leads of the devices to the copper pads. Each component footprint was custom made in Microwave Office (AWR) and was based on the spacing packaging from their datasheet. In Figure 7.2, the custom-made layouts footprints for the RF detector, RF Switch, and the 4-Bit Counter are shown. It is important to note that the diagram from each component is not to scale.

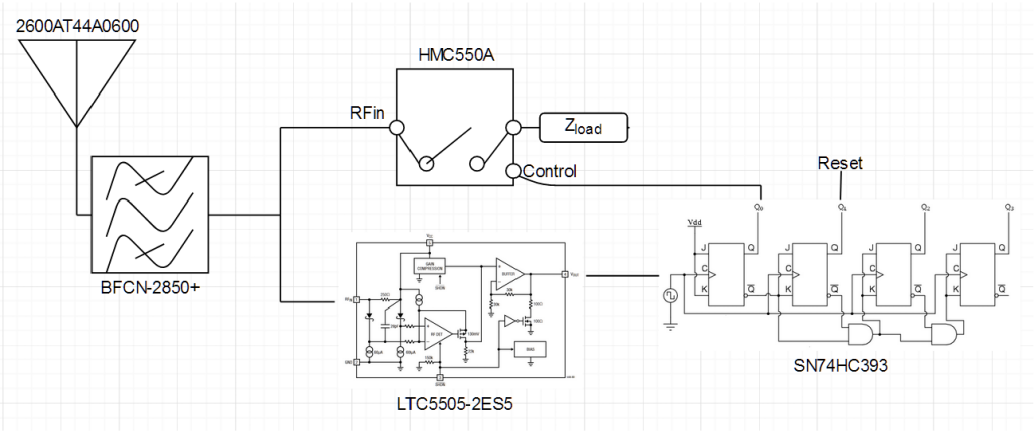

Figure 7.1: Hybrid RFID Circuit Schematic from [8]

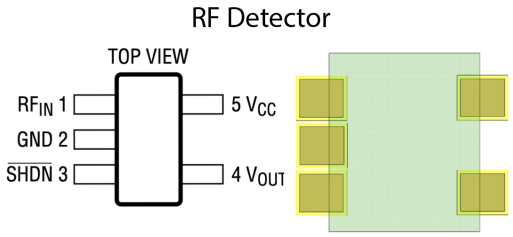

(a)

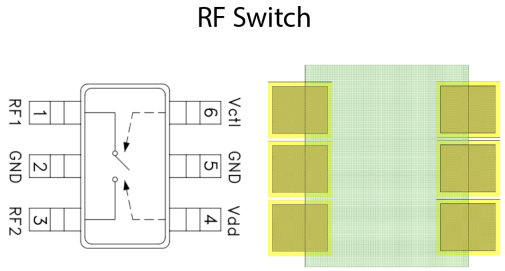

(b)

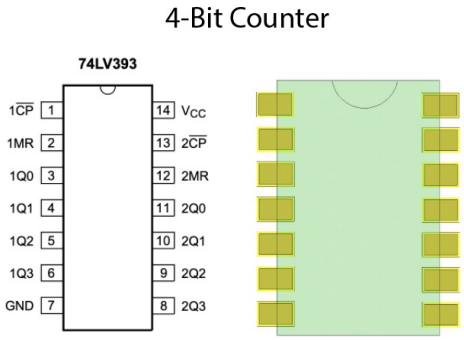

(c)

Figure 7.2: Custom made layout for the (a) RF Detector from (b) RF Switch (c) 4-Bit Counter

By using the custom-made footprints and utilizing the circuit schematic shown in 7.1, the Hybrid RFID circuit layout was made in AWR, which can be shown in Figure 7.3. This figure shows the layout of all of the components connected with 15 mil

copper traces. Since this circuit is a single layout board, a ground plane (underneath the circuit layout) could not have been incorporated. To try to accommodate for the lack of ground plane, the ground copper traces were made as thick as possible to help reduce inductance and provide a better return current path. Also, to prevent the copper traces from resonating, jumper wires will be connected across ground copper traces to reduce the electrical length of the copper trace. This will keep the lengths of the ground traces short enough to not resonant. These jumper wires are represented by red line segments in Figure 7.3. Apart from the key components listed previously, 0402 components were added to the circuit layout. These 0402 components are for bypass capacitors and two pi-networks (consisting of inductor and capacitors). One of the pi-networks of 0402 components is to create an impedance load that will be connected to the RF Switch. The other pi-network is a matching network that will connect between the RF Switch, the RF Detector, and the Curved Folded Dipole Antenna (CFDA). The overall form factor of the circuit layout shown in Figure 7.3 is approximately 24 mm by 29 mm (2.4 cm by 2.8 cm). To fabricate this circuit layout, the Laser etcher was used to etch the circuit layout on a 30 Rogers 4350 material. In Figure 7.4, the prototype of the fabricated Hybrid RFID circuit layout is shown.

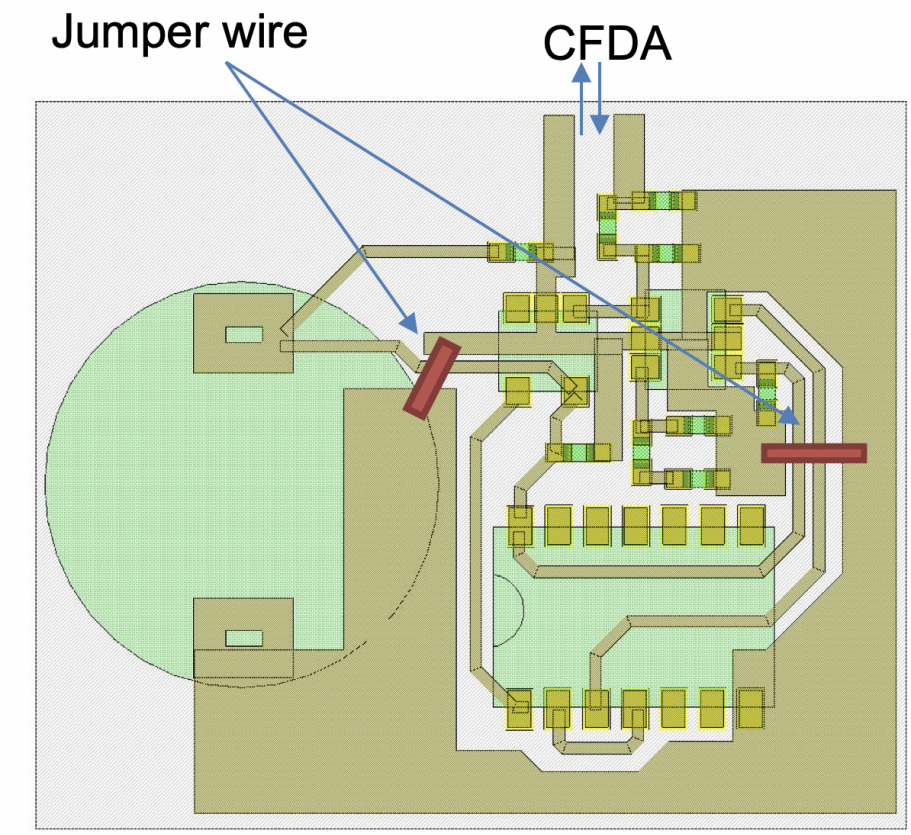

Figure 7.3: Hybrid RFID Circuit Layout in AWR

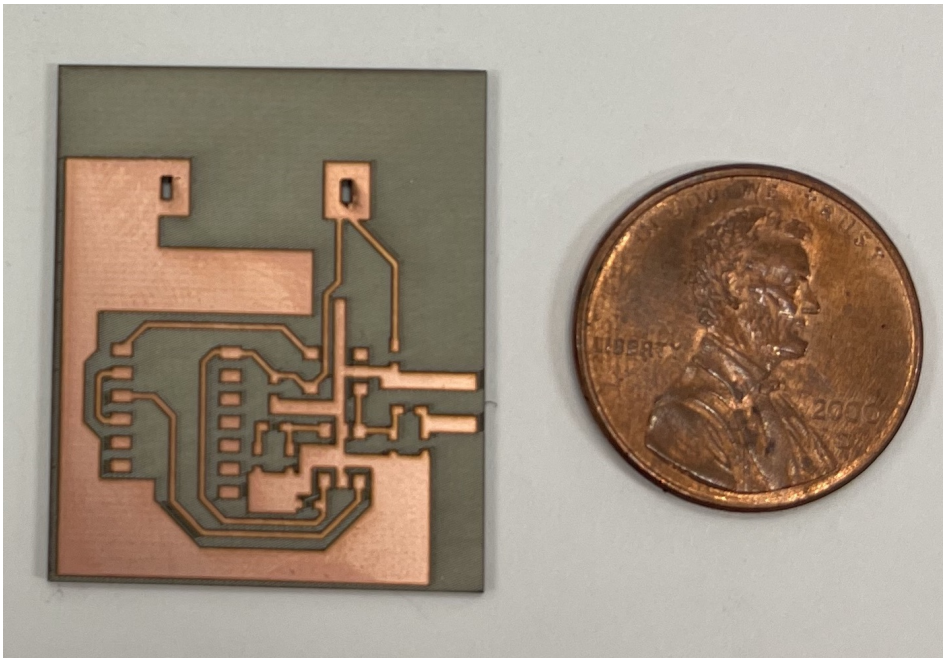

Figure 7.4: Hybrid RFID Circuit Layout Fabricated onto a 30 mil Rogers 4350

7.3 Conclusion

In conclusion, several proposed components of the original Hybrid RFID circuit were changed to help reduce weight. For example, the Battery (ECR2450) and battery holder (BU2450SM-JJ-GTR) were replaced with a BR-1225A watch battery, which significantly reduced the weight of the circuit by approximately 9 grams. In addition, the Hybrid RFID circuit layout was designed in AWR, shown in Figure 7.3, to have a small form factor of about 24 mm by 28 mm (2.4 cm by 2.8 cm) without the Curved Folded Dipole Antenna. This circuit layout was also fabricated, utilizing a Laser Etcher, and is shown in Figure 7.4. This work provided the first circuit layout prototype for the Hybrid RFID tag and will need to be attached to the Curved Folded Dipole Antenna (CFDA) for future measurements.

Chapter 8

Conclusions and Future Work

8.1 Conclusions

Bird tracking technology has been advancing rapidly for the past couple of decades. The Hybrid RIFD prototype designed in [8] shows that a working tag that can be used to backscatter energy from the WSR-88D weather radar. The work done in this thesis further develops the Hybrid RFID tag by designing a quasi-isotropic Curved Folded Dipole Antenna that has a small form factor (2 cm by 2.5 cm). Also, advancements in bird modeling were done by creating a bird model that represents a salvaged bird carcass electromagnetically. This bird model was modeled after the measurement results using a salvaged carcass of a Dark-eyed Junco (*Junco Hyemalis*). The results of the bird measurements were used as a baseline to find permittivity ϵ_r and conductivity σ values for the Bird Model. In the end, a $\epsilon_r = 1.2$ and $\sigma = 3[S/m]$ was used for the inner volume while a $\epsilon_r = 1.2$ and $\sigma = 0[S/m]$ was used for the outer volume of the Bird Model. With these values, it has been shown and verified that the Bird Model accurately represents a salvaged bird carcass (using a Dark-eyed Junco for the carcass) across the Insertion Loss, Impedance, and Far-Field Radiation patterns. Also, the Hybrid RFID tag was further developed by creating a realizable circuit layout that can be used for future measurements. This Hybrid RFID circuit layout is a single-layer

circuit board (using a 30 Mil Rogers 4350B) that allows for the RFID components to be soldered onto and provides a small form factor of 24 mm by 28 mm (2.4 cm by 2.8 cm).

8.2 Scientific Impact

This work has provided definitive measurements and results using salvaged bird carcasses. These measurements provide more knowledge on how the biological material of a bird impacts an antenna. A more accurate Bird Model was created to represent the impact of a salvaged bird carcass on an antenna. This Bird Model can be used for future Electromagnetic Simulations that involve the impact of birds on any particular device. Also, a quasi-isotropic Curved Folded Dipole Antenna with a small form factor (2 cm by 2.5 cm) was designed for the Hybrid RFID tag. Furthermore, the Hybrid RFID tag was further developed by creating and fabricating a circuit layout for a more realizable prototype for future measurements. These advancements provide more academic insight on the impact of birds on antennas and are one step closer to developing a new suitable bird tracking technology for mass deployment.

8.3 Future Work

For this work, there are a couple of paths for future research that can be continued. One path of future research would be to try to further verify the bird model by scaling it to a larger size. For instance, the Bird Model that was created in this work was modeled after the Dark-eyed Junco (*Junco Hyemalis*). For future research, this Bird Model can be scaled up a larger bird size and verify that the Bird Model continues to agree with larger birds. This would mean that a larger salvaged bird carcass would need to be obtained and used for verifying a larger Bird Model. Also, another path for future

research would be to do testing on the Hybrid RFID tag once it is soldered together and do backscatter measurements with the Curved Folded Dipole Antenna (CFDA) attached in the anechoic chamber. To take it one step further, the Hybrid RFID tag with the CFDA can be used to verify read range approximations. This will help verify that the Hybrid RFID tag can be seen by the WSR-88D weather radar at 100 km or more.

References

[1] W. Fiedler, "New technologies for monitoring bird migration and behaviour", *Ringing & Migration*, vol. 24, no. 3, pp. 175–179, 2009.

[2] J. Landt, "The history of rfid", *IEEE potentials*, vol. 24, no. 4, pp. 8–11, 2005.

[3] E. S. Bridge and D. N. Bonter, "A low-cost radio frequency identification device for ornithological research", *Journal of Field Ornithology*, vol. 82, no. 1, pp. 52–59, 2011.

[4] D. N. Bonter and E. S. Bridge, "Applications of radio frequency identification (rfid) in ornithological research: A review", *Journal of Field Ornithology*, vol. 82, no. 1, pp. 1–10, 2011.

[5] *Pit-tag.jpg*. [Online]. Available: https://idfg.idaho.gov/files/pit-tagjpg.

[6] S. A. Weis, "Rfid (radio frequency identification): Principles and applications", *System*, vol. 2, no. 3, pp. 1–23, 2007.

[7] E. S. Bridge, J. Wilhelm, M. M. Pandit, A. Moreno, C. M. Curry, T. D. Pearson, D. S. Proppe, C. Holwerda, J. M. Eadie, T. F. Stair, *et al.*, "An arduino-based rfid platform for animal research", *Frontiers in Ecology and Evolution*, vol. 7, p. 257, 2019.

[8] Z. Potts, "S", Master's thesis, University of Oklahoma, 2019.

[9] *Nexrad technical information*. [Online]. Available: https://www.roc.noaa.gov/WSR88D/Engineering/NEXRADTechInfo.aspx.

[10] Y. Wang, A. Pretorius, and A. Abbosh, "Low-profile antenna with elevated toroid-shaped radiation for on-road reader of rfid-enabled vehicle registration plate", *IEEE Transactions on Antennas and Propagation*, vol. 64, no. 4, pp. 1520–1525, 2016.

[11] P. P. Kumar and R. Maddirala, "Design of cpw-fed prong shaped patch antenna for rfid application at 5.8 ghz band", in *2014 International Conference on Electronics and Communication Systems (ICECS)*, IEEE, 2014, pp. 1–4.

[12] F.-L. Bong, E.-H. Lim, and F.-L. Lo, "Compact orientation insensitive dipolar patch for metal-mountable uhf rfid tag design", *IEEE Transactions on Antennas and Propagation*, vol. 66, no. 4, pp. 1788–1795, 2018.

[13] H. E. van Vliet and B. J. Stutchbury, "Radiotagged fledgling savannah sparrows passerculus sandwichensis at risk of entanglement in vegetation", *Ibis*, vol. 160, no. 4, pp. 919–922, 2018.

[14] L. Hou, M. Verdirame, and K. C. Welch Jr, "Automated tracking of wild hummingbird mass and energetics over multiple time scales using radio frequency identification (rfid) technology", *Journal of avian biology*, vol. 46, no. 1, pp. 1–8, 2015.

[15] D. V. Kholodnyak, P. A. Turalchuk, A. B. Mikhailov, S. Y. Dudnikov, and I. B. Vendik, "3d antenna for uhf rfid tags with eliminated read-orientation sensitivity", in *2006 European Microwave Conference*, IEEE, 2006, pp. 583–586.

[16] C. A. Balanis, "Antenna theory: A review", *Proceedings of the IEEE*, vol. 80, no. 1, pp. 7–23, 1992.

[17] H. Elkamchouchi and M. A. Nasr, "The s-shaped dipole antenna", in *ICMMT 4th International Conference on, Proceedings Microwave and Millimeter Wave Technology, 2004.*, IEEE, 2004, pp. 19–22.

[18] C. A. Balanis, *Antenna theory: analysis and design*. John wiley & sons, 2016.

[19] H. A. Wheeler, "The radiansphere around a small antenna", *Proceedings of the IRE*, vol. 47, no. 8, pp. 1325–1331, 1959.

[20] W. L. Stutzman and G. A. Thiele, *Antenna theory and design*. John Wiley & Sons, 2012.

[21] L. J. Chu, "Physical limitations of omni-directional antennas", *Journal of applied physics*, vol. 19, no. 12, pp. 1163–1175, 1948.

[22] M. I. Skolnik, *RADAR systems*. McGraw-Hill, NY, 2001.

[23] J. D. Griffin and G. D. Durgin, "Complete link budgets for backscatter-radio and rfid systems", *IEEE Antennas and Propagation Magazine*, vol. 51, no. 2, pp. 11–25, 2009.

[24] *Flexible circuits assembly*. [Online]. Available: https://www.allflexinc.com/.

[25] *Lifetag™ " cellular tracking technologies*, Dec. 2019. [Online]. Available: https://celltracktech.com/products/tag-system/lifetag/.

[26] T. Poydence, "Structure-independent conformal quasi-isotropic antennas for small unmanned aircraft system applications", 2017.

[27] S. Tanaka, Y. Kim, H. Morishita, S. Horiuchi, Y. Atsumi, and Y. Ido, "Wideband planar folded dipole antenna with self-balanced impedance property", *IEEE transactions on antennas and propagation*, vol. 56, no. 5, pp. 1223–1228, 2008.

[28] S. R. Best, "A discussion on the quality factor of impedance matched electrically small wire antennas", *IEEE Transactions on Antennas and Propagation*, vol. 53, no. 1, pp. 502–508, 2005.

[29] J. Martin, G. Swenson, and J. Bernhard, "Methodology for efficiency measurements of electrically small monopoles for animal tracking", *IEEE Antennas and Propagation Magazine*, vol. 51, no. 2, pp. 39–47, 2009.

[30] *Dissection of pigeon (with diagram) — zoology*. [Online]. Available: https://www.biologydiscussion.com/zoology/pigeon/dissection-of-pigeon-with-diagram-zoology/45131.

[31] *Dark-eyed junco identification*. [Online]. Available: https://www.allaboutbirds.org/guide/Dark-eyed_Junco/id.

[32] J. H. Rappole and A. R. Tipton, "New harness design for attachment of radio transmitters to small passerines (nuevo diseño de arnés para atar transmisores a passeriformes pequeños)", *Journal of field Ornithology*, pp. 335–337, 1991.